Soft Magnetic Materials

SOFT MAGNETIC MATERIALS

F. Fiorillo, G. Bertotti, C. Appino, M. Pasquale

Istituto Nazionale di Ricerca Metrologica
Strada delle Cacce 91, Torino 10135, Italy

A magnetic material is considered "soft" when its coercive fieldstrength is of the order of or lower than the earth's magnetic field (about 40 A/m). A soft magnetic material can be employed as an efficient flux multiplier in a large variety of devices, including transformers, generators, motors, to be used in the generation, distribution, and conversion of electrical energy, and a wide array of apparatus, from household appliances to scientific equipment. With a market around ◘ 20 billion in the year 2015 and annual growth rate around 5 %, soft magnetic materials (SMMs) are today an ever-important industrial product, offering challenging issues in properties understanding, preparation and characterization. An overview of the whole market of magnetic materials and the relative contributions of the different types of soft magnets is given in Fig. 1.

SMMs were at the core of the development of the early industrial applications of electricity. The steel practice at the turn of the 19th century was sufficiently developed to satisfy the increasing need of mild steel for the electrical machine cores. In 1900 Hadfield, Barrett, and Brown proved that, by adding around 2% in weight Si to the conventional magnetic steels, one could increase the permeability and decrease the energy losses [1]. Fe-Si alloys were more expensive and more difficult to produce and gained slow acceptance. In addition, the poor control of the C content was to mask the prospective performances of this product, compared with mild steels. It took more than two decades, characterized by a gradual improvement of the metallurgical processes, for Fe-Si to become the material of choice for transformers. An empirical attitude towards research in magnetic materials was prevalent at the time and applications came well before theoretical understanding. This is the case of the Goss process, developed in the early 1930s, by which the first grain-oriented Fe-Si laminations could be industrially produced [2]. In the years 1915-1923 G.W Elmen and co-workers at the Bell Telephone Laboratories systematically investigated alloys made of Fe and Ni, discovering the excellent soft magnetic properties of the permalloys (78% Ni) [3]. J.L. Snoek and co-workers are credited for the successful industrial development of ferrites in the 1940's [4], following attempts dating back to the first decade of the century. The discovery in 1967 of the soft magnetic amorphous alloys again occurred nearly by chance [5], but it provided a fertile field for technologists and theorists. It enriched the landscape of applicative magnetic materials, while straining existing theories on magnetic ordering. More recently, the need for increasingly high frequencies of operation in miniaturized devices and the appearance of novel phenomena of fundamental and applicative interest in low-dimensionality systems have propelled the investigation of the properties and the preparation techniques of soft magnetic thin films [6] [7]. Of special interest in this respect are the magnetoresistive phenomena observed in multilayer structures, where different layers can display, by combination of exchange interaction and applied field, either parallel or antiparallel magnetization. Spin-polarized conduction electrons diffusing through the layers suffer a magnetization orientation dependent scattering, according to their spin-up or spin-down character, resulting in a giant magnetoresistance effect [8].

GENERAL PROPERTIES OF SOFT MAGNETS

Magnetization curve and hysteresis

The behavior of a ferromagnetic material is summarized by the constitutive law $\boldsymbol{J}(\boldsymbol{H})$ (i.e., $\boldsymbol{M}(\boldsymbol{H})$), the dependence of the polarization $\boldsymbol{J}$ (magnetization $\boldsymbol{M}$) on the magnetic field $\boldsymbol{H}$. In many instances one can usefully recur to the $\boldsymbol{B}(\boldsymbol{H})$ law, where the magnetic induction $\boldsymbol{B}$, the quantity involved in the Faraday–Maxwell law, is related to $\boldsymbol{M}$, $\boldsymbol{J}$, and $\boldsymbol{H}$ by the relationship

$$\boldsymbol{B} = \mu_0\boldsymbol{H} + \mu_0\boldsymbol{M} = \mu_0\boldsymbol{H} + \boldsymbol{J}, \qquad (1)$$

where $\mu_0 = 4\pi\cdot10^{-7}$ NA^{-2} (H/m) is the magnetic constant (also called magnetic permeability of vacuum). The constitutive law (1) is the macroscopic outcome of an extremely complex sequence of microscopic processes, where, by combination of domain wall displacements, domain structure rearrangements, and rotations of the

magnetic moments, the system responds to a changing applied field $\boldsymbol{H}$ by moving through a succession of metastable minimum energy states [9], These processes are associated with irreversibility and losses, and a variety of $\boldsymbol{J}(\boldsymbol{H})$ behaviors endowed with hysteresis, a property shared with many physical phenomena. Because of hysteresis, any point in the (J, H) plane can be traversed by an infinite number of trajectories, depending on past history. But the experimental investigation requires some kind of accessible reference state. Two such states can be identified: the saturation, where all domains are swept out, and the demagnetized state (H =0, J = 0). The latter is reached either starting from saturation ($J = J_s$) and finely reducing the amplitude of an applied alternating field to zero value or by cooling the sample from the Curie temperature in the absence of any field. The curve taken after thermal demagnetization is called *virgin curve*. More frequently, the demagnetization process is performed using the decreasing alternating field and the *initial magnetization curve* is afterward obtained. An example of major hysteresis loop in a soft magnet (namely a grain-oriented Fe-Si sheet) is provided in Fig. 2. It is noted that, by virtue of the relatively low values of the applied field, no difference can be appreciated, according to Eq. (1), between the $B(H)$ and $J(H)$ curves. It is also remarked in this figure that a field H_c, the *coercive field*, must be applied in reverse, after having attained the peak polarization value J_p, in order to bring the material to the demagnetized state. H_c provides a measure of the magnetic hardness (softness) of the material, its value typically differing by many orders of magnitude in soft magnetic materials and in permanent magnets. Negligible differences between H_{cJ} and H_{cB}, the fields required to bring to zero the polarization and the induction, respectively, exist in soft magnets. By connecting the tip points of the nested symmetric minor loops, we obtain the *normal magnetization curve*. It coincides in practice with the initial magnetization curve. At low fields it is in many cases described by the Rayleigh law $J(H) = aH + bH^2$, where a and b are structure dependent constants. The Rayleigh region occupies in most soft magnets a J span going up to some ten percent of J_s (for example, 0.1 T – 0.2 T in low-carbon steels or 0.04 T in Mn-Zn ferrites).

In the course of magnetization and demagnetization, energy is exchanged between the sample and the external world. In particular, the energy per unit volume to be provided for bringing the material to a given induction value B_p starting from the demagnetized state is $U(B_p) = \int_0^{B_p} H\,dB$. Part of it is stored and part is dissipated in the material. Over a complete cycle the previous integral, the area of the hysteresis loop, provides the energy loss per unit volume

$$W = \oint H dB = \oint \mu_0 H\, dH + \oint H dJ = \oint H dJ\,. \qquad (2)$$

It is noted that the reactive term $\oint \mu_0 H\, dH$ averages out to zero. The dissipated energy increases with the frequency of the magnetizing field, because of dynamic viscous-type phenomena interfering with the magnetization process (e.g., eddy currents in metallic materials). We talk in this case of rate-dependent hysteresis, an example of which is provided in Fig. 3, showing the evolution of the hysteresis loops versus frequency in Fe-Co sheets.

The hysteresis loop embodies the magnetic properties involved in any kind of application and by the value of its parameters a classification of the materials can be made. The coercive field H_c, the remanent polarization J_r, the peak permeability $\mu_p = B_p / H_p$, the initial permeability, and the energy loss W are the base parameters by which the properties of the materials can be assessed. The material composition actually determines the values of the so-called intrinsic magnetic parameters, like the Curie temperature, the saturation magnetization, the magnetic anisotropy constants and the magnetostriction constants, which, in turn, affect the magnetization process in a way related to the material structure (e.g. crystallographic texture, grain size, foreign phases, lattice defects, etc.). By proper choice of composition and suitable metallurgical and thermal treatments, extra soft magnets can be obtained, where the coercive field can attain values lower than 1 A/m, with the relative permeability in the range of a few 10^5. But it should be stressed that a number of additional properties, like thermal and structural stability, stress sensitivity of the magnetic parameters, mechanical properties and machinability, thermal conductivity, and flexible response to thermomagnetic treatments are to be considered. The final acceptance of a specific material in applications will result from a cost-benefit evaluation of all these properties.

There are cases where the DC constitutive law $J(H)$ can be approximated by a linear function. This occurs, for example, in some soft magnetic alloys subjected to transverse field annealing [10] or, quite generally, at very low inductions, inside the Rayleigh region. High-frequency applications of soft magnets are typically limited to such low inductions and we can describe the material response to a sinusoidal applied field $H(t) = H_p \cos \omega t$ with the phase-delayed induction $B(t) = B_p \cos(\omega t - \delta) = B_p \cos\delta \cos\omega t + B_p \sin\delta \sin\omega t$. The function $B(t)$ can thus be expressed as the sum of two 90° phase-shifted sinusoids of peak amplitude

$B_1 = B_p \cos\delta$ and $B_2 = B_p \sin\delta$. We can equivalently write, using the complex notation, $H(t) = H_p e^{j\omega t}$ and $B(t) = B_p e^{j(\omega t - \delta)}$. The 90°-delayed component of the induction is connected with the dissipation of energy. From the definition of the energy loss per cycle *W* in Eq. (2), we obtain the energy loss per unit volume

$$W = \int_0^T H(t) \cdot \frac{dB(t)}{dt} dt = \pi H_p B_p \sin\delta \qquad (3).$$

On the other hand, if we apply the definition of permeability to both in-phase and 90° out-of-phase components of $B(t)$, we obtain the quantities

$$\mu' = \frac{B_p}{H_p}\cos\delta \qquad \mu'' = \frac{B_p}{H_p}\sin\delta \,. \qquad (4)$$

μ' and μ'' can be viewed as the components of the complex quantity

$$\mu = \frac{B_p e^{j(\omega t - \delta)}}{H_p e^{i\omega t}} = \mu' - j\mu'' \qquad (5)$$

and accordingly take the name of real and imaginary permeability, respectively. It is immediate to obtain from Eq. (3) that the energy loss per unit volume at a given peak polarization J_p and the complex permeability are related by the equation

$$W = \pi J_p^2 \cdot \frac{\mu''}{\mu'^2 + \mu''^2} \qquad (6).$$

Going towards low frequencies, the hysteresis loss might have a role, even at very low inductions. This is accounted for, with good approximation, by a residual μ'' value, which persists down to $f \to 0$. An example of correlated behavior of μ' and μ'' as a function of frequency is provided for the specific case of a Mn-Zn ferrite ring sample excited at J_p = 2 mT in Fig. 4. Here we notice how μ'' takes a negligible value at the lowest frequencies. The ratio between the imaginary and real permeabilities provides a measure of the departure of the behavior of an inductor with ferromagnetic core from that of a pure inductive reactance. Such a ratio is, according to Eq. (4), $\mu''/\mu' = \tan\delta$. The quantity tanδ, called "loss factor", coincides with the inverse of the quality factor *Q* of the inductor.

An overview of the physical and magnetic properties of the main soft magnetic materials used in applications is provided in the Tables 1 and 2. Fig. 5 shows that the Curie temperature, which provides a measure of the strength of the ferromagnetic exchange interaction, progressively increases on passing from soft ferrites, where the interaction mechanism is actually of antiferromagnetic nature, to amorphous alloys and crystalline alloys. An overall view of the coercive field and maximum permeability ranges typically attained in soft magnets is given in Fig. 6 and Fig. 7, while the behavior of the initial magnetization curves is comprehensively displayed in Fig. 8. Examples of major DC hysteresis loops are finally shown in Fig. 9.

Anisotropy energy and magnetization process

The key feature of SMMs, as of any other magnetic material, is that they are subdivided into magnetically saturated regions, the magnetic domains. In each domain the magnetization is uniform and points along a direction changing from domain to domain. The overall magnetization of a macroscopic piece of SMM is thus the result of an average over many domains, each of them being characterized by a privileged orientation, resulting from some form of anisotropy. Strength and symmetry properties of the anisotropy play indeed a leading role in determining the magnetic behavior of the material. The strength is measured by the anisotropy constant, *K*, which has the dimensions of an energy density (J/m^3). The symmetry can be uniaxial, cubic, or more complex, depending on the material.

The magnetization process in an SMM is the result of two microscopic mechanisms: motion of the domain walls and uniform rotation of the magnetization inside the magnetic domains. In conventional Fe-based crystalline alloys the rotations require high field strengths, because the interaction between field and polarization $E_H = -\boldsymbol{H} \cdot \boldsymbol{J}_s$, the Zeeman energy, must balance the magnetocrystalline anisotropy energy E_K roughly of the order of the anisotropy constant K_1. Since K_1 is around some 10^4 J/m^3, fields in the 10^3 – 10^4 A/m range must be

applied to achieve substantial rotations in iron and silicon steels. A soft magnetic behavior can be achieved, in these materials, only through easy displacements of the domain walls. Frictional forces, inevitable in real defective materials, resist these displacements. The coercive field measures the typical field strengths at which the domain walls are unpinned from defects and a substantial part of the magnetization is reversed. Energy is lost in this process, and magnetic hysteresis is accordingly observed. The subject of coercivity and hysteresis is classically treated by theorizing the motion of a domain wall, assumed either as a rigid [11] [12] or a flexible [13] object, in a perturbed medium. Since the energy of the domain wall γ_w is directly related to the anisotropy constant K_1 according to the expression $\gamma_w \propto \sqrt{AK_1}$, where A is the exchange stiffness constant, denoting the strength of the ferromagnetic exchange, any structural perturbation, influencing the exchange and anisotropy energies, reflects in a spatially perturbed domain wall energy. A domain wall moving in a defective medium takes then a random energy profile, whose spatial derivative must be overcome by the pressure of the applied field in order to achieve wall motion. The coercive field H_c, which is the field upon which the wall gets loose from the hindering effect of the structural defects, is then chiefly controlled by the value of the anisotropy constant K_1, the larger K_1 the larger H_c. In spite of the relatively high values attained by K_1, very soft magnetic behavior can however be achieved in Fe and Fe-Si when the microstructure is suitably controlled. In practice, this means having the least content of precipitates, voids, dislocations and point defects, together with large and favourably oriented grains. With the applied field directed as far as possible alongside one of the <100> easy axes, that is in the plane of the main 180° domain walls, an obvious directional advantage exists for the wall displacements, as remarkably demonstrated by the behavior of the grain-oriented (GO) Fe-Si laminations. The role of the microstructural defects is clearly observed in Fe. Here one can reach coercive fields as low as a few A/m upon prolonged purification and annealing treatments, leading to very low dislocation densities and C and N concentrations (some 10 – 20 parts in 10^6 ppm) [14] [15]. Coercivities of a few hundred A/m can be found instead when these concentrations are in the 100 ppm range and beyond [12]. C and N are basically insoluble in α-Fe and tend to form carbides and nitrides, which act as strong pinning centers for the domain walls. With much higher C content (around 1 wt%) graphite precipitates and martensitic domains are additionally formed, and H_c can reach values typical of hard magnets (a few 10^4 A/m).

Very low values of the magnetic anisotropy (say with K in the range of few ten J/m^3 and less) directly lead to soft and extra-soft magnetic properties, because both rotations and domain wall displacements become easy processes. This is the case, for example, of the Fe-Ni alloys with composition around Fe_{20}-Ni_{80}. K_1 is positive in α-Fe (b.c.c. cell) and negative in Ni (f.c.c. cell) and it passes through zero on the high Ni side in the Fe-Ni alloys. Vanishing anisotropy can equally be obtained in amorphous and nanocrystalline alloys, because the structural order in these materials is extended over limited distances, from a few atomic spacings to a few nanometers. The characteristic length L_{ex} controlling the magnetization process, the exchange length (of the order of the domain wall thickness), encompasses a large number of local ordered structural units, be them agglomerate of few atoms or nanometer sized crystals. The magnetic moments in such units are constrained to alignment by the exchange interaction and cannot follow the random directions of the local easy axes. The local magnetocrystalline anisotropy K_1 is then averaged out to a residual anisotropy K_0 across the N structural units of average size δ enclosed in the volume $L_{ex}^3 = N\delta$ according to $K_0 \approx K_1/\sqrt{N}$ [16]. Domain wall thickness and K_0 are related by the standard equation $L_{ex} \sim \pi(A/K_0)^{1/2}$, where A is the stiffness constant, and we get [17]

$$K_0 \approx K_1\left(\frac{\delta}{L_{ex}}\right)^{3/2} = K_1\left(\frac{\delta}{L_1}\right)^6, \qquad (7)$$

where $L_1 \sim \pi(A/K_1)^{1/2}$ is the exchange length of the crystalline counterpart. By taking $\delta = 10^{-9}$ m, $K_1 = 4.8\cdot10^4$ J/m^3 (as in Fe) and $A \sim 10^{-11}$ J/m, we find the negligible value $K_0 = 5.8\cdot10^{-6}$ J/m^3.

Once the magnetocrystalline effects are made negligible, other sources of magnetic anisotropy are brought to light. This is the case, for example, of the local anisotropies arising in the highly magnetostrictive Fe-based amorphous alloys, due to the magnetoelastic coupling between frozen-in stresses and the magnetization. In the typical alloy of composition $Fe_{78}B_{13}Si_9$ the saturation magnetostriction is $\lambda_s \sim 35 - 40\cdot10^{-6}$ and the long range internal stresses generated by the rapid solidification process are of the order of 50-100 MPa [18][19]. Induced anisotropies $K_\sigma = (3/2)\lambda_s\sigma$ of several hundred J/m^3 can therefore arise [20] and annealing treatments are required to recover excellent soft magnetic behavior. Co-based amorphous alloys (like $Co_{71}Fe_4B_{15}Si_{10}$ and $Co_{66}Fe_5Cr_4B_{15}Si_{10}$), Fe-Ni alloys of the permalloy type, and nanocrystalline alloys (like $Fe_{73.5}Cu_1Nb_3Si_{13.5}B_9$) have vanishing magnetostriction ($\lambda_s \sim 10^{-8} - 10^{-7}$) and, lacking also the anisotropy of magnetocrystalline origin, attain the lowest coercivities and record values of permeability. Their properties can be tailored by inducing calibrated uniaxial anisotropies through annealing treatments under saturating fields. In a saturated Fe-Ni alloy, the magnetization interacts with the Fe-Fe and Ni-Ni atomic pairs in such a way that, if the temperature is sufficiently high, these pairs tend to diffuse and distribute preferentially along the direction of the magnetization imposed by the applied field. A directional order sets in, although the alloy preserves its character of random

solid solution. In the amorphous alloys, anisotropic atomic rearrangements of the local ordered units occurs, with symmetry influenced by the direction of the magnetization [21], while in the nanocrystalline alloys directional pair ordering of the Si atoms in the Fe-Si nanocrystals is invoked to justify the induced anisotropy [16]. In magnetostrictive alloys, stress-induced anisotropy and anisotropy induced by field annealing can be suitably combined to impose a desired hysteresis loop shape.

Magnetic losses

SMMs are chiefly employed in magnetic cores of AC machines and devices, from 50 Hz to several MHz. The technically relevant quantity in applications is the energy loss. Eddy currents are generated by a time varying magnetic flux, leading to both shielding of the core by the associated counterfields (skin effect) and generation of heat by Joule effect. Excluding ferrites, which are either insulating or near-insulating materials, and the soft magnetic composites, near net-shape cores obtained by compacting and bonding ferromagnetic powders, soft magnets are generally used in sheet form, in order to minimize skin effect and losses. The theoretical assessment of these effects is far from simple, because it is seldom possible to treat the material as a continuum, characterized by a given magnetic permeability, and apply to it the Maxwell's equations. The magnetic structure is made of domains and domain walls and the distribution of eddy currents can be extraordinarily complex and non-uniform. Williams, Shockley and Kittel were the first to take at face value such a complexity, by investigating the dynamic behavior of a 180° Bloch wall in single crystals of Fe-Si. They theorized it through a balance equation involving, on the one hand, the applied magnetic field and, on the other hand, the structural pinning field and the eddy current counterfield (WSK model) [22]. Pry and Bean generalized the WSK model to a system of 180° walls, emulating the real domain structure of a GO Fe-Si sheet [23]. The whole problem was eventually assessed by G. Bertotti, who showed that the complexity of the dynamic magnetization process in real structures can be properly described by means of statistical methods [24] [25]. Bertotti's theory provides solid physical background to the concept of loss separation, where the total energy loss $W(f)$ at any given magnetizing frequency f and peak polarization J_p can be considered as the sum of three components, each of them depending in a different way on frequency

$$W(f) = W_h + W_{cl}(f) + W_{exc}(f) \ , \qquad (8)$$

as illustrated in Fig. 10. The meaning of these components is the following. W_h, called *hysteresis loss*, is the residual energy dissipated in the limit $f \to 0$ and, as such, it is independent of f. W_{cl}, called *classical loss*, is the loss calculated applying Maxwell's equations to the material when it is fictitiously assumed as fully homogeneous from the magnetic viewpoint (absence of domains). The *classical loss* W_{cl} is a sort of background term, always present and independent of any structural feature. For a lamination of thickness d and conductivity σ, one finds, under sinusoidal time dependence of the magnetic polarization and complete flux penetration in the lamination cross-section (negligible skin-effect), the classical loss per unit volume

$$W_{cl} = \frac{\pi^2}{6} \cdot \sigma d^2 B_p^2 f = \frac{\pi^2}{6} \cdot \sigma d^2 J_p^2 f \qquad [\mathrm{J/m^3}] \qquad (9)$$

where, as is usual the case with soft magnets tested at technical inductions, we neglect any difference between the peak values of induction B_p and polarization J_p. As shown in Fig. 10b, by summing up W_h and W_{cl} one falls short of the measured energy loss value. The remainder W_{exc} is called *excess loss*. Fig. 10b shows, in particular, that the prediction by Eq. (9) grossly underestimates the measured loss in GO laminations at 50-60 Hz, the frequencies at which the largest amount of electrical energy is generated and used, besides failing to account for the experimental non-linear dependence of W on f.

The three loss components are associated with different eddy current mechanisms and different space-time scales of the magnetization process. Flux reversal is actually concentrated at each instant of time inside the moving domain walls and, even under quasi-static excitation, eddy currents arise, because the domain wall displacements, hindered by the pinning centers, occur in a jerky fashion (Barkhausen effect). Intense local current transients, with lifetime around 10^{-9} s, are generated around the jumping wall segments and energy is correspondingly dissipated. The hysteresis component W_h integrates the so generated loss over a period and the unit volume of the material. Since the time constant of the microscopic eddy current pulses is always many orders of magnitude smaller than the typical magnetization period $T = 1/f$, it is apparent that the associated local magnetization reversal is not affected by the rate of increase of the applied field and W_h is independent of frequency. For a given value J_p, W_h gives a measure of the coercive field. This is consistent with the fact that the Barkhausen mechanism is independent, as the coercivity should be, of the material conductivity. The excess loss

W_{exc} is associated with the large-scale motion of the domain walls. The theory shows, again in the absence of skin effect, that the excess loss behavior in most SMMs can be described to a good approximation by the expression

$$W_{\text{exc}} = k_{\text{exc}} \cdot \sqrt{\sigma f} \cdot J_{\text{p}}^{3/2} \qquad [\text{J/m}^3] \qquad (10),$$

where k_{exc} is a parameter related to the properties of the domain structure and their relationship with the structural properties of the material [24][25]. As such, it generally increases to some extent with J_p [26]. Eq. (10) is actually a reduced form of a more general expression for W_{exc}. The two expressions normally coincide beyond a few Hz [24] [26]. Very broadly, it can be stated that k_{exc} is the larger the more discrete is the magnetization process. Very large domains are therefore not desirable from this viewpoint and, as discussed in the following, methods aiming at increasing the density of the domain walls in the sheet samples have sometimes been devised.

While Bertotti's theory is solidly assessed from the physical and experimental viewpoint and has found widespread application, alternative approaches have been proposed in recent times, pointing to the simultaneous prediction of magnetic losses and shape of the hysteresis loops versus frequency in soft magnetic sheets. In particular, S. Zirka, et al. have developed a viscosity-based magnetodynamic model, where the classical Maxwell's diffusion equation is combined with a magnetic hysteresis model, which can be either rate-independent or rate-dependent [27] [28]. This approach requires the implementation of numerical methods. In the very special case of sharply rectangular hysteresis loops, emulating ideal step-like magnetization curves [9], it has been assumed that a breakdown of the classically held uniformity of the distribution of the magnetic flux density, implied in the derivation of Eq. (9), occurs even at low frequencies [29]. It has been suggested that this effect might occur, via propagation of saturation magnetization wavefronts across the sheet thickness, also in ordinary non-oriented steel sheets excited at high inductions [28]. However, direct experimental evidence for the occurrence of this reversal mechanism is not available at present time.

In conclusion, if minimization of the AC energy losses is desired, not only the lamination thickness and the material conductivity need to be reduced, as suggested by the classical approach (Eq. (9)), but also the microstructure must be controlled, in order to minimize both W_h (i.e. the coercive field) and W_{exc}. This emphasizes the role of the metallurgical process, whose continuous refinement over the years has produced increasingly better control of the various structural parameters (e.g. impurities, defects, grain size, crystallographic texture) and clear progress of the magnetic properties of the materials.

IRON AND LOW-CARBON STEELS

Iron is referred to as "high purity" when the total concentration of impurities (typically C, Cu, N, O, P, S, Si, Al) does not exceed a few hundred ppm. It is otherwise called *low-carbon steel* (LCS) or *non-alloyed steel*. When soluble elements like Si and Al are deliberately introduced, typically in the range of a few per cent, it is appropriate to speak of "silicon steels". Very pure iron is seldom used in applications, but the study of its properties is of basic physical interest. The main practical drawbacks of pure Fe are its relatively high electrical conductivity, which makes it unsuitable for AC applications, its poor mechanical properties, and its cost. Low-cost LCSs (C < 0.1 wt%) are largely applied in a multitude of small electrical machines (for instance fractional horse power motors) and devices where efficiency is not of primary concern. Together with the silicon steels, they cover about 70% of the world tonnage of soft magnetic materials. More efficient LCSs are today increasingly developed, under the pressure of rising energy costs and environmental concerns. Higher grades are therefore now available, where improved magnetic properties are obtained chiefly by introducing a small amount of Si (< 1 wt%) and decreasing the content of impurities (especially sulfides, carbides and nitrides).

High-purity iron can be obtained starting with commercially pure iron (e.g. of the ARMCO type) and refining it by suitable methods. These include prolonged annealing in pure H_2 at temperatures not far from the melting point (e.g. 48 hours at 1480 °C), zone melting and levitation melting. By means of these methods, some 20 to 30 ppm maximum total impurity content can be reached, with C and N less than 10 ppm. Relative permeabilities $\mu_r \sim 10^5$ and coercivities H_c = 1-2 A/m have been measured in highly purified iron samples [30]. Some common iron grades are listed in Table 3. ARMCO-type iron is ideal for soft cores working in a DC environment, like the electromagnets. Its high electrical conductivity is a drawback for AC applications, but the combination of high permeability and high conductivity can lead to efficient magnetic field shielding at power frequencies [31]. In addition, pure iron is relatively resistant to corrosion, due to the formation of a protecting cohesive layer of rust.

Low-carbon steels used in magnetic cores are generally produced as sheets through a sequence of hot and cold rolling passes and thermal treatments, as schematically shown in Table 4. The specifications for these steels are provided in the IEC Standard 60404-8-3 [32]. To improve the magnetic performance, the sheets must be decarburized. It is a final annealing treatment in wet hydrogen atmosphere, at temperatures around 800° C. By this process, the carbon concentration can be reduced to less than 50 ppm. The main detrimental effect of

the residual C is magnetic aging, that is, the increase of coercivity with time ensuing from the precipitation of cementite particles and the related domain wall pinning phenomena. Aging may represent a real threat in actual magnetic cores, where operating temperatures of 50 °C - 100 °C are common. Fig. 11 shows that in LCSs with C concentrations as low as 45 ppm (in weight) a potential for aging still exists [33]. Nitrogen can equally induce aging, but it can be partly stabilized by the formation of AlN precipitates. These, however, may adversely affect the grain texture during re-crystallization annealing, by favoring the growth of magnetically hard {111} planes, an effect that is contrasted by controlled addition of B (~30 ppm) and Zr (0.07 wt %) [34]. Reduction of the C, N, and S concentrations in the range of 20 – 30 ppm can also be obtained, in high quality steels, by vacuum degassing of the melt, which can make the final decarburization anneal unnecessary, with beneficial effects on the production costs [35].

The $\alpha \longrightarrow \gamma$ transition takes place in Fe at 911 °C and the final thermal treatments are thus preferably made at lower temperatures, which may limit the range of attainable grain sizes and crystallographic textures. LCSs are generally delivered as semi-processed products, because they need to be in a cold worked state before punching and cutting. The necessary mechanical hardness is imparted by means of temper rolling, a 3 to 5 % cold reduction. Once punched, the laminations are subjected to decarburization and grain growth annealing, eventually followed by controlled surface oxidation ("bluing"), to ensure acceptable interlaminar insulation in the core. One notable consequence of temper rolling is a somewhat exaggerated grain growth upon final annealing, which overcomes to some extent the limitations imposed on the upper treatment temperatures by the $\alpha \longrightarrow \gamma$ transition.

The performance of the LCS sheets is best described in terms of AC magnetic properties at 50 - 60 Hz. In the absence of purification treatments and significant Si content, AC losses at 60 Hz and 1.5 T can reach some 15 W/kg in 0.65 mm thick laminations, with relative permeability $\mu_r = 500 – 1000$. The addition of 0.5 - 1 wt% Si, together with better composition control, may contribute to lowering this loss figure to less than 6 - 8 W/kg in 0.50 mm thick sheets. However, the introduction of Si decreases the saturation magnetization, which may be somewhat detrimental to permeability. Therefore, the loss performance is improved, whenever possible, by use of very clean materials, as obtained by extensive application of vacuum degassing. Coated semi-processed LCSs are thus available, which combine improved loss and permeability behavior ($P \sim 4$ W/kg and $\mu_r \sim 3000$ at 1.5 T and 50 Hz in 0.50 mm thick laminations) with excellent punching performance. On increasing the magnetizing frequency, the benefit of decreasing the lamination thickness and increasing the Si content becomes apparent, as shown in Fig. 12.

Pure Fe and non-alloyed steels are employed as cores of DC electromagnets, where one exploits their high saturation magnetization to produce strong fields. Typical AC applications are relays, lamp ballasts, fractional horse power motors and small transformers, where performance is needed at low price. It is known that in small motors (power less than 1-2 kW), where the limited size imposes high induction values in the stator teeth, copper losses tend to predominate over iron losses. The solution offered by non-alloyed steels, with their high values of permeability at high inductions, high thermal conductivity, and affordable price, represents a good compromise between the requirements of costs and machine efficiency. Optimal product performance is in any case obtained through proper design considerations.

The base physical and magnetic parameters of low-carbon steels and low-Si laminations are given in Tables 1 and 2. We list here additional properties and features of these materials:

1) *Temperature dependence of the magnetic properties.*

There is a moderate decrease of the coercive field, of the order of 10 %, following the increase of temperature from 20 ° C to 200 °C, due to a concurring decrease of the anisotropy energy. The total power loss at 50 Hz decreases more rapidly, by about 20 %, in the same temperature interval because of the concomitant increase of the electrical resistivity. The permeability is correspondingly increased, but to somewhat lesser extent.

2) *Stress dependence of the magnetic properties.*

Elastic tensile stresses introduce slight magnetic softening. Compressive stresses engender instead substantial decrease of the magnetic permeability. This effect is consistent with sign and value of the magnetostriction constants in iron single crystals. Plastic deformation is conducive to increased coercivity and losses and decreased permeability. The increase of coercivity roughly follows a square root dependence on the plastic strain [36]. An example of the effect of plastic deformation by tensile straining on the DC hysteresis loop of polycrystalline pure iron (grain size $\langle s \rangle = 14$ μm) is given in Fig. 12.

3) *Mechanical properties*. Pure Fe and low carbon steels are mechanically soft and can be easily machined. However, lamination punching and cutting need to be made on the cold worked materials, before the final annealing treatment.

4) *Coating.* Pure iron and LCS sheets are not coated in general. They come instead with a slight homogeneous surface oxidation, which is sufficient to provide acceptable layer-to-layer electrical insulation in the assembled cores.

5) *Delivery.* Pure iron is delivered either in bulk form as billets of various diameters or thick slabs (thickness d around 200 mm), hot-rolled plates (3 mm $\leq d \leq$ 120 mm), cold-rolled sheets (0.50 mm $\leq d \leq$ 2 mm). They are provided to the customer as semi-finished products and need final heat treatment after cutting/punching, in order to attain the desired soft magnetic properties.

6) *Specifications.* The grades, general requirements, magnetic properties, geometric characteristics, tolerances, and technological characteristics are defined in the Standards IEC 60404-8-3 [32] and IEC 60404-8-6 [37].

7) *Applications*. Low-carbon steels are chiefly employed in DC electromagnets, electromagnetic shields at power frequencies, relays, lamp ballasts, fractional horse power motors, and small transformers.

IRON-SILICON ALLOYS

The addition of few atomic percent Si brings about notable changes in the physical, mechanical and magnetic properties of Fe, as summarized in Fig. 14. The most notable effect regards the electrical resistivity, which increases at a rate around $5 \cdot 10^{-8}$ Ω·m per soluted atomic percent. This implies a more than fourfold increase on passing from pure Fe to the conventional Fe-(3 wt%)Si alloys, a remarkable benefit in terms of decreased AC losses. But there are further properties taking advantage of Si alloying. The magnetocrystalline anisotropy constant K_1 decreases with increasing Si (from 46 kJ/m^3 in pure Fe to 36 kJ/m^3 in Fe-(3 wt%)Si), reflecting into lower coercivity. The yield strength increases, which favors material handling and machining. Inspection of the Fe-Si phase diagram (Fig. 15) shows that above about 2 wt% Si the $\alpha \rightarrow \gamma$ transition (bcc to fcc structure) no longer takes place and the previously remarked restrictions on the final annealing temperatures in the low-carbon steels do not longer exist. The chief factors against substantial addition of Si are the reduction of the saturation magnetization (around 2.5 % for any weight percentage increase of Si concentration) and the fact that there is no practical way of achieving laminations with more than about 4 wt% Si by conventional rolling processes. The heterogeneous formation of FeSi and Fe_3Si ordered phases leads in fact to severe material embrittlement [38]. Alloying with Al in place of Si leads to quite similar physical and structural effects, while not causing material embrittlement. But Al is very reactive and can easily lead to oxide formation, it brings about an increase of the magnetostriction, and is costlier. An overview of the behavior of the physical and intrinsic magnetic properties of the Fe-Si and Fa-Al alloys is provided in Ref. [39].

Non-oriented Fe-Si alloys

Non-oriented (NO) Fe-Si alloys are Soft Magnetic Materials (SMMs) with an approximately isotropic grain texture. They cover the medium and high quality range of SMMs for applications in electrical rotating machines (motors and generators), where good isotropic magnetic properties are required. They come in a variety of grades, the higher ones being associated with higher Si content. The specifications for NO Si steels are provided in the Standards IEC 60404-8-4 [40], IEC 60404-8-6 [37], IEC 60404-8-8 [41]. The materials are typically graded by their power loss at 50 Hz and peak polarization J_p = 1.5 T. For example, a magnetic steel sheet with designation M250-35A has nominal thickness 0.35 mm and maximum power loss at 50 Hz and 1.5 T of 2.50 W/kg (and, typically, 1.0 W/kg at 1.0 T and magnetic polarization J_p = 1.60 T for applied field H = 5000 A/m).

The Si concentration can vary between 1 wt% and 3.7 wt% and some percentage of Al (0.2 – 0.8 wt%) and Mn (0.1 – 0.3 wt%) is usually justified by metallurgical requirements. These impurities increase the alloy resistivity without impairing the mechanical properties. Al lowers the temperature of the primary re-crystallization and prevents aging by N precipitation, by stabilizing it through the formation of AlN second phases. Mn can capture residual S impurities, leading to the formation of MnS precipitates. In order to counter the adverse effects on the soft magnetic properties of the material brought about by these precipitates, clean material preparation methods are required [35]. The lower grade NO laminations (less than 2 wt% Si) are produced and delivered in the semi-processed state and follow the same thermomechanical history of low-carbon steels (sketched in Table 4), with final thickness ranging between 0.65 mm and 0.50 mm. The higher grades are instead fully processed materials. They are obtained according to the procedure outlined in Table 5. The hot-rolled sheets (thickness 2.3 mm – 1.8 mm) are cold rolled to intermediate gauge, annealed at 750 °C – 900 °C, reduced to the final gauge of 0.65 mm – 0.35 mm, subjected to a re-crystallization and decarburization anneal at 830 °C – 900 °C and final grain-growth anneal at 850 °C – 1100 °C. A single-stage cold reduction is a basic variant of this process. A phosphate-based or chromate-based coating (thickness 0.5 μm – 5 μm) is then

applied, which not only provides the necessary interlaminar insulation, but also ensures good sheet punchability. The latter property is important, because of the strict tolerances required in rotating machine cores and the need to avoid edge burrs, a possible cause of interlaminar short circuits in the assembled cores. Emphasis has been given in recent times to environmental friendly chrome-free coatings. Polymer-based lacquers for both semi-processed and fully processed steels have therefore been developed, which can be cured by ultraviolet radiation in a fast, energy efficient, and hazard-free process [42]. Contrary to the case of semi-finished products, no stress relief treatment is applied in general to the fully treated sheets after punching.

By acting on the composition and the preparation methods and relying upon improved knowledge of the role of the structural parameters on the loss and permeability properties, industry has made available to the users a wide range of NO steels. These materials are never isotropic and typically exhibit some 10 % - 20 % variation of the loss figure along different directions in the lamination plane. The top commercial grades have around 4 wt % (Si + Al) concentration and, with a gauge of 0.35 mm – 0.50 mm, they display a power loss figure $P_{15/50}$ of 2.10 – 2.30 W/kg at 1.5 T and 50 Hz, reaching an induction B_{25} = 1.50 – 1.60 T at 2500 A/m. Non-oriented Fe-Si alloys are preferentially employed in medium and high power rotating machines, whereas, as previously stressed, low-carbon steel laminations are preferred in small apparatus. The highest efficiency (> 95 %) is sought in big electrical machines, not only to save energy, but also to avoid overheating and shortened machine life span. For medium-to-high-frequency applications, like high-speed rotating machines, thin fully processed grades with good mechanical properties have been developed. They span a thickness range 0.10 mm - 0.27 mm, as illustrated in Table 6. The related specifications are provided by the Standard IEC 60404-8-8 [41].

The development of improved non-oriented alloys is related to the control of a number of structural parameters, namely impurities, grain size, crystallographic texture, surface state, residual and applied stresses. A few ten ppm concentrations of impurities like C, N, S, O tend to increase coercivity and losses [43]. They can do this directly, by forming precipitates that act as pinning centers for the domain walls, and indirectly, by adversely affecting grain growth and texture. The role of grain size $\langle s \rangle$ is illustrated in Fig.16, where it is observed that the optimal $\langle s \rangle$ value at line frequency is, depending on the composition, around 100 μm – 200 μm, where the total power loss attains a minimum value [44] [45]. This dependence is especially important in clean materials. Fig. 17 shows that a large grain size brings about a decrease of the loss below a few hundred Hz, while the opposite occurs at higher frequencies. This is understood in terms of opposite dependencies on grain size exhibited by the hysteresis loss component W_h, decreasing as $\langle s \rangle^{-n}$, with n = 0.5 – 1, and by the excess loss W_{exc}, approximately increasing as $\langle s \rangle^{1/2}$ [44]. The correlated dependence of W_h and W_{exc} on the average grains size is theoretically predicted [46]. A low impurity content is mandatory for achieving this optimal grain size, because precipitates tend to hinder grain growth. In addition, some particles, like MnS and AlN, segregating at grain boundaries, favour the establishment of a detrimental texture, rich of {111} planes. On the other hand, there are soluted impurities, like Sb and Sn, as well as Mn in very clean steels, that can induce selective growth of those re-crystallized grains that have orientations close to the ideal random cubic texture {100}<0*vw*>. A similar texture can actually be approached, in two-stage reduced alloys, by increasing the Al concentration, up to 1.1 wt % [47] or even 1.8 wt% [48], which permits one to achieve the power loss figure $P_{15/50} \sim 2$ W/kg at 1.5 T and 50 Hz.

The punching operation generates localized residual strains and, consequently, it might affect the loss figure in fully processed materials, where, in general, stress relief annealing is not performed. In large machines, however, an appreciable increase of the magnetic losses could derive from the stresses permanently introduced by stacking and assembling the laminations in the core. The detrimental role of such stresses, especially when they are compressive and are applied in the plane of the lamination, is well documented [49], as illustrated in Fig. 18, and it is empirically accounted for by the machine designers through the introduction of an appropriate building factor in the estimation of the core loss figure [50].

High-Si, Fe-Al, and Fe-Al-Si alloys

Fe-(6.5 wt%)Si alloys are a prospective route to low loss materials [51]. When compared with the conventional Fe-(3 wt%)Si alloys, they exhibit a favourable combination of lowered anisotropy ($K = 2.1 \cdot 10^4$ J/m^3 instead of $K = 3.6 \cdot 10^4$ J/m^3) and increased resistivity ($\rho = 80 \cdot 10^{-8}$ Ω·m instead of $\rho = 45 \cdot 10^{-8}$ Ω·m), which compound with vanishing magnetostriction ($\lambda_{100} = -0.5 \cdot 10^{-6}$, $\lambda_{111} = 2 \cdot 10^{-6}$) to provide a potentially excellent soft magnetic alloy for applications at power and medium frequencies. The reduced magnetostriction additionally yields a definite decrease of the acoustic noise under operating conditions. On the other hand, the saturation polarization is reduced to a certain extent (Fig. 14).

Fe-(6.5 wt%)Si alloys cannot be prepared by cold rolling, because the heterogeneous formation of ordered FeSi (B_2) and Fe_3Si (DO_3) phases during cooling makes them hard and brittle [52]. To avoid ordering,

cooling rates greater than about 10^3 °C/s in the temperature interval 800 °C – 500 °C are needed, a condition that can be satisfied by rapid quenching from the melt. By Planar Flow Casting (PFC), a method where a molten metal stream is ejected onto a rotating metallic drum, ductile Fe-(6.5 wt%)Si ribbons are obtained, with thickness typically ranging between 30 μm and 100 μm. Once annealed in vacuum at 1100 °C – 1200 °C, they exhibit a columnar grain structure (average grain size $\langle s \rangle \sim 100 - 500$ μm) with a prevalent texture (100) <0*vw*> (random cube-on-face). The final ribbons may show, at the price of a somewhat reduced ductility with respect to the as-quenched state, a coercivity lower than 10 A/m and a maximum relative permeability larger than 10^4 and constant up to the kHz region. At 1 kHz and 1 T, the power loss can be lower than 15 W/kg in 50 μm thick ribbons, a value that favourably compares with the loss figure of thinned NO and GO Fe-(3 wt%)Si laminations. Fig. 23 puts in evidence the passage of the total loss W and its structure dependent components (hysteresis W_h and excess W_{exc}) through a minimum value at the 6.7 wt % Si concentration in a rapidly quenched and annealed Fe-Si tapes (thickness $d = 40$ μm). A comparison of the energy loss versus frequency behaviours in conventional NO Fe-(3.5 wt%)Si sheets and rapidly quenched Fe-(6.5 wt%)Si ribbons is provided in Fig. 20.

Fe-(6.5 wt%)Si alloys can also be prepared by Si enrichment of standard NO and GO laminations. Classically, Si enrichment is carried out by means of a Chemical Vapour Deposition (CVD) process, where $SiCl_4$ is used as the donor phase, according to the reaction $SiCl_4 + 5Fe \Leftrightarrow Fe_3Si + 2FeCl_2$ [53]. This process has been developed at industrial scale on NO sheets, resulting in good magnetic properties and fairly good workability [54]. Two types of commercial laminations are offered (JFE Super Cores), the first one homogeneously enriched till 6.5 wt% Si, the second one with a Si concentration profile decreasing from 6.5 wt% at the surface to about 3 wt% at the centre [55]. Such a profile is especially effective in restraining the macroscopic eddy currents, because they tend to concentrate at the lamination surface, and is therefore suitable for high-frequency applications. Table 7 provides a comparison of the magnetic properties of these Si-enriched sheets with conventional NO and GO alloys. Different high-Si core types for applications ranging from high-speed rotating machines to electronic devices are offered. Because of the delicate mechanical handling required by these materials, lamination cutting and core assembling are usually done at the factory.

Solute Al and Si atoms affect in a similar way the physical properties of Fe [56], but Si is preferred in magnetic alloys, because it is less oxygen reacting than Al and is less expensive. Fe-Al alloys are ductile, even when partial ordering occurs (above 7 – 8 wt % Al concentration), but the magnetostriction constant λ_{100} suffers an approximately five-fold increase with respect to pure Fe on increasing Al up to 10 wt % (from $20 \cdot 10^{-6}$ to $\sim 90 \cdot 10^{-6}$). It follows an opposite and unfavourable trend with respect to Si addition and eventually drops around zero for Al concentrations ~ 16 wt %. At the same time, the anisotropy constant follows a monotonic decrease and, depending on the degree of ordering, passes through zero around Al = 11 wt % – 14 wt % [39]. Two compositions have relevance in applications. The Fe-(13 wt %)Al alloy combines high magnetostriction with low anisotropy and is of interest for magnetoelastic transducers. The Fe-(17 wt %)Al alloy is characterized by mechanical hardness and high permeability and is used in magnetic heads. The ternary Fe-(9.6 wt %)Si-(5.5 wt %)Al alloy, known as Sendust, is characterized by an extremely soft magnetic behavior, because the constants K_1, λ_{100}, and λ_{111} all simultaneously approach the zero value. The coercive field can reach values around 1 - 2 A/m and the relative permeability is of the order of 10^5. Sendust alloys are extremely brittle and are therefore used in cast form for DC applications and as powder cores in AC devices.

Further properties and features of non-oriented Fe-Si alloys

1) *Temperature dependence of the magnetic properties.*

The behavior of Fe-Si alloys versus temperature is pretty much the same as that of Fe and low-carbon steels (see the previous Section). The upper working temperature limit is defined either by the properties of the lamination coating or the device itself.

2) *Stress dependence of the magnetic properties.*

Elastic tensile stresses introduce slight changes only (typically, small magnetic softening), while compressive stresses introduce a substantial decrease of the magnetic permeability and an increase of coercivity and losses, as illustrated by the behavior of the total loss at different J_p values shown in Fig. 18 ($f =$ 100 Hz) and the DC hysteresis loops shown in Fig. 21. It is observed in this figure the progressive shearing of the loop under increasing compressive stress σ. The physical reason for this effect lies in the introduction by the stress of an additional magnetoelastic energy term $E_{me} = (3/2)\langle\lambda_s\rangle\sigma$, where $\langle\lambda_s\rangle$ is the averaged isotropic magnetostriction constant. This additional energy term, making the easy axes farther from the stress axis energetically favorable and preferentially occupied by the magnetization, must be overcome by the Zeeman energy $E_H = -\boldsymbol{H}\cdot\boldsymbol{J}$ provided by the field and shows up through loop shearing. In polycrystalline Fe-(3 wt%)Si alloy it is estimated $\langle\lambda_s\rangle \sim 5 \cdot 10^{-6}$ and for $\sigma = 50$ MPa one gets $E_{me} \sim 370$ J/m^3, roughly corresponding to the

additional Zeeman energy estimated directly from the magnetization curves in Fig. 21. Concerning the effect of plastic deformation, we have, as usual in soft magnets, a deterioration of the magnetic properties, as illustrated for the Fe sheets in Fig. 13.

3) *Mechanical properties.*

Fe-Si sheets show increasing mechanical hardness with increasing the Si content (Vickers hardness passing from 130 to 220 in the Si range 1 wt% - 3.5 wt%) and become definitively brittle for Si concentration higher than about 4.5 wt%. The JFE Fe-(6.5 wt%)Si sheets, obtained by CVD enrichment of conventional Fe-(3 wt%)Si, show mitigated brittleness.

4) *Coating.*

Coatings with thickness 0.7 μm - 6 μm and interlaminar resistance ranging between 3 and 200 $\Omega \cdot cm^2$ are applied as a final step in the sheet preparation. They allow for maximum continuous working temperature of 270 °C.

5) *Delivery.*

Non-oriented semi-processed and fully processed electrical steels are supplied as slit coils or cut sheets of width 1.1 m – 1.25 m and length 2.5 m – 3.5 m.

6) *Specifications.*

The grades, general requirements, magnetic properties, geometric characteristics, tolerances, and technological characteristics are defined in the Standards IEC 60404-8-4 [40], IEC 60404-8-6 [37], IEC 60404-8-8 [41].

7) *Applications.*

Non-oriented Fe-Si steel sheets are applied in all kinds of small, medium, and large rotating machines. The thinner grades (Table 6) and the high-Si types are especially suited to high-speed machines, chokes and high-frequency inductors up to a few ten kHz.

Grain-oriented Fe-Si alloys

Fe single crystals exhibit minimum coercivity and maximum permeability when magnetized along one of the <001> axes. This property has fundamental theoretical implications and outstanding practical consequences. In fact, most transformer cores are built today of grain-oriented (GO) Fe-Si laminations, where the crystallites have their [001] easy axis close to the rolling direction (RD) and their (110) plane nearly parallel to the lamination surface (Fig. 22). This is the so-called (110)[001] texture or *Goss texture*, after N.P. Goss, the first to develop such materials. Because of the remarkable texture of the GO alloys, their large grain size (from a few millimeters to a few centimeters) and the little content of impurities, coercive fields as low as 4 – 10 A/m and maximum permeability values around $7 \cdot 10^4$ are obtained. These figures differ by about an order of magnitude from those typically found in NO alloys. Single-phase transformer cores can be made either by rolling up a long lamination or by stacking and suitably joining at the corners separate sheet pieces, *so that the magnetic-flux path is everywhere aligned to RD*. Three-phase cores are always of the stacked type and cover the high power range (starting from some 50 kVA). GO laminations are subdivided in two main classes: conventional grain oriented (CGO) and high permeability (HGO) alloys, characterized by a dispersion of the [001] axes of the crystallites around RD of about 7° and 3°, respectively. Specifications for industrial products are provided in the Standards IEC 60404-8-6 [37], IEC 60404-8-7 [57], and IEC 60404-8-8 [41]. The CGO materials, although less performing than the HGO ones, cover about 80 % of the market. Industrial products are offered with thicknesses usually ranging between 0.23 mm and 0.35 mm and a power loss figure $P_{17/50}$ = 1.40 – 0.80 W/kg at 1.7 T and 50 Hz (see Table 8). GO sheets with thickness lower than 0.20 mm are available for applications in the kHz range. About $3 \cdot 10^6$ ton/year of GO alloys are produced worldwide, with a market value estimated around ◘ $5 \cdot 10^9$.

Preparation methods

Following the original method by Goss, a number of patented processes for the production of GO sheets have been developed, based on various complex thermo-mechanical sequences [58] [59] [60]. Table 9 offers a schematic illustration of the CGO and HGO processing methods. In the case of CGO materials, the main preparation steps can be summarized as follows: (1) Melting in the arc furnace, vacuum degassing and continuous casting. Besides Si, ranging in concentration between 3.0 wt% and 3.2 wt%, the following impurities are usually present: Mn (0.04 – 0.1 wt%), S (0.02 wt%), C (0.03 wt%). (2) Slab re-heating at 1300 °C – 1350 °C, followed by hot rolling to the thickness of 2 mm, annealing at a temperature of 900°C - 1100 °C, and cooling. Times and temperatures along this stage are finely adjusted in order to achieve a homogeneous distribution of precipitates, namely MnS particles with size around 10 - 20 nm. (3) Two-stage cold rolling (~70 % plus ~55 %) to the final gauge, with intervening annealing treatment at 800 °C – 1000 °C. (4) Decarburizing anneal in wet H_2 atmosphere at 800 °C – 850 °C. Since a huge amount of deformation is cumulated by the

previous cold reduction, complete primary re-crystallization takes place at this stage. However, the newly formed grains are strongly inhibited in their growth because of the presence of the finely precipitated MnS impurities. (5) MgO coating, coiling and 48 hour box-annealing at a temperature of 1200 °C. During this final annealing treatment, secondary re-crystallization takes place, where abnormally large and sharply (110)[001] oriented grains grow within the precipitate-stabilized primary matrix and eventually cover the whole sheet. This is thought to occur because these grains have a boundary mobility much larger than the great majority of the primary grains, whose prevalent texture is around {111} <110> and {111} <112>. It is estimated that one in about 10^6 primary grains is (110)[001] oriented, which explains the large final secondary-grain size. At the end of box-annealing the precipitates are completely dissolved and harmful effects on the magnetization process are avoided. (6) Phosphate coating and thermal flattening. The HGO laminations are obtained with some variants to the previous sequence, which lead to sharper Goss texture. Different industrial HGO processes are employed today. In the process summarized in Table 9 [58], a single stage 87 % cold reduction is adopted. The MnS inhibitors are here reinforced with AlN precipitates and partial austenitic transformation, during hot rolling and successive annealing at 1100 – 1150 °C, is achieved by adjusting the C concentration around 700 ppm. With 3.25 wt% Si and 700 ppm C, the γ phase fraction at 1150 °C amounts to 40 – 50 %, which leads to optimal dissolution of AlN and subsequent precipitation of optimally sized particles along the cooling stage. A second method is a two-step cold rolling process which exploits the combined inhibiting action of MnSe precipitates and Sb solute atoms, segregated at grain boundaries [59]. In a third process, solute B, N, and S atoms act as inhibitors and a single-stage cold reduction is again performed [60]. Commercial HGO laminations usually come into the thickness range 0.30 mm – 0.23 mm. To achieve lower gauges while maintaining a comparable textural quality is more difficult. For example, the required 87 % single stage cold reduction in the HGO process would call for a correspondingly thinner hot-rolled sheet, which may not follow the temperature-time behavior ensuring optimal dispersion of the AlN particles. The preparation of thick HGO sheets, (i.e. 0.50 mm gauge) would equally be impaired, because of insufficient decarburization. It has been shown that such difficulties can be overcome and high permeability laminations in wide gauge range (0.18 mm – 0.50 mm) can be produced by promoting the formation of the AlN particles at a later stage, just prior to the secondary recrystallization. This is the so-called "acquired inhibitor method", where N_2 gas is injected into the material after decarburization [61]. Industrial GO products of thickness 0.20 mm and $W_{17/50}$ = 0.82 – 0.91 W/kg are nowadays available [62].

Magnetic domains and magnetization process

The beneficial effects on permeability and coercivity produced by an improved Goss texture are directly related to the morphology of the magnetic domains, which, for a perfect (110)[001] grain, form a bar-like array, with the 180° Bloch walls running along the [001] direction (Fig. 22a). This ideal structure is approached in the HGO sheets, which exhibit the lowest coercivity and the highest permeability among the Fe-Si alloys, thanks to the combined absence of DW pinning centers and the presence of large well-oriented grains. They also exhibit the lowest magnetostriction, eventually resulting into reduced transformer noise. Fig. 22b shows a typical domain structure in well oriented grains of an HGO sheet. It is noticed the presence of spike-shaped supplementary domains, which form when the [001] axis slightly emerges from the sheet plane. Spike domains create closed paths for the magnetic flux, to reduce the magnetostatic energy of the system. In a material with few, wide bar-like domains, like the ones of Fig. 22b, the magnetization reversal, localized at each instant of time at the moving walls, is highly non-homogeneous and the excess loss component W_{exc} (Eq. (10)) is accordingly large. Sharp increase of the loss is also observed on moving the field direction away from the rolling direction (RD) [63]. In HGO materials with neat (110)[001] texture, this feature has detrimental consequences on power losses, because a relatively high W_{exc} contribution can wipe out the beneficial effects on the DC behavior engendered by the excellent textural properties of the material. In order to optimize the material response in terms of permeability and losses, it is expedient to apply, both in CGO and HGO laminations, a coating (thickness ~2.5 μm) capable of exerting a tensile stress of 2 – 10 MPa. This stress leads, via magnetoelastic interaction, to partial or complete disappearence of the flux closing domains, which have a high magnetoelastic energy cost. Under these conditions, the system can reduce its magnetostatic energy by reducing the size of the main bar-like domains, leading to a more homogeneous magnetization process and reduced dynamic losses. However, the energy balance is such that stress-induced domain refinement hardly occurs when the angle made by the [001] axis with the plane of the lamination β < ~1.5 °. For this reason, significant domain multiplication is achieved in the best HGO materials through a combination of magnetoelastic and magnetostatic effects, by scribing patterns on the lamination surface. An array of scribing techniques (e.g. mechanical scratching, laser irradiation, plasma jet scribing, etch pitting) have been devised and are employed in the production of the highest HGO grades. As shown in Table 8, the highest grade HGO products are the scribed 0.23 mm thick sheets, which exhibit a specific power loss $W_{17/50}$ = 0.80 W/kg at 1.7 T and 50 Hz. Further improvements can be envisaged through the following strategies [64]: 1) Achieve perfect

orientation (β <1°) and refine the domain structure by laser scribing; 2) Achieve a smooth lamination surface and remove the oxide layer, in order to minimize domain wall pinning; 3) Decrease the lamination thickness down to 0.15 mm, exploiting the acquired inhibitor method to optimize the secondary recrystallization process.

For applications at medium frequencies (0.4 – 10 kHz) thinned GO laminations are commercially available. They are produced by rolling standard laminations to the reduced gauge of 0.15 – 0.10 mm and carrying out an appropriate heat treatment. Since these alloys present inferior texture and permeability, new processes have been devised in the laboratory in order to achieve highly oriented extra-thin materials [65]. Excellent performances have been obtained in laminations with thickness ranging between 10 μm and 100 μm by adopting, after cold reduction to the final gauge, a special sequence of annealing treatments [66]. These induce a sharply defined (110)[001] texture through a tertiary re-crystallization process, which occurs because the (110) crystallographic planes are those having minimum energy when exposed to the lamination surface. This principle is also at the basis of the preparation of cube-on-face (100)[001] textured Fe-(3 wt%)Si laminations by secondary re-crystallization in a slightly oxidizing atmosphere [67]. Cube-textured Fe-Si laminations are attractive in principle, because the biaxial symmetry introduced by the two easy axes in the lamination plane has a potential for applications both in transformers and rotating machines. However, they are difficult and expensive to manufacture and they are not available at present as industrial products.

Further properties and features of grain-oriented Fe-Si alloys

1) *Temperature dependence of the magnetic properties.*

Same considerations apply to GO and NO laminations, both exhibiting a reduction of the power loss with increasing temperature T. Fig. 23 provides the behavior of the intrinsic magnetic parameters (saturation magnetization J_s, anisotropy constant K_1, magnetostriction constants λ_{100} and λ_{111}) and the electrical resistivity ρ versus T [68] [69]. The energy loss at power frequency decreases, more or less linearly, by some 20 % on increasing T from room temperature up to 400 °C [68]. The decrease of the quasi-static loss W_h with T is chiefly related to the decrease of K_1, which is feebly countered by a corresponding slight increase of λ_{100}. The increase of the resistivity with T provides a concomitant reduction of the dynamic loss component $W_{dyn} = W_{cl} + W_{exc}$. In practice, the upper temperature for continuous use is not imposed by the material properties but by the heat resistance (e.g. electrical insulations) of the device.

2) *Stress dependence of the magnetic properties.*

Elastic tensile stresses applied along the Rolling Direction are slightly beneficial, while drastic deterioration of the permeability and loss figures occurs with the application of a longitudinal compressive stress. Fig. 24 provides an example of this effect [70] [71]. Again, the magnetostrictive interaction makes, for a compressive stress applied along RD, the [001] direction in each crystallite energetically unfavourable. The other two <100> directions, transverse to RD (Fig. 22a) are now preferentially occupied and the magnetization process becomes more difficult, because the additional barrier offered by the magnetoelastic energy term must be overcome for the domain process to proceed. The detrimental effect of plastic straining is apparent upon lamination punching. It is observed in HGO sheets that strip shearing over a 100 mm width might still account for about 5 % increase of the loss. Stress relief is therefore frequently required. This is typically carried out between 760 °C and 840 °C. Laser-scribed sheets cannot, however, be subjected to annealing, because this would reverse the reduction of core loss by the domain refinement.

3) *Mechanical properties*.

Grain-oriented Fe-Si laminations are relatively hard from the mechanical viewpoint (Vickers hardness around 200) and lamination shearing and punching can be performed with good accuracy and minimum burr height.

4) *Coating.*

The grain-oriented laminations are covered on both sides with a thin inorganic coating, which is applied over the glass film layer, which is formed during the high temperature annealing process. The coating is approximately 2.5 - 3 μm thick per side and provides good electrical resistance with only a marginal effect on the stacking factor. The coating has good adhesive properties and can withstand normal punching operations, besides resisting annealing up to 840 °C. It additionally exerts a tensile stress of 2 – 10 MPa, which not only leads to loss reduction, but also to reduced magnetostriction and noise in transformers. The coating is chemically resistant to any fluid contamination during the production process, gives some protection against corrosion, and is unaffected by different types of transformer oils.

5) *Delivery.*

Grain-oriented electrical steels are supplied as slit coils or cut sheets of typical width 100 mm – 900 mm and length up to 3 m.

6) *Specifications.*

The grades, general requirements, magnetic properties, geometric characteristics, tolerances, and technological characteristics are defined in the Standards IEC 60404-8-6 [37], IEC 60404-8-7 [57], and IEC 60404-8-8 [41].

7) *Applications.*

Grain-oriented electrical steel is employed in the manufacture of energy efficient transformers and large, high performance generators. The advantage of using GO materials instead of the usual NO laminations in the axial flux permanent magnet rotating machines has been recognized [72].

SOFT MAGNETIC COMPOSITES (POWDER CORES)

For applications in the medium frequency range (from a few hundred Hz to a few ten kHz) and those instances where specially shaped cores, hardly achievable by lamination stacking, are required, powder cores provide an attractive solution. One deals in this case with relatively isotropic materials, which appear especially suited for applications where three-dimensional flux paths are established [73] [74] [75]. The main industrial products are based on pure Fe powders, but soft magnetic composite (SMC) cores obtained starting from Fe-P, Fe-Si, Fe-Co alloys are also available. Composites obtained by compaction of amorphous and nanocrystalline particles have also been widely investigated in the literature [76] [77] [78], but the related industrial production is still limited [79]. Soft magnetic composites are obtained either as sintered or compacted products. Sintered cores combine a resistivity approximately doubled with respect to the one of the starting bulk material with good soft quasi-static magnetic behavior. Their use is generally restricted to DC applications. Compacted cores have very high resistivities, ranging between $50 \cdot 10^{-6}$ Ωm and $1000 \cdot 10^{-6}$ Ωm, which depend on the particle size, compacting pressure and heat-treatment temperature. Since an insulating layer separates the individual particles, the eddy current paths are mostly confined within the grains and the dynamic magnetic losses are correspondingly reduced. These materials become in general attractive from the viewpoint of losses in the kHz range.

Preparation methods

The preparation process starts with the production of the particles, generally by means of an atomisation process, except for the case of nanocrystalline alloys, which are intrinsically hard and brittle and can be pulverized by milling. Preparation by water atomization is schematically described in Fig. 25. Crystalline particles of roughly spheroidal shape and average size $\langle s \rangle$ ranging between 5 μm and 200 μm are obtained. Amorphous alloy particles have been successfully obtained by the Spinning Water Atomization Process (SWAP) [77]. With this method, tiny liquid droplets are first obtained pulverizing the molten alloy pouring from the crucible by means of a nitrogen gas jet and are subsequently ejected and quenched as amorphous particles ($\langle s \rangle \sim 50$ μm) into a spinning water stream. Figs. 26a and 26b show the morphology of the Fe crystalline particles [73] and the Fe-based amorphous particles [77] obtained by these two processes. The micrographs in Figs. 26c and 26d provide a cross-sectional view of the particle assembly after compaction [80] [81]. In this process, the particles are electrically insulated by a dielectric and a binder is usually added. The powder is mixed with a lubricant (0.5 wt%), poured into a die and compressed at a pressure of 600 – 800 MPa. Warm compacting (up to 150 °C) is generally adopted, in order to increase the final composite density, that is, the final saturation polarization [82] [83]. This process permits one to manufacture net-shape parts, without need for further tooling. It is followed by annealing in air at temperatures ranging between 300 °C and 500 °C, which leads to partial dissolution of the lubricant and stress relaxation, the final density of the magnet being around 6800 – 7400 kg/m^3. High annealing temperatures are beneficial from the viewpoint of the mechanical properties and DC magnetic behavior, but they are detrimental for AC magnetic losses, as shown in Fig. 27. An intermediate curing temperature is therefore chosen (for example T_a = 450 °C), by which acceptable mechanical strength is achieved. The sintered materials are treated after compaction at a temperature of the order of 1150 °C – 1300 °C, after which they reach a density about 2 % lower than the density of the individual particles. Otsuka, et al., [77] coated the amorphous particles obtained by SWAP by a low melting temperature phosphate glass (1 % volume), compacted the conglomerate with 2GPa pressure, and annealed it at 415 °C.

Magnetic properties

Being finely subdivided and, consequently, characterized by a distributed air gap, the iron powder cores exhibit a sheared hysteresis loop and relatively low values of the permeability ($\mu_r \sim 100$ - 500). This effect is apparent in Fig. 28, where the DC hysteresis loops at peak polarization J_p = 1.25 T of a non-oriented

Fe-(3 wt%)Si lamination and of two SMC Fe cores with different densities (i.e. Fe filling factor) are compared. From the slope of the loops around the coercive field it is estimated that the distributed air gaps play the role of an effective macroscopic demagnetizing coefficient $N_{d,eff} \sim 1.8 \cdot 10^{-3}$ and $N_{d,eff} \sim 3.3 \cdot 10^{-3}$ in the higher (δ = 7450 kg/m^3) and lower (δ = 7260 kg/m^3) density composites, respectively. It is noted in Fig. 28 that the grain-to-grain magnetic decoupling is conducive also to about an order of magnitude increase of the coercive field with respect to the silicon steel sheet. The lack of any large-scale electrical conductivity, however, can provide comparable or even superior loss behavior with respect to Fe-Si and low-carbon-steel laminated cores at high frequencies. In addition, a nearly frequency independent permeability is generally obtained up to 10 - 100 kHz. A comparison of the magnetic energy losses from DC to 10 kHz at J_p = 1.0 T in high-performance Fe-Si non-oriented sheets and an industrial Fe-based SMC core sample (density δ = 7450 kg/m^3) is provided in Fig. 29. To be remarked that in many cases the loss decomposition according to Eqs. (8) – (10) cannot be straightforwardly applied to SMC cores [84], because the eddy currents are not fully delimited by the imperfectly insulated particle boundaries and can flow from particle-to-particle via random contacts. A scenario therefore occurs, where mesoscopic currents circulating inside the particles grains are associated with macroscopic currents encompassing a large number of particles. By means of a numerical model, emulating the actual particle assembly and the random character of the interparticle conductive connections, the classical eddy current loss component W_{cl} can nevertheless be calculated. It can be described, in particular, as the sum of two terms, microscopic and macroscopic, and related to the actually measured resistivity of the SMC sample, thereby making the loss decomposition procedure still appropriate [85].

Further properties and features of Soft Magnetic Composites

1) Temperature dependence of the magnetic properties.

Fe-based SMCs have their properties depending on temperature like their bulk counterpart. The maximum continuous working temperature for coated samples is around 200 °C, the limit being posed by the temperature resistance of the plastic coating.

2) Mechanical properties.

Soft magnetic Fe composites have negligible plastic deformation and fracture strength, depending on the final annealing temperature. After a typical treatment at 450 °C, the transverse fracture strength is around 100 MPa. Sintered composites have fracture strength increased to 200 – 300 MPa. These materials can be usually be machined with conventional tools.

3) Delivery.

Many applications of soft magnetic composites call for the classical ring samples, which are available with diameters ranging between a few mm to about 100 mm. Bulk samples in the form of cylinders and disks (down to a few mm thickness) are generally available and the capability to produce net-shape SMCs can be exploited, in order to achieve suitably designed final parts.

4) Applications.

The conventional SMC cores, either as closed ring samples or cut cores, are increasingly used as power inductors, specifically in switch-mode power supplies. Other power applications include differential inductors, boost inductors, buck inductors, flyback transformers, high-Q filters, load coils, flux concentrators. Most interesting applications are found in the rotating machines [86] [87] [88] [89]. One takes profit in this case of the quasi-isotropic behavior of the material, allowing for the establishment of three-dimensional flux paths and the related additional degree of freedom in machine design. It is required that this 3D advantage be fully harmonized in the design, in view of the generally inferior soft magnetic properties of SMCs with respect to conventional Fe-Si sheets, as put in evidence by the DC hysteresis loops shown in Fig. 28 and the illustrative energy loss behaviors shown in Fig. 29.

Thus, while an outright substitution of the laminated core with an SMC one is expected to result in a reduced machine performance, suitable exploitation by design of the available 3D geometries can be effective in achieving improved efficiency and reduced mass in rotating machines. Permanent magnet motors appear especially prone to improved performances by use of SMC cores. Transverse flux, axial flux, and claw-pole machines are among the devices successfully developed making use of compacted composite cores, resulting in increased efficiency, decreased size, and decreased volume of the permanent magnets. A noted advantage of the 3D design is the reduction of the winding length, with reduced copper loss and weight. It is possible, for example, to adopt rounded teeth, allowing for tighter and shorter winding, with higher slot filling factor. A possibly higher iron loss, compared with laminated cores, is therefore compensated by lower copper loss. Volume reduction by use of an SMC stator core in brushless permanent magnet motors has been demonstrated [87][88].

AMORPHOUS AND NANOCRYSTALLINE ALLOYS

Preparation of amorphous alloys

Amorphous soft magnetic materials are obtained as thin ribbons by means of rapid solidification. Today, the predominantly employed rapid solidification technique is the Planar Flow Casting (PFC), by which one can prepare ribbons of variable width (up to 100 - 200 mm) and thickness usually ranging between 15 μm and 40 μm. In a typical PFC setup (Fig. 30a), a quartz crucible, which holds the liquefied master alloy, is placed nearly in contact with the surface of a rotating metallic drum, which drags the liquid at a velocity of 10 – 40 m/s. This ensures a cooling rate of the order of 10^5 - 10^6 °C/s, sufficient to undercool the alloy through the glass transition temperature T_g, where it achieves the typical viscosity of a solid, retaining, at the same time, the disordered atomic arrangement of a liquid (Fig. 30c). Narrow ribbons can also be produced by means of the Chill Block Melt Spinning technique (Fig. 30b), of which PFC is a derivation. With a more complex method, the so-called in-water-quenching technique, amorphous wires, of 50 μm – 100 μm diameter, are prepared [90]. In this case, the molten metal jet is plunged into rotating water. Glass-coated amorphous wires are prepared by the Taylor extraction technique, where a tiny master alloy ingot, held at the bottom of a glass tube, is heated by a radiofrequency inductor up to the melting point. The softened end of the tube, enclosing the molten metal, is pulled at suitable speed through a stream of water and a glass capillary is obtained enclosing the metallic core, having a diameter of a few micrometers [91][92].

Metallic amorphous alloys can also be prepared in bulk form, by adopting comparatively low rates of cooling from the melt, when their glass transition temperature T_g and melting temperature T_m have relatively close values ($T_g/T_m \sim 0.7$) and the crystallization temperature is also appreciably lower (some 10 to 30 K) than T_g [93]. This condition can be achieved with multicomponent systems, where the atomic sizes of the main constituent elements are significantly different. Long range atomic rearrangements are required for the achievement of the crystalline state on cooling from the melt and time then suffices to freeze the amorphous state by adopting conventional copper mould casting. Examples of soft amorphous alloys obtained in bulk form (for example, cylinders with diameters of a few millimeters) are $Fe_{80}P_{12}B_4Si_4$, $Fe_{76}Al_4P_{12}B_4Si_4$, $Fe_{74}Al_4Ga_2P_{12}B_4Si_4$ [94].

Properties and applications of amorphous ribbons

The general composition of soft magnetic amorphous alloys is $T_{70\text{-}80}M_{30\text{-}20}$, where T stands for one or more of the transition metals Fe, Co, and Ni, and M is a combination of metalloids (e.g. B, Si, P, C). The metalloid atoms, with their radius much smaller than that of Fe, Co, and Ni, play an indispensable role as glass formers, besides providing the eutectic composition required for the safe achievement of the amorphous state. Lack of crystalline order does not prevent the formation of ferromagnetic order. The existence of a large-scale magnetic moment is in fact basically unaffected by structural disorder, although its strength is reduced by the presence of the metalloids [95].

The Ni atoms do not apparently contribute to the total magnetic moment and the magnetic glasses are usually classified as Fe-based or Co-based. The Curie temperature T_c of an amorphous alloy is found to be lower than that of the corresponding crystalline alloy, with the remarkable property that in the Fe-based materials it decreases when the proportion of Fe is increased, pointing to an extrapolated minimum T_c value for hypothetical pure amorphous Fe. This is justified in terms of local coordination of the Fe atoms in the amorphous environment, which is different from the one associated with the ferromagnetic b.c.c. structure of crystalline iron [96]. Fig. 31 shows that the saturation magnetization decreases by a noticeable amount when passing from the Fe-based to the Co-based composition in the representative alloy $Fe_xCo_{80\text{-}x}B_{20}$ [96].

The mean free path of conduction electrons in glassy metals is limited by the atomic disorder to a few interatomic distances, and the electrical resistivity is consequently increased by a factor 2-3 with respect to their crystalline counterpart, besides being quite independent of temperature. At the same time, plastic slip is highly limited, because no dislocation glide is possible and a very high fracture stress $\sigma_r \sim 2800$ MPa is obtained, with cumulated strain $\varepsilon_r \sim 2.5$ %. The ratio E/σ_r, where E is the Young's modulus, attains a value ~50, which is typical of high-strength materials and makes amorphous alloys interesting for structural applications. As summarized by the parameters presented in Table 10, the disordered atomic structure provides a unique combination of mechanical hardness and magnetic softness, the latter coming from a subtle mechanism which involves the competition between the exchange interaction responsible for ferromagnetic order and the local anisotropies. One may actually describe an amorphous alloy as a random ensemble of

structural units, each extending over a distance δ equal to a few atomic spacings. Each unit has definite symmetry properties and is therefore characterized by local magnetocrystalline anisotropy oriented at random. In 3*d*-based alloys, where the anisotropy constant K is of the order of 10^4 - 10^5 J/m^3, the torque by K is not sufficient to force the local alignment of the magnetization alongside the easy axis of the individual structural units, because the exchange interaction maintains the spins aligned over a correlation length $L_{ex} >> \delta$. The effective magnetocrystalline anisotropy K_0 of the material becomes then the average of the local anisotropies over distances of the order of L_{ex} and is reduced to a pretty low value, as previously discussed (see Eq. (7)). This negligible value of the average magnetocrystalline anisotropy is the key to the soft magnetic properties of the amorphous alloys. In fact, under these conditions, coercivity and permeability are only due to either residual anisotropies of magnetoelastic origin or the induced anisotropies created by suitable magnetothermal treatments (field annealing, stress annealing, etc.). A stress σ causes a uniaxial anisotropy $K_\sigma = (3/2)\lambda_s\sigma$ in a material characterized by the saturation magnetostriction constant λ_s. This value provides a sort of "a priori" indicator of the achievable ultimate soft magnetic properties of a given amorphous alloy. Fig. 31 shows that in the representative composition $Fe_{80-x}Co_xB_{20}$ the constant λ_s strongly depends on the relative proportions of Fe and Co. It ranges from positive to negative values (from ~$30\cdot10^{-6}$ to ~$-3\cdot10^{-6}$) on passing from the Fe-rich to the Co-rich side and intersecting the value $\lambda_s \sim 0$ at Fe concentrations around 5 - 8 at%. In the highly magnetostrictive Fe-rich alloys, the random distribution of internal stresses introduced during the rapid solidification, typically of the order of 50 – 100 MPa, is the source of complex anisotropy patterns, with stress anisotropy K_σ values in the range of some 10^2 - 10^3 J/m^3, hindering the magnetization process and causing increased coercivity [97]. These stresses can never be completely relieved by annealing, because the treatment temperatures are in any case limited by the necessity of avoiding even the slightest precipitation of crystalline phases. After carefully controlled annealing under a saturating longitudinal field, the Fe-based ribbons reach at best coercive fields of 2- 3 A/m.

The influence of stress anisotropies becomes negligible in the vanishing magnetostriction Co-rich alloys. Accordingly, these materials exhibit low energy losses and high permeability at all frequencies. In addition, their properties can be tuned to specific needs by suitable thermal treatments under a saturating magnetic field. These can induce a large-scale anisotropy K_u, as a consequence of localized atomic rearrangements, having a definite directional order. Being the dominant form of anisotropy present in the material, K_u fully governs coercivity, permeability and loop shapes, as illustrated in Fig. 32, which shows the evolution of the DC hysteresis loop upon transverse field annealing in the $Co_{71}Fe_4B_{15}Si_{10}$ amorphous ribbons. The near-zero-magnetostrictive Co-based alloys display then softness and versatility and compare favorably with soft ferrites and Fe-Ni alloys. With prevailing transverse induced anisotropy K_u, the rotation of the magnetic moments is the chief magnetization mechanism and the associated permeability is approximately given by $\mu_r\mu_o = J_s^2 / 2K_u$. Since the domain wall processes are largely suppressed, the loss is minimized and excellent high frequency properties are obtained. The extra-soft magnetic properties of the Co-rich compositions are obtained at the expense of a substantial reduction of the saturation polarisation with respect to the Fe-based alloys (0.9 – 0.5 T versus 1.3 – 1.6 T). This compounds with the obvious cost of Co, so that the related alloys are reserved for specialized applications. Fe-based alloys can actually reach saturation polarizations as high as 1.8 T, but this requires the presence of about 20 at% Co, which is not desirable from the viewpoint of costs.

Table 11 summarizes the behavior of the main physical parameters of a number of common amorphous alloys. Fe-based alloys can advantageously replace the high permeability GO Fe-Si laminations in transformers. In fact, core loss reduction by a factor 2 – 3 can be obtained at 50 Hz on passing from GO to amorphous $Fe_{78}B_{13}Si_9$ laminations (Fig. 33 [98]). The loss analysis puts in evidence that this is due to a drastic reduction of the excess and classical loss components, brought about by the combination of low ribbon thickness and high material resistivity.

In recent years, increasing emphasis on energy saving has favored the introduction by electrical utilities of distribution transformers made of amorphous alloy cores, especially in the single-phase low power range (10 –50 kVA). These devices are characterized by reduced total ownership costs, regarding both purchasing and operating costs along the device lifetime, besides exhibiting good stability over time [98][99]. With the development of improved Fe-based amorphous alloys and increasing pressure to decrease CO_2 emissions worldwide by efficient distribution of the electrical energy, high-rating transformers (MVA range) are increasingly built with amorphous Fe-based cores. The recent development by Metglas Inc. of a high saturation alloy (HB1 alloy, J_s = 1.65 T) has been heralded as a significant step towards high-efficiency high-rating transformers. Table 12 shows the case of a 500 kVA three-phase transformers, where reduced volume, and audible noise are obtained using this amorphous alloy in place of the standard amorphous alloy SA1 (J_s = 1.56 T), while preserving the same strong reduction of the no-load loss with respect to the HGO based transformer [98]. Fig. 34 additionally shows how the exciting power is similarly reduced with the HB1 alloy. It is remarked

that, with the increasing use of non-linear loads, like variable speed motors, personal computers, telecommunication devices, etc., higher harmonics are introduced in the system and the losses are accordingly increased. This is one additional reason for adopting amorphous-cored distribution transformers.

Significant use of amorphous alloys is made in electronics [100]. For instance, Co-based alloys are ideal as cores of inductive components to be employed up to frequencies of the order of 1 MHz, as found, for instance, in the switch-mode power supplies and in digital telecommunication circuits. Their low J_s value is not a disadvantage in these cases, because, in order to limit core heating, the working induction is always kept small. The unique combination of high elastic limit and high magnetostriction in the Fe-based materials is exploited in high-sensitivity sensors and transducers. Further applications include electromagnetic interference filtering, magnetic heads, various types of magnetic shielding and ground fault interrupters.

Amorphous wires

Amorphous wires, either glass-coated or prepared by the water-quenching technique, exhibit a bistable magnetic behavior, regardless of the sign of the magnetostriction. This property derives from the special domain structure that is formed in the wire, typically made of an active longitudinal core, reversing its magnetization with a single Barkhausen jump, and an outer shell, having either radial or circumferential domains. The origin of such a structure is to be found in the anisotropies induced by the large stresses frozen-in during the solidification process, in association with the anisotropy of magnetostatic origin (shape anisotropy). The switching-like behavior of the magnetization reversal in amorphous wires can be exploited in a number of applications, like jitter-free pulse generators, digitizing tablets, speed and position sensors, anti-theft devices. A further remarkable property of amorphous wires is that their reactance at MHz frequencies can change to a large extent upon application of a DC field (giant magnetoimpedance effect) [101]. For instance, variations $\Delta X/X \approx 0.1 - 1$ under an applied field of 100 A/m can be found in Co-based amorphous wires [102]. This effect originates in the strong variation of skin depth with the variation of the domain structure imposed by the DC field and has a potential for many types of magnetic field sensors.

Nanocrystalline alloys

Amorphous alloys tend to crystallize heterogeneously upon annealing, with scattered nucleation and growth of microcrystals taking place at temperatures well below the bulk transition to the crystalline state. This has detrimental consequences on the soft magnetic behavior of the material, besides being associated with drastic mechanical embrittlement. Fe-based alloys actually need stress-relief annealing in order to achieve optimized magnetic properties, but early heterogeneous formation of microcrystals of 0.1 – 1 μm size brings about a sharp increase of the coercive field before full stress relief is achieved [103]. In Fe-Si-B alloys, however, it is possible to achieve both homogeneous grain nucleation and restrained grain coarsening by the addition of Cu and Nb [104]. In particular, by treating amorphous ribbons with composition $Fe_{73.5}Cu_1Nb_3B_9Si_{13.5}$ (FINEMET) at a temperature around 540 °C - 550 °C, a homogeneous nanocrystalline structure is obtained, composed of α-Fe-(~20 at%)Si grains, having dimensions of the order of 10 nm, embedded in a residual Nb-rich amorphous matrix. The crystallites occupy about 70 % of the material volume and are separated by 1 – 2 nm thick amorphous layers. Quite a similar structure can be obtained in alloys with composition $Fe_{91-84}(Zr, Nb)_7B_{2-9}$ (NANOPERM), where the crystalline phase is made of α-Fe grains [105]. Since the grain size δ is much smaller than the correlation length L_{ex} and the intervening amorphous phase ensures grain-to-grain exchange coupling, conditions similar to those found in amorphous structures are created, leading to vanishing crystalline anisotropy. In particular, with the average size of the nanograin $\delta = 10$ nm, $K_1 = 4 \cdot 10^4$ J/m^3, and $A \sim 10^{-11}$ J/m, we obtain from Eq. (7) the average magnetocrystalline anisotropy $K_0 \sim 2.5$ J/m^3, with the scale of the exchange length expanded to the micrometer size. This feature does not come alone, because also magnetostrictive anisotropies average out to vanishing values. In fact, there is a balance in the material between the negative magnetostriction of the crystalline phase and the positive magnetostriction of the amorphous phase. Any applied or residual stress may generate anisotropies at the nanometer scale, having directions dictated by the nature of the stress (tensile/compressive) and the sign of the magnetostriction constant, but, again, the exchange interaction acts to suppress any mesoscopic and macroscopic anisotropy. Eq. (7) suggests that the coercive field, which can be roughly estimated to be proportional to the average anisotropy constant K_0 [9], increases with the sixth power of the grain size δ. The experiments show that this relationship is verified to a good approximation up to $\delta \sim 100$ nm [106], a limit beyond which the coercive field starts decreasing with increasing δ. Fe-based nanocrystalline alloys emulate the properties of the amorphous Co-based alloys, with the advantage that one can deal with inexpensive raw materials, while achieving much higher saturation magnetization (e.g. 1.24 T in $Fe_{73.5}Cu_1Nb_3B_9Si_{13.5}$ and 1.63 T in $Fe_{91}Zr_7B_2$ versus 0.61 T in $Co_{67}Fe_4B_{14.5}Si_{14.5}$ and 0.86 T in $Co_{71}Fe_4B_{15}Si_{10}$) and improved thermal stability. It has been shown that further increase of the saturation magnetization in nanocrystalline alloys can be obtained in Co-containing materials, like those having general composition (Fe, Co)-M-B-Cu (HITPERM), where M ≡ Zr, Nb, Hf. One can attain in

them a very high Curie temperature, up to about 900 °C, and J_s values close to 2 T, with the relative initial permeability around a few 10^3 [107]. It has also been found that significant increase of J_s can be achieved by adding Co to the FINEMET-type alloys, at the expenses of the Si content [108]. With the composition $Fe_{53}Co_{30}Cu_1Nb_7B_8Si_1$, one obtains J_s = 1.71 T and H_c = 6 A/m. Significant progress has been achieved in recent times with the introduction of the novel Fe-rich compositions Fe-Si-B-P-Cu (NANOMET) [109][110] [111]. They are characterized by high saturation polarization (J_s > 1.80 T) and coercive field lower than 10 A/m. These properties descend from a fine structure made of Fe-α nanocrystals surrounded by a thin amorphous layer, which is formed upon annealing at a temperature of the order of 420 °C. The composition $(Fe_{85.7}Si_{0.5}B_{9.5}P_{3.5}Cu_{0.8})_{99}C_1$ is endowed with H_c = 4.5 A/m, J_s = 1.83 T, and power loss at 1.7 T and 50 Hz $P_{1.7/50}$ = 0.38 W/kg [111].

The hysteresis loop of nanocrystalline alloys is sensitive to field annealing. The magnetization-induced atomic ordering mechanism in FINEMET alloys invests the crystalline Fe-Si phase and is less effective than in the Co-based amorphous and nanocrystalline alloys. In any case, nearly linear, low-remanence hysteresis loops can be achieved by suitable treatments under transverse field, similar to the behavior (Fig. 32) displayed by the hysteresis loops in the Co-based amorphous alloys. The linearization of the loop ensuing from the induced transverse anisotropy $K_{u\perp}$ (Fig. 35) leads to low power losses [112] and high permeabilities up to frequencies in the MHz range.

Pretty high uniaxial anisotropies, up to some kJ/m^3, can be induced in amorphous and nanocrystalline ribbons by annealing under tensile stress [113] [114], an effect that is thought to descend from thermally activated anelastic creep and ensuing redistribution of the atomic bonds in the amorphous phase, which are frozen-in upon cooling and stress removal [115]. The induced anisotropy in nanocrystalline ribbons is proportional to the applied stress σ and can be either longitudinal or transverse, according to the Si concentration [116]. With Si > 10 %, the transverse ribbon axis becomes an easy axis, as illustrated by the evolution with σ of the DC magnetization curves shown in Fig. 36 for a Finemet-type composition.

A schematic illustration of how the various amorphous and nanocrystalline alloys relate among themselves and other soft magnets in terms of initial permeability and coercive field versus the saturation polarization is given in Figs. 6 and 7, while the base parameters of different types of nanocrystalline alloys are listed in Table 13 [16]. Fig. 37 shows how the medium-to-high frequency range magnetic power losses displayed by optimally treated nanocrystalline and amorphous alloys favorably compare with the losses found in conventional crystalline soft magnets.

Further properties and features of amorphous and nanocrystalline alloys

1) *Temperature dependence of the magnetic properties.*

Amorphous alloys are metastable materials and have relatively low Curie temperature (see Table 11). Their properties are normally stabilized by stress-relaxation annealing and the maximum continuous service temperature is typically of the order of 150 °C in Fe-based alloys and 90 – 110 °C in Co-based and Ni-based alloys. This is totally adequate for most applications, including distribution transformers, whose stability over aging has been fully verified [99]. There is a slight decrease of the coercive field and increase of the DC permeability of the amorphous alloys on going from room temperature to the maximum continuing service temperature, because the induced anisotropies tend to decrease. The available induction swing under pulsed applications is, however, bound to decrease, following the corresponding decrease of the saturation magnetization, which is, up to about 150 °C, of the order of a few percent in Fe-based alloys and 10 – 15 % in Co-based alloys. The dynamic magnetic behavior is, at the same time, little affected, because the electrical resistivity is quite independent of temperature. The continuous service temperature in nanocrystalline alloys is similarly around 150 °C. These materials, having been subjected to a preparatory treatment around 550 °C, are stable and show little decrease of the permeability and increase of coercivity up to 150 °C [117][118] (see Fig. 38), related to the loosening of the grain-to-grain exchange interaction. On approaching the Curie temperature of the intergrain amorphous phase ($T_{c,am}$ ≈ 290 °C), the Fe-Si nanograins become fully decoupled and the anisotropy constant sharply increases, bringing about more than an order of magnitude increase of the coercive field and decrease of the permeability [16]. It is noted that the thermal resistance of windings and core holder may often be a good reason for keeping the maximum service temperature below 150 °C.

2) *Stress dependence of the magnetic properties.*

While Co-based amorphous alloys have vanishing magnetostriction and correspondingly little stress sensitivity, Fe-based alloys, having high and positive magnetostriction constant $\lambda_s \approx +37 \cdot 10^{-6}$, display high magnetoelastic sensitivity, a property favouring the application of these alloys as stress sensors. For example, the magnetization curve can pass from quasi-linear to quasi-steplike, as a result of combined transverse induced anisotropy $K_\perp$ and longitudinal stress-induced anisotropy $K_{//} = (3/2)\,\lambda_s\sigma$. Magnetostrictive energy harvesters have been built around such an effect [119]. Stress sensitivity plays, however, a detrimental role on

the properties of wound cores. Ribbon bending generates a mixture of tensile and compressive stresses, with the latter bringing about a strong increase of the loss [120]. It is then observed that on decreasing the radius R of toroidal cores, thereby increasing the maximum tensile/compressive stress according to $\sigma_{max} = E_Y d / 2R$, where E_Y is the Young modulus of the material and d is the ribbon thickness, the magnetic loss shows a remarkable increase [121]. Stress relaxation by annealing is therefore required in order to recover, at least in part, good soft magnetic properties. This operation may be a critical one, because the annealing temperature must be far lower than the crystallization temperature. This permits one to avoid the early formation of scattered microcrystals, acting as strong pinning centres for the domain walls and leading to sharp increase of the coercive field. For example, in the common $Fe_{78}B_{13}Si_9$ alloy, having crystallization temperature of 550 °C, the maximum annealing temperature is around 400 °C [103]. Remarkably, no appreciable plastic straining can be achieved in amorphous alloys, which display a unique combination of high mechanical strength and soft magnetic behavior (see Tables 1 and 2). On the other hand, annealed amorphous alloys tend to be brittle and the thermal treatment is preferably made on the final core. This is mandatory with nanocrystalline alloys, because they are extremely brittle. They are therefore delivered either as precursor amorphous alloys or as fully encased cores.

3) *Mechanical properties*.

As-quenched amorphous alloys display very high mechanical hardness (Vickers hardness around 800) and strength and are practically free from plastic deformation. They tend to become brittle after stress-relaxation annealing and all cutting operations should be performed before the thermal treatment. Machining is difficult and laser or water-jet cutting are preferred to traditional punching by cutting tools. Nanocrystalline alloys are extremely brittle and cannot be mechanically handled after the thermal treatment, although some ductility may remain if annealing is performed by Joule heating [122].

4) *Coating.*

Amorphous ribbons are delivered without coating. Ribbons used in tapewound amorphous/nanocrystalline commercial cores may be subjected to coating by a very thin MgO layer before winding [123]. The typical lamination factor ranges between 80 % and 90 %.

5) *Delivery.*

Amorphous alloys are typically supplied as ribbons of variable width (5 mm – 100 mm) and thickness around 20 – 30 µm. Tapewound heat-treated cores are offered either encased in a plastic container or epoxy coated and ready for applications. Nanocrystalline materials are sold as final cores with a large variety of diameters, typically ranging from 10 mm to 150 mm. Table 14 lists the physical and magnetic parameters of representative commercial amorphous alloys.

6) *Applications*.

Amorphous alloys are efficient and versatile materials and find room in all applications of the electrical engineering and a multitude of electronic devices. In particular, Fe-based alloys appear, as previously stressed, real breakthrough materials for large scale adoption of highly efficient distribution transformers. Their use in rotating electrical machines is so far limited, because of the difficulties and costs involved with lamination cutting and assemblage and the resulting poor mechanical properties of the core. Highly efficient switched reluctance motors have nevertheless been developed in recent times [124]. Fig. 52 shows that the efficiency of such a motor, reaching 95 %, is far higher than the one of an identical motor built with conventional NO Fe-Si steel. Patented methods are available for the construction of motors with amorphous cores [125]. Besides electrical machines, Fe-based and Co-based amorphous alloy cores and are conveniently employed in current transformers, ground fault interrupters, high-frequency inductors, magnetic sensors, switch-mode power supplies, electromagnetic shields. Same applications are envisaged for the nanocrystalline alloy cores.

NICKEL-IRON AND COBALT-IRON ALLOYS

Ni-Fe alloys: structure and magnetic properties

Nickel-iron alloys display a broad range of magnetic properties and a well-defined structure in the range 35 % ≤ Ni ≤ 80 %. A stable random f.c.c. solid solution (γ phase) can be obtained above 35 % Ni by choice of annealing temperatures and suitably high cooling rates, with possible addition of elements like Mo, Cu and Cr. The $\gamma \rightarrow \alpha$ phase transition on cooling from high temperatures occurs at $T <\sim 500$ °C, but, because of the low diffusion rate, it can be easily restrained, together with the formation of the ordered Ni_3Fe phase, by rapid cooling. Structural stability and homogeneity are conducive to good mechanical properties and ease in cold rolling, down to thicknesses as low as 10 µm.

The variety of magnetic behaviors achieved in the final Fe-Ni laminations is rooted in the remarkable evolution of the intrinsic magnetic parameters with composition and treatment shown in Fig. 40. It is noticed that both the magnetocrystalline anisotropy constant K_1 and the magnetostriction constants λ_{100} and λ_{111} pass through the zero value in the Ni-rich side, with a positive K_1 value, associated with a <100> easy axis, co-existing with the γ - phase up to ~75 wt% Ni. Compositions with Ni < 30 wt% are ill defined from the structural viewpoint and bear little interest as magnetic materials. The $Fe_{70}Ni_{30}$ (wt % composition) alloy is characterized by a singularity drop of the Curie temperature T_c, which becomes of the order of room temperature. It increases in a near-linear fashion in the range 30 - 35 wt% Ni, a property that is sometimes exploited in magnetic shunt devices. At 36 wt% Ni concentration T_c has already reached the value of 230 °C and the thermal expansion coefficient is extremely low (~$1 \cdot 10^{-6}$ K^{-1}, the so called *Invar behavior*). The Invar property descends from the fact that the spontaneous *volume magnetostriction* compensates, on approaching the Curie temperature, for the variation of the lattice parameter. The resistivity is pretty high ($75 \cdot 10^{-8}$ Ω·m), a feature conducive to low losses at high frequencies and making the $Fe_{64}Ni_{36}$ tapes interesting for applications like radar pulse transformers. The $Fe_{50}Ni_{50}$ alloys are characterized by a high saturation polarization J_s = 1.6 T. They can be prepared as strongly (100)[001] textured sheets by means of severe cold rolling to the final thickness (> 95%) and primary re-crystallization annealing around 1000 °C. The favorable directional feature provided by the texture can be reinforced by the anisotropy K_u induced through longitudinal magnetic annealing at a temperature $T \sim$ 450°C (Curie temperature $T_c \sim$ 500 °C) and slow cooling. In this way a squared hysteresis loop is achieved, to be exploited, for example, in magnetic amplifiers and saturable reactor cores. By increasing the Ni content towards 55 - 60 wt %, the induced anisotropy K_u, of the order of 300 - 400 J/m^3, is not far from the value of the magnetocrystalline anisotropy K_1. By annealing under a transverse saturating field, one can therefore achieve a sheared low-remanence hysteresis loop characterized by a large unipolar swing (0.9 – 1.2 T). This feature is welcomed in devices like unipolar pulse transformers and ground fault interrupters.

The highest permeabilities and lowest coercivities are obtained around 75 – 80 wt% Ni concentration, because it is possible to approach vanishing values for both magnetostriction and anisotropy. Fig.40 actually shows that it is not possible to simultaneously achieve zero values for K_1, λ_{100} and λ_{111}. It is therefore expedient to make calibrated additions of elements like Mo, Cu and Cr, by which one can achieve, at the same time, an isotropic magnetostriction constant $\lambda_s \sim 0$ and good control of the Fe_3Ni phase ordering through annealing and cooling. Since the anisotropy constant K_1 depends on ordering, it is possible to devise a thermal treatment leading to $K_1 \sim 0$ [126]. A further advantage introduced by the additives is a substantial increase of resistivity (e.g. from $20 \cdot 10^{-8}$ Ω·m to $62 \cdot 10^{-8}$ Ω·m by introducing 5 wt% Mo in 78 wt% Ni alloys), at the cost of a certain reduction of J_s. As reported in Table 15, a coercive field lower than 1 A/m and relative initial permeabilities higher that 10^5 can be obtained in these alloys, generally known under the trade name of permalloy or mumetall. A typical DC hysteresis loop in a permalloy tape is given in Fig. 41, illustrating, through comparison with the loop of a GO Fe-Si sheet, an example of achievable magnetic softness. By field annealing at temperatures ranging between 250 °C and 380 °C, a substantial manipulation of the hysteresis loop can be obtained, because the intrinsically low magnetocrystalline anisotropy (lower than about 100 J/m^3) can be overcome by the anisotropy K_u induced by magnetic ordering. On passing then from longitudinal to transverse field annealing, the hysteresis loop shape may evolve towards quasi-linear behavior. This corresponds to increased role of the rotations in the magnetization process and decreased losses. It should be remarked that the magnetocrystalline anisotropy K_1 increases with decreasing the temperature. Consequently, the heat treatments should be calibrated for the temperature at which the magnetic core is eventually employed. In particular, in permalloys for cryogenic applications, the annealing temperature is conveniently reduced. In the example shown in Fig. 55, regarding the alloy $Fe_{17.9}Ni_{78.3}Mo_{3.8}$, it is observed that while annealing at T_a = 535 °C and quenching to room temperature leads to $K_1 \sim 0$ at T = 23 °C, vanishing anisotropy at T = -195 °C is obtained by decreasing the annealing temperature to T_a = 495 °C [127].

Co-Fe alloys

Cobalt-iron alloys do not display outstanding soft magnetic properties, but they represent a unique solution in terms of Curie temperature and saturation polarization, both remarkably higher than in pure Fe [126]. In the classical $Fe_{50}Co_{50}$ alloy we have, for instance, T_c = 950 °C and J_s = 2.35 T. This reveals useful for a number of applications where volume reduction and high working temperature may be required, as occurring in onboard high-speed generators for aircrafts and spacecrafts, without concern for the cost of Co.

The $Fe_{50}Co_{50}$ alloy transforms from fcc (γ) to bcc (α) solid solution on cooling passing through T = 1000 °C and undergoes rapid long range ordering below 730 °C. The $\gamma \rightarrow \alpha$ transformation can limit to some extent the re-crystallization process, while ordering detrimentally affects the mechanical properties, leading to a brittle material. Ordering can be retarded by the addition of 2 wt% V and rapid quenching. Vanadium appears

also to favour the formation of a mixture of α-phase and martensite upon quenching, conducive to ductile behaviour of the material. The $Fe_{49}Co_{49}V_2$ alloys can be prepared as thin sheets by cold rolling, with the V introducing the further benefit of a large increase of resistivity ($\rho = 40 \cdot 10^{-8}$ Ω·m vs. $\rho = 7 \cdot 10^{-8}$ Ω·m in $Fe_{50}Co_{50}$). By adjusting the cooling rate one can also dramatically decrease the anisotropy constant. However, the magnetostriction remains extremely high, with $\lambda_{100} \sim 150 \cdot 10^{-6}$ and $\lambda_{111} \sim 30 \cdot 10^{-6}$, which hinders the achievement of very soft magnetic behavior.

The value of the coercive field in regular $Fe_{49}Co_{49}V_2$ alloys (Permendur) is around 30 - 80 A/m. A substantial property improvement can be obtained by careful control of the material purity and magnetic field annealing. The high purity alloy can exhibit $H_c \sim 20$ A/m and maximum relative permeability $\mu_r \sim 2 \cdot 10^4$. It displays lower losses and requires far lower exciting power than best quality NO Fe-(3 wt%)Si sheets beyond about $J_p = 1.5$ T. It is therefore the material of choice for generators and motors with high rotation speed and special transformers with low losses at very high inductions. Their excellent frequency response is illustrated in Fig. 56, providing a comparison of the energy loss versus frequency behaviours of 0.20 mm thick non-oriented Fe-Si and $Fe_{49}Co_{49}V_2$ sheets.

Further properties and features of Ni-Fe and Co-Fe alloys

1) *Temperature dependence of the magnetic properties.*

The vanishing of the anisotropy energy around 80% Ni concentration can be adjusted by suitable thermal treatments, according to the K_1 behaviors reported in Fig. 42, in order to attain an extremely high value of the permeability μ_r around a convenient temperature, which approximately corresponds to the temperature at which K_1 crosses the zero line. One can move, in particular, the temperature at which μ_r is maximum downward by lowering the annealing temperature and/or the cooling rate. It is shown in Fig. 42 that annealing at 495 °C leads to $K_1 \sim 0$ at cryogenic temperatures in the $Fe_{17.9}Ni_{78.3}Mo_{3.8}$ alloy .

Fe-Co alloys, with their high Curie temperature ($T_c = 930$ °C in $Fe_{49}Co_{49}V_2$), are attractive for the temperature stability of their properties. It is verified that on going from room temperature to 180 °C the Permendur alloys exhibit a moderate improvement of their magnetic behavior, with a slight increase of permeability and decrease of power losses (around 10 %). It is generally verified that the properties do not greatly deteriorate up to about to 500 °C, which makes Fe-Co alloys very attractive for high-temperature applications.

2) *Stress dependence of the magnetic properties.*

The strong variation of the magnetostriction constants with the relative proportions of Fe and Ni makes the stress-sensitivity of the Fe-Ni alloys changing from strong to negligible on going from the Invar composition ($Fe_{64}Ni_{36}$) to the permalloy composition. The $Fe_{32}Ni_{68}$ alloy combines low K_1 value with relatively high and positive magnetostriction and the hysteresis loop shape can be sharply squared applying a tensile stress. Although nearly zero magnetostrictive, permalloy and mumetall can suffer deterioration of their soft magnetic behavior from the machining operations (forming, bending, deep drawing, shearing, cutting, etc.) required for various kinds of applications (core assemblage, magnetic shields, etc) . The residual stresses are relaxed by annealing at a temperature of 850 °C – 900 °C, followed by rapid cooling through the ordering region (from 600 °C to 300 °C). If machining is made on the cold-rolled sheets, a recrystallization treatment must be performed, by heating a few hours at a temperature of 1050 °C – 1150 °C.

Fe-Co alloys exhibit strong magnetostriction ($\lambda_s = 60 \cdot 10^{-6}$) and need stress relaxation annealing of the final product. Since atomic re-ordering ($\gamma \rightarrow \alpha$ transformation**)** would degrade the soft magnetic properties, annealing must be performed below 900 °C. This is followed by relatively fast cooling (about 250 °C/hour) till 300 °C.

3) *Mechanical properties*.

Fe-Ni alloys are moderately soft from the mechanical viewpoint (Vickers hardness ranging between 120 and 160) and do not pose special problems in the standard machining operations. The classical $Fe_{50}Co_{50}$ alloys are very brittle and are not used in practice, because one can rely on the ductile $Fe_{49}Co_{49}V_2$ alloys, whose Vickers hardness is around 200.

4) *Coating.*

Fe-Ni and Fe-Co laminations are delivered uncoated. If required, they are slightly oxidized by making the final part of the heat treatment in air.

5) *Delivery.*

Fe-Ni alloys are generally delivered as: i) flat products; ii) final heat-treated tapewound or ring-stacked cores; 3) massive products (bars, billets, hot-rolled sheets). The strips can be purchased either in the cold-rolled or annealed condition, with thicknesses ranging between 25 μm and 3 mm and variable width (300 mm – 600 mm).

Fe-Co alloys are commercially available as strips of thickness 0.1 mm - 1.5 mm, rods of diameter 10 mm - 80 mm, and ring cores. Strips and rods are usually delivered in the cold-worked state and need a final heat treatment, according to the previously mentioned procedure. Besides the permendur alloy $Fe_{49}Co_{49}V_2$, the industrial offer includes the composition $Fe_{83}Co_{17}$, having saturation polarization J_s = 2.22 T, magnetostriction reduced to $\lambda_s = 25 \cdot 10^{-6}$, and good mechanical properties.

Fig. 58 compares the initial magnetization curves of mumetal ($Ni_{80}Fe_{15}Mo_5$) and $Fe_{49}Co_{49}V_2$ alloys with those of the Finemet nanocrystalline alloy and of standard non-oriented Fe-(3 wt%)Si steel sheets.

6) *Specifications.*

The specifications for the Fe-Co alloys are defined in the Standards IEC 60404-8-6 [37].

7) *Applications*.

Fe-Ni alloys are applied in a large number of devices where high-performance magnetic cores are required. The applications include measuring instruments, switch-mode power supplies, ground fault interrupters, magnetic sensors, recording heads for magnetic tape systems, inductors for applications up to the MHz range. A major application of mumetal is magnetic shielding. The Invar alloy ($Fe_{64}Ni_{36}$) has Curie temperature around 230 °C and nearly zero thermal expansion coefficient ($\sim 1 \cdot 10^{-6}$) between 20 °C and 100 °C. This property results from a compensating effect, where the expansion of the lattice with the increase of the temperature is countered by a corresponding decrease of the volume magnetostriction engendered by a relatively fast decrease of the saturation magnetization [128].

The Fe-Co alloys are typically applied in motors, generators, and transformers when a high power-to-weight ratio is required (e.g. in airborne and spaceborne devices). Bulk Fe-Co polar pieces are also indispensable for high-performance electromagnets.

We conclude our review of the metallic soft magnetic alloys by a comparison of the their power loss behaviors. Following Eq. (8), we decompose the magnetic power loss $P(f) = f \cdot W(f)$ as $P(f) = P_{\mathrm{h}}(f) + P_{\mathrm{cl}}(f) + P_{\mathrm{exc}}(f)$, the sum of hysteresis $P_h(f) = f\, W_h$, classical $P_{cl}(f) = f\, W_{cl}(f)$, and excess $P_{exc}(f) = f\, W_{exc}(f)$ power loss components. We then show in Fig. 45 a summary of the $P(f)$ response of crystalline and amorphous alloys at power and medium frequencies, where the different contributions by P_h, P_{cl}, and P_{exc} are highlighted. These results can be explained in terms of the previously discussed intrinsic and structure dependent properties of the materials.

SOFT FERRITES

Ferrimagnetic interaction and intrinsic properties of ferrites.

Soft spinel ferrites are largely applied at frequencies above the audio range, up to few hundred MHz, because of their non-metallic character. They have the general composition $MO \cdot Fe_2O_3$, where M is a divalent metal ion such as Fe^{2+}, Mn^{2+}, Ni^{2+}, Zn^{2+}, Mg^{2+}. Typical applications include pulse and wide-band transformers for television and telecommunications, inductor cores in switched-mode power supplies, antenna rods, cores for electromagnetic interference suppression, magnetic heads.

For frequencies in the range 500 MHz – 100 GHz the so-called microwave ferrites are employed. Some types of spinel ferrites, hexagonal ferrites (like $BaFe_{12}O_{19}$) and garnets (like $Y_3Fe_5O_{12}$) belong to this class of materials. They are used in a variety of devices, such as waveguide isolators, gyrators, and modulators, to control the transmission or absorption of electromagnetic waves.

The magnetic properties of ferrites are due to the magnetic moments of the metal ions. The ion-ion interaction is antiferromagnetic in nature and leads to a distinctive temperature dependence of the inverse of susceptibility and of the saturation polarization [129]. As illustrated in Fig. 46, the oxygen ions in spinel ferrites are arranged in a close-packed face-centered cubic structure and the small metal ions slip into interstitial positions, either at tetrahedral (A) or octahedral (B) sites, which are surrounded by four and six oxygen ions, respectively. In a unit cell, which contains eight formula units (i.e. 32 O^{2-} ions, 16 Fe^{3+} ions, and 8 M^{2+} ions), 8 of the available A sites and 16 of the available B sites are occupied by the metal ions. When the M^{2+} ions and the Fe^{3+} ions are in the A and B sites, respectively, we have the so-called *normal spinel* structure. The *inverse spinel* structure is obtained when the 16 Fe^{3+} ions are equally subdivided between the A and B sites, the latter being shared with the M^{2+} ions. Intermediate cases are very frequent.

The spontaneous magnetization of ferrites and its temperature dependence were explained by Néel [130], by assuming that the spin moments of the metal ions in the A and B sublattices are antiferromagnetically coupled through indirect exchange interaction. Given the insulating character of these materials, one can talk of bound electrons. Since the cations are separated by the oxygen anions, direct exchange interaction between their *3d* electron spins is negligible and an indirect coupling mechanism, the superexchange [131], is expected

to take place. This involves the spins of the two extra *2p* electrons in the O^{2-} ion, which interact by direct exchange with the *3d* spins of the two neighbouring metal cations. Interaction implies that the *3d* and *2p* orbitals exchange electrons, with the constraints imposed by Hund's rule on the spin direction in the *3d* orbitals. Since the *2p* spins in the O^{2-} ion are, because of the Pauli exclusion principle, oppositely directed, it turns out that if the two cations have both five or more *3d* electrons (half-full or more than half-full *3d* shell), *their total magnetic moments are bound to antiparallel directions*. This is the case of the common ferrite ions Mn^{2+}, Fe^{2+}, Co^{2+}, Ni^{2+}. The strength of the superexchange interaction is the greatest when a straight line connects the cations through the O^{2+} ion. The A-B coupling, which is associated to an A-O-B angle around 125°, is then much stronger than the A-A and B-B couplings, where the angles are 90° and 80°, respectively. At the end, one is left with a system made of two coupled arrays of anti-parallel magnetic moments of unequal magnitude, which results in a net magnetic moment. This uncompensated antiferromagnetic behavior is called *ferrimagnetism* and the resulting magnetic moment per unit cell can be calculated through Néel's hypothesis. These calculations are in good agreement with the experimental values of the saturation magnetization and are supported by neutron diffraction experiments.

Although the magnetic moment per formula unit may be very large in terms of number of Bohr magnetons, the saturation polarization J_s of spinel ferrites is low (typically below 0.5 T at room temperature), because of the low density of the uncompensated magnetic ions. In addition, the temperature dependence of J_s, resulting from the composition of the temperature variations of the magnetization of the individual sublattices, may give rise, according to Néel's theory, to a variety of behaviors [129]. Most magnetic spinel ferrites, like $FeFe_2O_4$, $NiFe_2O_4$, $CoFe_2O_4$, are of the inverse type. In this case, the magnetic moment per formula unit equals that of the M^{2+} ion, because the Fe^{3+} ions are evenly distributed among the A and B sublattices. Table 16 provides some examples of ion and moment distribution among sites in different types of spinel ferrites. The $ZnFe_2O_4$ ferrite is of the normal type, but, since the Zn^{2+} ion has a closed 3*d* shell and zero magnetic moment, it is paramagnetic at room temperature. In the absence of A-B type coupling, an antiferromagnetic B-B coupling is expected, as shown in Table 16, but this is very weak and antiferromagnetism in $ZnFe_2O_4$ is observed only below 9 K. $MnFe_2O_4$ is an example of partly normal and partly inverse spinel structure, where the Mn^{2+} and Fe^{3+} share in certain proportions the A and B sites. The general properties of a number of normal and inverse spinel ferrites are shown Table 17. The differences observed between predicted and measured magnetic moments per formula unit n_B (Bohr magnetons) are ascribed to a number of factors, like imperfect quenching of the orbital magnetic moments, changes in the ion valence, and fluctuations in the cation distribution between the A and B sites. Such differences are small, in general, except for $CoFe_2O_4$, where the orbital contribution is important.

Ferrites, being ionic compounds, are insulators in principle and display in practice a wide range of resistivity values, always orders of magnitude higher than typical Fe-Si or amorphous alloys. The most important conduction mechanism is the transfer of electrons between Fe^{2+} and Fe^{3+} ions in the octahedral sites. Magnetite ($FeFe_2O_4$) therefore exhibits a nearly metallic behavior, with resistivity $\rho \sim 10^{-5}$ Ω·m.

Most technical spinel ferrites are of the mixed type, where the presence of two or more metal ions M^{2+} introduced in non-stoichiometric proportions can provide great versatility of the magnetic properties. Mn-Zn and Ni-Zn ferrites are the two basic families of mixed soft ferrites, where, by tuning the relative concentrations of the metal ions and making suitable additions and thermal treatments, material tailoring to specific applications can be achieved. Although, as previously stressed, normal $ZnFe_2O_4$ has zero magnetic moment, its addition to the inverse $MnFe_2O_4$ or $NiFe_2O_4$ ferrites leads to an increase of the global saturation magnetization at 0 K. This can be understood, in terms of Néel's theory, as due to the parallel alignment of the magnetic moments of the Fe^{3+} ions in the B-sites of $ZnFe_2O_4$, which is enforced by the antiferromagnetic coupling with the ion moments in the A sites, as illustrated in Table 16. The price one has to pay for mixing is progressive weakening of the A-B coupling with increase of the proportion of $ZnFe_2O_4$, leading to a decrease of the ferrimagnetic Curie temperature [132]. The simple spinel ferrites, which have cubic symmetry, generally have negative anisotropy constant K_1 (<111> easy axis). This derives, according to the single ion model, from the sum of the opposite contributions of the Fe^{3+} ion moments occupying the A and B sites, respectively, where the negative K_{1B} term eventually prevails over the positive term K_{1A}. It occurs because the orbital angular moment in the octahedral sites is not fully quenched by the crystal field. In $CoFe_2O_4$, however, K_1 is large and positive (<100> easy axis), because the large spin-orbit coupling of the Co^{2+} ions predominates (Table 17). By acting on the starting composition and the processing method, mixed Mn-Zn and Ni-Zn ferrites can be prepared with very low anisotropy values in a range of temperatures suitable for applications (20 °C – 100 °C). It has been shown that Zn substitution in Mn and Ni ferrites leads to weakening of the exchange field acting on the octahedral (B) Fe ions and, consequently, to weakening of the negative K_{1B} constant on approaching the room temperature. If, in addition, calibrated replacement of divalent cations with Fe^{2+} or Co^{2+} ions is made, one can combine their positive anisotropy with the negative K_1 value of the host in such a way that the resultant anisotropy constant K_1 will cross the zero value around a convenient temperature (e.g. between room

temperature and 100 °C). Full anisotropy compensation is, for example, obtained at 300 K with the composition $Mn_{.53}Zn_{.40}Fe_{.07}^{2+}Fe_2^{3+}O_4$ [133]. As previously remarked, a small anisotropy value straightforwardly leads to soft magnetic behavior. It can be stated in fact, under very general terms, that the coercivity and the initial permeability approximately follow the relationships

$$H_c \propto \frac{K^{1/2}}{J_s < s >}, \qquad \mu_i^{rot} \propto \frac{J_s^2}{K}, \qquad \mu_i^{dw} \propto \frac{J_s^2 \cdot < s >}{K^{1/2}} \qquad (11),$$

where μ_i^{rot} and μ_i^{dw} are the contributions to the initial permeability deriving from coherent rotation of the magnetization and domain wall (d.w.) displacements, respectively, and $<s>$ is the average grain size [134][135]. Besides the crystalline structure, applied and residual stresses and magnetic ordering induced by field annealing may contribute to the magnetic anisotropy. The effect of these various terms is summarized by the constant K in Eq. (11).

Preparation method

Industrial materials are prepared in such a way as to achieve near-zero value of K_1 around the expected operating temperature, which in most cases is around 100 °C. The accurate control of their intrinsic and structural properties (e.g. ion valence, purity of the raw material, stoichiometry, dopants, grain size, porosity) during preparation is accomplished through the well-established routes of powder metallurgy [136][137]. The conventional production process starts with the preparation of the base oxides, typically by calcination of suitable iron salts, and their mixing by prolonged wet grinding. This leads to a homogeneously fine powder, where the dimension of the single granules is around or less than one micrometer. The resulting mixture is then dried and pre-fired in air at 900°C – 1200 °C. During this stage the spinel ferrite is formed by solid state reaction of Fe_2O_3 with the other present metal oxides (MO or M_2O_3). The so-prepared powders are then compacted, either by die-punching or hydrostatic pressing, and pieces of the desired shape are obtained. The filling factor of the so-obtained assembly of particles is around 50% - 60%. In the final main step, the pieces are brought to a temperature of 1200 °C – 1400 °C in an oxidizing atmosphere, with or without application of external pressure. The desired final magnetic and structural properties of the material are thus achieved through: i) particle bonding by interdiffusion and grain growth; ii) densification, by elimination of the interparticle voids, up to ~ 95 % - 98% filling factor; iii) chemical homogenization, by completion of unfinished reactions. The resulting product is hard and brittle and, if required, it is eventually machined with precision abrasive tools, in order to meet the final tolerances. The final particle assembly is made of semiconducting grains, their typical size ranging between 10 μm and 50 μm, separated by a few nm thick insulating layer (see the inset in Fig. 46).

Magnetization process and losses.

The DC resistivity of typical Mn-Zn ferrites can vary from some 10^{-2} Ω·m to ~10 Ω·m, depending on the amount of doping with Fe^{2+}, while in Ni-Zn ferrites can reach values as high as $10^5 – 10^6$ Ω·m, because there is little difference between the resistivity of the grain and that of the boundary layer. It turns out that on increasing the magnetizing frequency a strong capacitive effect can take place in Mn-Zn ferrites, engendering a drop of the material resistivity. This is shown for three different types of commercial products in Fig. 46. The eddy current paths, tightly bound to the grain interior at low frequencies, may thus invest the whole sample cross-section at high frequencies [138]. They can give rise, however, to an appreciable contribution to the energy losses only on relatively wide cross-sectional area samples and at high frequencies [139]. The calculation of the eddy current losses is made difficult by the heterogeneous structure of the material and can be worked out by recurring to a specific multiscale modelling of the eddy current patterns, to be numerically implemented [139]. No eddy current effects are expected till the GHz range in Ni-Zn ferrites.

The value of permeability and coercivity of soft ferrites are controlled to a good extent by the addition of Fe^{2+} ions (mainly in the Mn-Zn ferrites) or Co^{2+} ions (mainly in the Ni-Zn ferrite), by which the anisotropy energy, that is the value of the anisotropy constant K, can be controlled. It turns out that higher permeabilities and lower coercivities are found in the Mn-Zn compounds, as illustrated by the behaviour of the DC hysteresis loops shown in Fig. 47. A certain range of behaviours is achieved, for a given type of ferrite (i.e. either Mn-Zn or Ni-Zn), by finely acting on the composition, the additives, and the final material structure (grain size, porosity, etc.).

The near-insulating character of ferrites is conducive to a nearly constant value of the initial susceptibility over many frequency decades, typically from DC up to some 100 kHz and 1 MHz in Mn-Zn and Ni-Zn ferrites, respectively. Fig. 48 shows the frequency dependence of the real and imaginary parts of the relative initial permeability $\mu = \mu' - i\mu''$ in selected industrial products. It is observed how the relaxation of $\mu'(f)$

is preceded by a hump and followed by a transition to negative values, the landmark clue to ferromagnetic resonance. The overall behaviour of $\mu'(f)$ and $\mu''(f)$ can be chiefly interpreted, once the rotational and domain wall contributions are singled out, in terms of distributed (grain-to-grain) effective anisotropy fields, engendering distributed resonant absorption frequencies [140][141].

In the low induction regimes and at sufficiently high frequencies (quasi-linear response) the dissipation of energy can be related to the phase shift δ between $B(t)$ and $H(t)$ according to Eq. (3), $W = \pi H_p B_p \cdot \sin\delta$, where W is the specific energy loss per cycle and unit volume. H_p and B_p are the peak amplitudes of the field and induction waveforms and, according to Eq. (4), $\delta = \tan^{-1}(\mu''/\mu')$. Damping effects by eddy currents in Mn-Zn ferrites, where anisotropy compensation may critically depend on the addition of conduction prone Fe^{2+} ions, do play a role as a source of energy loss in the range of frequencies of interest in applications only in relatively large samples [139] and are irrelevant in Ni-Zn ferrites. Spin damping mechanisms, involving either direct or indirect relaxation to the lattice, are therefore invoked to justify the basic phenomenology of losses [142]. In any case, whatever the predominant magnetization mechanism, either coherent magnetization rotation or d.w. displacements, high susceptibility and high limiting frequency of operation are conflicting requirements (Snoek's rule, see Fig. 48). By denoting with f_0 the relaxation frequency (cutoff frequency of $\mu'(f)$), it can be assumed, in particular, that the relationships $f_0 \chi_i^{rot} \propto J_s$ for spin rotations and $f_0 \chi_i^{dw} \propto J_s^2 / < s >$ for d.w. processes approximately hold. This suggests that the dispersion of susceptibility is shifted towards higher frequencies in small-grained ferrites.

Further properties and features of soft ferrites.

1) *Temperature dependence of the magnetic properties.*

It was previously stated how the soft ferrite chemistry aims at best magnetic performances in a temperature range useful for applications. This means, from the physical viewpoint, focusing on the behavior of the anisotropy constant K and the saturation magnetization J_s versus temperature. K is driven towards zero value in appropriate fashion exploiting the combination of the positive K_{1A} and negative K_{1B} terms, while J_s falls on approaching the Curie temperature according to a composition dependent behavior. One is eventually able to achieve a certain stability of the magnetic response upon a certain temperature interval, which can typically range between 50 °C and 150 °C, as put in evidence by the dependence of the initial permeability on temperature shown for different compounds in Fig. 49. One can observe a more or less pronounced double-peak structure in these behaviors. The first peak occurs in association with the zero crossing of the anisotropy energy. The second peak, common to the majority of ferromagnetic materials (Hopkinson's peak), is due to the complete vanishing of K, which occurs before J_s falls to zero at the Curie temperature. The same anisotropy mechanism leading to optimal permeability behavior in Fig. 49 leads, at least in the low-to-medium frequency range (up to a few hundred kHz), to minimum loss figure [143].

2) *Effect of stresses and mechanical properties*.

Soft ferrites have negative magnetostriction, which is higher in Ni-Zn compounds, and is typically around a few 10^{-6}. Their magnetic properties are therefore stress sensitive. In practice, stresses can arise with core embedding (e.g. by plastic encasing) and may cause a decrease of permeability.

Being ceramic materials, ferrite cores are brittle and sensitive to any shock and fast changing load. For example, high cooling rates and high static or cyclic loads can cause cracks or failure of the cores. Machining of sintered ferrites is often required for meeting final tolerances of the components. It should be accomplished by grinding with abrasive (typically diamond) tools.

3) *Applications*.

The major feature of the soft ferrite magnets, one of exhibiting high permeability and low magnetic losses from DC to radiofrequencies, is exploited in a great variety of applications. These may find a limitation in the low value of the saturation magnetization, common to all ferrite types, and, in some instances, also in the low value of the Curie temperature. They are favored in many instances by low cost compared to more performing but costlier materials (e.g. amorphous and nanocrystalline cores).

The highly insulating rare-earth ferrites of garnet structure (e.g., $Y_3Fe_5O_{12}$) are characterized by the narrowest resonance linewidth ($\Delta H \approx 10$ A/m at 10 GHz in single crystals), that is, the smallest losses. They are the material of choice for microwave applications [144][145]. Examples of such applications are non-reciprocal devices, like isolators and circulators, exploiting the different response of a saturated ferrite to the sense of rotation of a circularly polarized wave. A linearly polarized electromagnetic wave can actually be considered as composed of two counter-rotating circularly polarized waves and only one of them can resonate with the precessing spins at the Larmor frequency, depending on the direction of the saturating bias field.

Resonant isolators let then a circularly polarized wave at the resonance frequency to pass in one direction, but they will prevent the reflected portion of it to travel back to the source thanks to the resonant absorption by the precessing spins.

Further significant applications of ferrite cores include: a) high-Q inductors in resonant circuits and filters; b) current transformers; c) broadband transformers (antenna transformers, ISDN transformers, etc.); d) electromagnetic interference (EMI) sensors; e) medium and high frequency switch-mode power supplies. The wide range of commercially available cores are usually optimized for specific frequency and temperature ranges.

CONCLUDING REMARKS

Soft magnetic materials are key elements in all instances of generation, transmission, and conversion of the electrical energy. As such, they have great technological and social value, far beyond their mere economic significance. At present time, the soft magnets used in applications are fully fledged materials, where progress in their properties and applications maintains an evolutionary character. The amorphous and the nanocrystalline alloys have been the real breakthrough materials appearing in the last 20 – 30 years. Much research has been done since, looking for novel compositions with improved properties and for more effective treatments, widening their versatility and energetic efficiency. Applications have indeed outpaced in many cases the full understanding of the magnetic properties. Consequently, empirical attitudes in responding to technological needs sometimes prevail. Modeling of magnetization process, hysteresis, and losses is, for example, still the subject of many investigations and a wide-ranging assessment of the associated complex phenomenology is not fully attained at present time.

In this review we have summarized the preparation methods and the basic properties of the soft magnetic materials having special relevance for energy applications. A physical framework for the interpretation of such properties has been discussed. It is stressed how the soft magnetic behavior of the materials results from the combined influence of intrinsic and structural parameters and how the magnetic optimization must be pursued also against a number of other properties, like the electrical and mechanical ones, besides the ecomomic issues. Present industrial trends favor the use of devices operating at ever increasing frequencies, like high-speed rotating machines and switch-mode power supplies. These call for increasingly efficient magnetic cores upon a broad range of frequencies and optimal combination of material type, costs, and loss predicting methods.

References

[1] W.F. Barrett, W. Brown, and R.A. Hadfield, Electrical conductivity and magnetic permeability of various alloys of Fe, *Sci. Trans. Roy. Dublin Soc.,* **7:** 67-126, 1900.

[2] N.P. Goss, *Electrical sheet and method and apparatus for its manufacture and test*, U.S. Patent No. 1,965,559, 1933.

[3] G.W. Elmen, *Magnetic material*, Canadian Patent No. 180,359, 1916.

[4] J.L. Snoek, *Magnetic material and core*, U.S. Patent No. 2,452,531, 1948.

[5] P.W. Duwez and S.C.H. Lin, Amorphous ferromagnetic phase in iron-carbon-phosphorous alloys, *J. Appl. Phys.*, **38 :** 4096-4097**,** 1967.

[6] B. Heinrich and J.A.C. Bland (eds.), *Ultrathin Magnetic Structures*, Berlin: Springer-Verlag, 1994.

[7] B. Dieny, Couches minces et multicouches magnétiques, in E. du Trémolet de Lacheisserie (ed.), *Magnétisme*, Vol. 2, Grenoble: Presses Universitaires de Grenoble, 1999, pp. 255-300.

[8] A. Barthélémy, A. Fert, and F. Petroff, Giant magnetoresistance in magnetic multilayers, in K.H.J. Buschow (ed.), *Handbook of Magnetic Materials*, Vol. 12, Amsterdam: Elsevier, 1999. pp. 1-96.

[9] G. Bertotti, *Hysteresis in Magnetism*, San Diego: Academic Press, 1998.

[10] S. Flohrer, R. Schäfer, J. McCord, S. Roth, L. Schultz, F. Fiorillo, W. Günther, G. Herzer, Dynamic magnetization process of nanocrystalline tapewound cores with transverse field-induced anisotropy, *Acta Mater.* **54**: 4693-4698, 2006.

[11] L. Néel, Bases d'une nouvelle théorie génerale du champ coercitif, *Ann. Univ. Grenoble,* **22**: 299-319, 1946.

[12] L.J. Dijkstra and C. Wert, Effect of inclusions on coercive force of iron, *Phys. Rev* **79**: 979-985, 1950.

[13] H.R. Hilzinger and H. Kronmüller, Statistical theory of the pinning of Bloch walls by randomly distributed defects, *J. Magn. Magn. Mater.* **2**: 11-17, 1976.

[14] A. Ferro and F. Fiorillo, Grain size dependence of the coercive force in very pure iron, *Proc. Soft Magn. Mater. Conf.* 7, The University College, Cardiff, 1985, pp. 75-77.

[15] J. Degauque, B. Astié, J.L. Porteseil, and R. Vergne, Influence of the grain size on the magnetic and magnetomechanical properties of high-purity iron, *J. Magn. Magn. Mater.* **26**: 261-263 (1982).

[16] G. Herzer, Nanocrystalline soft magnetic alloys, in K.H.J. Buschow (ed.), *Handbook of Magnetic Materials*, Vol. 10, Amsterdam: Elsevier, 1997, pp. 415-463.

[17] R. Alben, J.J. Becker, and M.C. Chi, Random anisotropy in amorphous ferromagnets, *J. Appl. Phys.*, **49**: 1653-1658,1978.

[18] H. Kronmüller and W. Fernengel, The role of internal stresses in amorphous ferromagnetic alloys, *Phys. Stat. Sol. (a)*, **64**: 493-602,1981.

[19] C. Appino and F. Fiorillo, A model for the reversible magnetization in amorphous alloys, *J. Appl. Phys.*, **76**: 5371-5379, 1994.

[20] C. Appino, F. Fiorillo, and A.Maraner, Initial susceptibility vs. applied stress in amorphous alloys with positive and negative magnetostriction, *IEEE Trans.Magn.*, **29**: 3469-3471, 1993.

[21] H. Morita, Y. Obi, and H. Fujimori, Magnetic anisotropy of $(Fe, Co, Ni)_{78}Si_{10}B_{12}$ alloy system, in S. Steeb and R. Warlimont (eds.), *Rapidly Quenched Metals*, Amsterdam: North-Holland,1985, pp. 1283-1286**.**

[22] H. J. Williams, W. Shockley, and C. Kittel, Studies on the propagation velocity of a ferromagnetic domain boundary, *Phys. Rev.*, **80**: 1090-1094, 1950.

[23] R.H. Pry and C.P. Bean, Calculation of energy losses in magnetic sheet material using a domain model, *J. Appl. Phys.*, **29**: 532-533, 1958.

[24] G. Bertotti, Physical interpretation of eddy current losses in ferromagnetic materials, *J. Appl. Phys.*, **57**: 2110-2126, 1985.

[25] G. Bertotti, General properties of power losses in soft ferromagnetic materials, *IEEE Trans. Magn.* **24**: 621-30, 1988.

[26] E. Barbisio, F. Fiorillo, and C. Ragusa, Predicting loss in magnetic steels under arbitrary induction waveform and with minor hysteresis loops, *IEEE Trans. Magn.* **40**: 1810-1819, 2004.

[27] S. E. Zirka, Y. I. Moroz, P. Marketos, and A. J. Moses, Viscosity-based magnetodynamic model of soft magnetic materials, *IEEE Trans. Magn.* **42**: 2121-2132, 2006.

[28] S. E. Zirka, Y. I. Moroz, S. Steentjes, K. Hameyer, K. Chwastek, and S. Zurek, Dynamic magnetization models for soft ferromagnetic materials with coarse and fine domain structures, *J. Magn. Magn. Mater.,* **394**: 229-236, 2015.

[29] I. Mayergoyz and C. Serpico, Nonlinear diffusion of electromagnetic fields and excess eddy current losses, *J. Appl. Phys.,* **85**: 4910-4912, 1999.

[30] A. Ferro and G.P. Soardo, Sur les effets de la polygonisation dus aux changements de phase sur les propriétés magnétiques du fer de très haute perméabilité, *Mémoires Sci. Rev. Metall.* **65**: 161-166, 1968.

[31] M. Zucca, G. Lorusso, F. Fiorillo, P.E. Roccato, and M. Annibale, Highly efficient shielding of high-voltage underground power lines by pure iron screens, *J. Magn.Magn. Mater.*, **320**: e1065-e1069, 2008.

[32] IEC Standard Publication 60404-8-3, Specifications for individual materials – Cold-rolled electrical non-alloyed steel sheet and strip delivered in the semi-processed state, IEC Central Office, Geneva, 2005.

[33] K. Ueno, I. Tachino, and T. Kubota, Advantages of vacuum degassing of non-oriented electrical steels, in R. Pradham (ed.), *Metallurgy of vacuum degassed steel products*, The Mineral, Metals and Materials Society, 1990, pp. 347-350.

[34] G. Lyudkovsky and P.K. Rastogi, Effects of boron and zirconium on microstructure and magnetic properties of batch annealed Al-killed low carbon steels, *IEEE Trans. Magn.* **21**: 1912-1914, 1985.

[35] A. Coombs, Improved low loss high permeability grades, processing and properties, *J. Phys. IV (France)* **8-Pr2**: 475-482, 1998.

[36] M. Küpferling, C. Appino, V. Basso, G. Bertotti, F. Fiorillo, and P. Meilland, Magnetic hysteresis in plastically deformed low carbon steel laminations, *J. Magn.Magn. Mater.* **316:** e854-e857, 2007.

[37] IEC Standard Publication 60404-8-6, Specifications for individual materials - Soft magnetic metallic materials, IEC Central Office, Geneva, 1999.

[38] B. Viala, J. Degauque, M. Baricco, E. Ferrara, M. Pasquale and F. Fiorillo: "Magnetic and mechanical properties of FeSi 6.5 wt % rapidly solidified alloys and their interpretation", *J. Magn. Magn. Mater.*, **160**: 315 – 317, 1996.

[39] G. Bertotti and F. Fiorillo, Crystalline Fe-Si, Fe-Al, and Fe-Si-Al alloys, in H.P.J. Wijn (ed.), *Magnetic Properties of Metals*, Landolt-Börnstein New Series, Vol. 19-i1, Berlin: Springer-Verlag, 1994, pp. 33-139.

[40] IEC Standard Publication 60404-8-4, Specifications for individual materials – Cold-rolled electrical non-alloyed steel sheet and strip delivered in the fully processed state, IEC Central Office, Geneva, 2013.

[41] IEC Standard Publication 60404-8-8, Specifications for individual materials – Thin magnetic steel strip for use at medium frequencies, IEC Central Office, Geneva, 1991.

[42] D. Snell and A. Coombs, Novel coating technology for non-oriented electrical steels, *J. Magn. Magn. Mater.* **215-216**: 133-135, 2000.

[43] H. Shimanaka, Y. Ito, T. Irie, K. Matsumura, E. Nakamura, and Y. Shono, Non-oriented Fe-Si steels useful for energy efficient electrical apparatus, in H.R. Marden and E.T. Stephenson (eds.) *Energy efficient electrical steels*, The Metallurgical Society of AIME, 1980, pp. 193-204.

[44] G. Bertotti, G. Di Schino, A. Ferro Milone, and F. Fiorillo, On the effect of grain size on magnetic losses of 3 % non-oriented Si-Fe., *J.Phys. (France)* **46-C6**: 385 – 388, 1985.

[45] M. Shiozaki and Y. Kurosaki, The effects of grain size on the magnetic properties of nonoriented electrical steel sheets, *J. Mater. Eng.* 11: 37-43, 1989.

[46] G. Bertotti, Direct relation between hysteresis and dynamic losses in soft magnetic materials, *J.Phys. (France)* **46-C6**: 389 – 392, 1985.

[47] T. Kubota, Recent progress in non-oriented silicon steel, *Proc. 16th Soft Magn. Mater. Conf.,* The Max Planck Institut für Eisenforschung, Düsseldorf, 2004, pp. 79-85.

[48] P. Brissonneau, J. Quenin, and J. Verdun, A new sheet with a pseudo-cubic texture for application to large rotating machines, *Proc. 7th Soft Magn. Mater. Conf.,* The University College, Cardiff, 1985, pp. 209-211.

[49] M. LoBue, C. Sasso. V. Basso, F. Fiorillo, and G. Bertotti, Power losses and magnetization process in Fe-Si non-oriented steels under tensile and compressive stresses, *J. Magn. Magn. Mater.* **215-216**: 124-126, 2000.

[50] F. Ossart, Dégradation du comportement magnétique des tôles lors de leur mise en oeuvre industrielle: mise en évidence expérimentale et modélisation, *Mec. Ind.* **1**: 165-176, 2000.

[51] J. Degauque and F. Fiorillo, Alliages magnétiques doux enrichis en silicium, in A. Kedous-Lebouc (ed.), *Matériaux magnétiques en genie électrique*, Paris: Hermes-Lavoisier, 2006, pp. 227-286.

[52] B. Viala, J. Degauque, M. Fagot, M. Baricco, E. Ferrara, and F. Fiorillo: "Study of the brittle behavior of annealed Fe 6.5 wt % Si ribbons produced by planar flow casting", *Materials Science and Engineering A* , 212: 62-68, 1996.

[53] S. Crottier-Combe, S. Audisio, J. Degauque, E. Ferrara, M. Pasquale, and F. Fiorillo, Magnetic properties of FeSi 6.5 wt % alloys obtained by a $SiCl_4$ based CVD process, *J. Magn. Magn. Mater.* **160:** 151-153, 1996.

[54] T. Yamaji, M. Abe, Y. Takada, K. Okada, and T. Hiratani, Magnetic properties and workability of 6.5 % silicon steel sheet manufactured in continuous CVD siliconizing line, *J. Magn. Magn. Mater.* **133:** 187-189, 1994.

[55] N. Namikawa, H. Ninomiya, and T. Yamaji, High silicon steel sheets realizing excellent high frequency reactor performance, *JFE Technical Report.* **6:** 12-17, 2005.

[56] J. C. Perrier and P. Brissonneau, Some physical and mechanical properties of Si-Al-Fe alloys," *J. Magn. Magn. Mater.* **26**: 79-82, 1982.

[57] IEC Standard Publication 60404-8-7, Specifications for individual materials – Cold-rolled grain-oriented electrical steel strip and sheet delivered in the fully-processed state, IEC Central Office, Geneva, 2008.

[58] T. Yamamoto, S. Taguchi, A. Sakakura, and T. Nozawa, Magnetic properties of grain-oriented silicon steels with high permeability Orientcore HI-B, *IEEE Trans. Magn.* **8**: 677-681, 1972.

[59] I. Goto, I. Matoba, T. Imanaka, T. Gotoh, and T. Kan, Development of a new grain-oriented silicon steels "RG-H" with high permeability, *Proc. 2nd Soft Magn. Mater. Conf.*, The University College, Cardiff, 1975, pp. 262-268.

[60] H.C. Fiedler, A new high induction grain-oriented 3% silicon-iron, *IEEE Trans. Magn.* **13**: 1433-1436, 1977.

[61] N. Takahashi, Y. Suga, and H. Kobayashi, Recent developments in grain-oriented silicon-steel, *J. Magn. Magn.Mater.* **160**: 98-101, 1996.

[62] JFE Electrical Steel Sheets, www.jfe-steel.co.jp/en/products/electrical/catalog/

[63] L.R. Dupré, F. Fiorillo, J. Melkebeek, A.M. Rietto, and C. Appino, Loss versus cutting angle in grain-oriented Fe-Si laminations, *J. Magn. Magn.Mater.* **215-216**: 112-114, 2000.

[64] T. Kubota, M. Fujikura, and Y. Ushigami, Recent progress and future trend on grain-oriented silicon-steel, *J. Magn. Magn.Mater.* **215-216**: 69-73, 2000.

[65] F. Fiorillo, Advances in Fe-Si properties and their interpretation, *J. Magn. Magn. Mater.* **157-158**: 428-431, 1996.

[66] K.I. Arai and K. Ishiyama, Recent developments of new soft magnetic materials, *J. Magn. Magn. Mater.* **133**: 233-237, 1994.

[67] D. Kohler, Promotion of cubic grain growth in 3% silicon iron by control of annealing atmosphere composition, *J. Appl. Phys.* **31**: 408S-409S, 1960.

[68] A. Ferro, G. Montalenti, and G.P. Soardo, Temperature dependence of power loss anomalies in directional Fe-Si 3%, *IEEE Trans. Magn.* **12**: 870-872, 1976.

[69] J.W. Shilling and G.L. Houze, Jr., Magnetic properties and domain structure in grain-oriented 3 % Si-Fe, *IEEE Trans. Magn.* **10**: 195-223, 1974.

[70] K. Foster and M.F. Littmann, Factors affecting core losses in oriented electrical steels at moderate inductions, *J. Appl. Phys.* **57:** 4203-4208, 1985.

[71] T. Yamamoto, S. Taguchi, S. Sakakura, and A. Nozawa, Magnetic properties of grain-oriented silicon steel with high permeability Orientcore HI-B, *IEEE Trans. Magn*. **8:** 123-127, 1972.

[72] D. Kowal, P. Sergeant,. L. Dupré, and A. Van den Bossche, Comparison of non-oriented and grain-oriented material in an axial flux permanent magnet machine, *IEEE Trans. Magn*. **46:** 279-285, 2010.

[73] C. Cyr, Modélisation et caractérisation des matériaux magnétiques composites doux utilisés dans les machines électriques, Thèse Université Laval, Québec, 2007.

[74] I. P. Gilbert, V. Moorthy, S. J. Bull, J. T. Evans, and A. G. Jack, "Development of soft magnetic composites for low-loss applications, *J. Magn. Magn. Mater.* **242-245**: 232-234, 2002.

[75] J.A. Bas, J.A. Calero, and M.J. Dougan, Sintered soft magnetic materials. Properties and applications, *J. Magn. Magn. Mater.* **254-255:** 391-398, 2003.

[76] F. Mazaleyrat and L.K. Varga, Ferromagnetic nanocomposites, *J. Magn. Magn. Mater.* **215-216:** 253-259, 2000.

[77] I. Otsuka, K. Wada, Y. Maeta, T. Kadomura, and M. Yagi, Magnetic properties of Fe-based amorphous powders with high-saturation induction produced by spinning water atomization process (SWAP), *IEEE Trans. Magn.* **44:** 3891-3894, 2008.

[78] M. Müller, A. Novy, M. Brunner, and R. Hilzinger, Powder composite cores of nanocrystalline soft magnetic FeSiB-CuNb alloys, *J. Magn. Magn. Mater.***196-197:** 357-358, 1999.

[79] H. Matsumoto, A. Urata, Y. Yamada, and S. Yoshida, MPCG for large-current using ultra low loss dust material "SENNTIX" formed by one-piece construction, NEC Technical Journal, **2:** 66-70, 2007.

[80] O. De la Barrière, C. Appino, F. Fiorillo, C. Ragusa, H. Ben Ahmed, M. Gabsi, F. Mazleyrat, and M. LoBue, Loss separation in soft magnetic composites, *J. Appl. Phys.* **109:** 07A317-1 - 07A317-3, 2011.

[81] M. Yagi, I. Endo, I. Otsuka, H. Yamamoyo, R. Okuno, H. Koshimoto, and A. Shintani, Magnetic properties of Fe-based amorphous powder cores produced by a hot pressing method, *J. Magn. Magn. Mater.* **215-216:** 284-287, 2000.

[82] C. Oliver, Advances in powder metallurgy of soft magnetic materials, *IEEE Trans. Magn.* **31:** 3982-3984, 1995.

[83] P. Jansson, Advances in soft magnetic composites based on iron powder, *Proc. Soft magnetic Materials 98* (Gorham-Intertech, 1998).

[84] M. De Wulf, L. Anestiev, L. Dupré, L. Froyen, and J. Melkebeek, Magnetic properties and loss separation in iron powder soft magnetic composite materials, *J. Appl. Phys.* **91:** 7845-7847, 2002.

[85] C. Appino, O. Bottauscio, O. de la Barrière, F. Fiorillo, A.Manzin, and C. Ragusa, Computation of Eddy Current Losses in Soft Magnetic Composites, *IEEE Trans. Magn.* **48:** 3470-3473, 2012.

[86] Z. Zhang, F. Profumo, A. Tenconi, and M. Santamaria, Analysis and experimental validation of performance for an axial flux permanent magnet brushless DC motor with powder iron metallurgy cores, *IEEE Trans. Magn.* **33:** 4194-4196, 1997.

[87] G. J. Atkinson, A.G. Jack, B.B. Jensen, and J. Washington, Soft magnetic composite in optimized machine design, Magnews (Summer 2009) pp. 18-20.

[88] A.G. Jack, B.C. Mecrow, and C.P. Maddison, Combined radial and axial permanent magnet motors using soft magnetic composites, Proc IEE 9th Int. Conf. on Electrical Machines and Drives, Conf. Publication n°. 468, Canterbury, UK, 1999.

[89] Y. Huang, J. Zhu, Y. Guo, Q. Hu, Development of a high-speed claw pole motor with soft magnetic composite core, Proc. IEMDC '07 Conf., Vol. 2, pp. 1564-1568, 2007.

[90] T. Masumoto, I. Ohnaka, A. Inoue, and M. Hajiwara, Production of Pd-Cu-Si amorphous wires by melt spinning method using rotating water, *Scripta Met.* **15**: 293-296,1981.

[91] M. Vazquez and A.P. Zhukov, Magnetic properties of glass-coated amorphous and nanocrystalline microwires, *J. Magn. Magn. Mater.***160:** 223-228, 1996.

[92] H. Chiriac, Preparation and characterization of glass covered magnetic wires, *Mater. Sci. Eng. A* **304 306:** 166-171,2001.

[93] A. Inoue and A. Makino, Preparation and soft magnetic properties of Fe-based bulk amorphous alloys, *J. Phys. IV (France)* **8-Pr2**: 3-10, 1998.

[94] A. Inoue, A. Makino, and T. Mizushima, Ferromagnetic bulk glassy alloys, *J. Magn. Magn. Mater.* **215-216**: 246 – 252, 2000.

[95] R.C. O'Handley, *Modern magnetic materials*, New York: Wiley, 2000, p. 391.

[96] R.C. O'Handley, Fundamental magnetic properties, in F.E. Luborsky (ed.), *Amorphous Metallic Alloys*, London: Butterworths, 1983, p. 257.

[97] H. Kronmüller, N. Moser, and T. Reininger, Magnetization processes domain patterns and microstructure in amorphous alloys, *Anal. Fis.* **B86**: 1-6, 1990.

[98] R. Hasegawa and D. Azuma, Impacts of amorphous metal-based transformers in energy efficiency and environment, *J. Magn. Magn. Mater.* **320**: 2451 – 2456, 2008.

[99] V.R.V. Ramanan, Metallic glasses in distribution transformer applications: an update, *J. Mater. Eng.* **13**: 119-127, 1991.

[100] C. H. Smith, Applications of rapidly solidified soft magnetic alloys, in H.H. Liebermann (ed.), *Rapidly Solidified Alloys*, New York: Marcel Dekker, 617-663, 1993.

[101] M. Knobel and K.R. Pirota, Giant magnetoimpedance: concepts and recent progress, *J. Magn. Magn. Mater.* **242-245**: 246 – 252, 2002.

[102] L.V. Panina and K. Mohri, Effect of magnetic structure on giant magnetoimpedance in Co-rich amorphous alloys, *J. Magn. Magn. Mater.* **157-158**: 137 – 140, 1996.

[103] G. Bertotti, E. Ferrara, F. Fiorillo, and P. Tiberto, Magnetic properties of rapidly quenched soft magnetic materials, *Mater. Sci. Eng.* **A226-228**: 603-613, 1997.

[104] Y. Yoshizawa, S. Oguma, and K. Yamauchi, New Fe-based magnetic alloy composed of ultrafine grain structure, *J. Appl. Phys.* **64**: 6044-6046, 1988.

[105] A. Makino, A. Inoue, and T. Masumoto, Nanocrystalline soft magnetic Fe-M-B (M=Zr, Hf, Nb) alloys produced by crystallization of amorphous phase, *Mater. Trans. JIM* **36**: 924-938, 1995.

[106] G. Herzer, Grain size dependence of coercivity and permeability in nanocrystalline ferromagnets, *IEEE Trans. Magn.* **26**: 1397-1402, 1990.

[107] M.A. Willard, D.E. Laughlin, M.E. McHenry, D. Thoma, K. Sickafus, J.O. Cross, and V.G. Harris, Structure and magnetic properties of $(Fe_{0.5}Co_{0.5})_{88}Zr_7B_4Cu_1$ nanocrystalline alloys, *J. Appl. Phys.* **84**: 6773-6777, 1998.

[108] Y. Yoshizawa and Y. Ogawa, Magnetic properties of high B_s nanocrystalline FeCoCuNbSiB alloys, *IEEE Trans. Magn.* **4**: 3271-3273, 2005.

[109] A. Makino, Nanocrystalline soft magnetic Fe-Si-B-P-Cu alloys with hugh B of 1.8 – 1.9 T contributable to energy saving, *IEEE Trans. Magn.***48**: 1331-1335, 2012.

[110] A. Setyawan, K. Takenaka, P. Sharma, M. Nishijima, N. Nishiyama, and A. Makino, Magnetic properties of 120 mm wide ribbons of high Bs and low core loss NANOMET® alloy, *J. Appl. Phys.* **117**: 17B715, 2015.

[111] K. Takenaka, A. Setyawan, P. Sharma, M. Nisijima, N. Nishiyama, and A. Makino, Industrialization of nanocrystalline Fe-Si-B-Cu alloys for high magnetic flux density cores, *J. Magn. Magn. Mater.* **401**: 479-483, 2016.

[112] E. Ferrara, C. De Luigi, C. Beatrice, C. Appino, and F. Fiorillo, Energy loss versus magnetizing frequency in field-annealed nanocrystalline alloys, *J. Magn. Magn. Mater.* **215-216**: 466-468, 2000.

[113] L. Kraus, K. Závěta, O. Heczko, P. Duhaj, G. Vlasák, and J. Schneider, Magnetic anisotropy in as-quenched and stress-annealed amorphous and nanocrystalline $Fe_{73.5}Cu_1Nb_3Si_{13.5}B_9$ alloys, *J. Magn. Magn. Mater.* **112**: 275-277, 1992.

[114] F. Alves and R. Barrué, Anisotropy and domain patterns of flash stress-annealed soft amorphous and nanocrystalline alloys, *J. Mater. Eng.* **254-255**: 155-157, 2003.

[115] Y. Suzuki, J. Haimovich, and T. Egami, Bond-orientational anisotropy in metallic glasses observed by x-ray diffraction, *Phis. Rev. B* **35**: 2162-2168, 1987.

[116] G. Herzer, Creep induced magnetic anisotropy in nanocrystalline Fe-Cu-Nb-Si-B alloys, *IEEE Trans. Magn.* **30**: 4800-4802, 1994.

[117] G. Herzer, Amorphous and nanocrystalline soft magnets, in *Magnetic Hysteresis in Novel Magnetic Materials*, NATO Science Series E, G.C.Hadjipanayis, Ed., 1997, pp. 1-20.

[118] Nanocrystalline cores Nanophy. Data sheet. http://www.aperam.com.

[119] M. Zucca, O. Bottauscio, C. Beatrice, A. Hadadian, F. Fiorillo, and L. Martino, "A study on energy harvesting by amorphous strips", *IEEE Trans. Magn.* **50**: 8002104, 2014.

[120] T. Sasaki, E. Shimomura, and K. Yamada, Variation of power losses with stresses in amorphous sheets for power applications, *IEEE Trans. Magn.* **23**: 3587-3589, 1987.

[121] F. Luborsky and J.J. Becker, Strain-induced anisotropy in amorphous alloys and the effect of toroid diameter on magnetic properties, *IEEE Trans. Magn.* **15**: 1939-1945, 1979.

[122] P. Allia, P. Tiberto, M. Baricco, M. Knobel, and F. Vinai, Nanostructured materials for soft magnetic applications produced by fast dc Joule heating, *IEEE Trans. Magn.* **30**: 4797-4799, 1994.

[123] J. Petzold, Applications of nanocrystalline soft magnetic materials for modern electronic devices, *Scripta Mater.* **48**: 895-901, 2003.

[124] R. Hasegawa, Advances in amorphous and nanocrystalline magnetic materials, *J. Magn. Magn. Mater.* **304:** 187-191, 2006.

[125] Rybak, et al., USA Patent 6, 106, 376, Bulk metallic glass motor and transformer parts and method of manufacture, 2000.

[126] G. Couderchon and J.F. Thiers, Some aspects of magnetic properties of Ni-Fe and Co-Fe alloys, *J. Magn. Magn. Mater.* 26: 196-214, 1982.

[127] G. Y. Chin, Review of magnetic properties of Fe-Ni alloys, *IEEE Trans. Magn.* **7**: 102-113, 1971.

[128] Y. Nakamura, The Invar problem, *IEEE Trans. Magn.* **12**: 278-291, 1976.

[129] J. Smit and H.P.J. Wijn, *Ferrites*, New York, Wiley, 1959.

[130] L. Néel, Proprietés magnétiques des ferrites: ferrimagnétisme et antiferromagnétisme, *Ann. Phys.* **3**: 137-198, 1948.

[131] P.W. Anderson, Antiferromagnetism. Theory of the superexchange interaction, *Phys. Rev*. 79: 350-356, 1950.

[132] R. Pauthenet, Aimantation spontanée des ferrites, *Ann.Phys.* **7**: (1952) 710-745.

[133] H. Pascard, Basic concepts for high permeability in soft ferrites, *J. Phys. IV (France)* **8-Pr2**: 377-384, 1998.

[134] D. Gignoux, Irreversibilité des processus d'aimantation et hystéresis dans les matériaux ferromagnétiques réels : le role des défauts, in *Magnétisme*, E. du Trémolet de Lacheisserie, Ed. Presses Universitaires Grenoble, 1999, pp. 211-248.

[135] F. Fiorillo, C. Appino, and M. Pasquale, Hysteresis in magnetic materials, in *The Science of Hysteresis*, G. Bertotti and I. Mayergoyz, Eds., Academic Press, 2006, Vol. III, pp. 1-189.

[136] J. Hanuszkiewicz, D. Holz, E. Eleftheriou, and V. Zaspalis, Materials processing issues influencing the frequency stability of the initial magnetic permeability of MnZn ferrites, *J. Appl. Phys.* **103**: 103907, 2008.

[137] V. Tsakaloudi and V. T. Zaspalis, A new Mn-Zn ferrite for high-speed data transmission applications in telecommunication networks, *J. Magn. Magn. Mater.* **310**: 2540-2542, 2007.

[138] V. Loyau, G.-Y. Wang, M. LoBue, and F. Mazaleyrat, An analysis of Mn-Zn ferrite microstructure by impedance spectroscopy, scanning transmission electron microscopy and energy dispersion spectrometry characterizations, *J. Appl. Phys.,***111**: 053928, 2012.

[139] F. Fiorillo, C. Beatrice, O. Bottauscio, and E. Carmi, Eddy-Current Losses in Mn-Zn Ferrites, *IEEE Trans. Magn.* **50**: 6300109, 2014.

[140] F. Fiorillo, C. Beatrice, O. Bottauscio, A. Manzin, and M. Chiampi, An approach to magnetic losses and their frequency dependence in Mn-Zn ferrites, *Appl. Phys. Lett*. **89:** 122513, 2006.

[141] F. Fiorillo and C. Beatrice, A comprehensive approach to broadband characterization of soft ferrites, *Int. J. Appl. Electromagnetics Mech.* **48**: 283-294, 2015.

[142] H. Suhl, Theory of the magnetic damping constant, *IEEE Trans. Magn.* **34**: 1834-1838, 1998.

[143] F. Fiorillo, C. Beatrice, M. Coïsson, and L. Zhemchuzhna: "Loss and permeability dependence on temperature in soft ferrites", *IEEE Trans. Magn.* **45**: 4242-4245, 2009.

[144] M. Pardavi-Horvath, Microwave applications of soft ferrites, *J. Magn. Magn. Mater.* **215-216**: 171 – 183, 2000.

[145] V.G. Harris, Modern microwave ferrites, *IEEE Trans. Magn.* **48**: 1075-1104, 2012.

Soft Magnetic Materials

F. Fiorillo, G. Bertotti, C. Appino, M. Pasquale
Istituto Nazionale di Ricerca Metrologica
Strada delle Cacce 91, Torino 10135, Italy

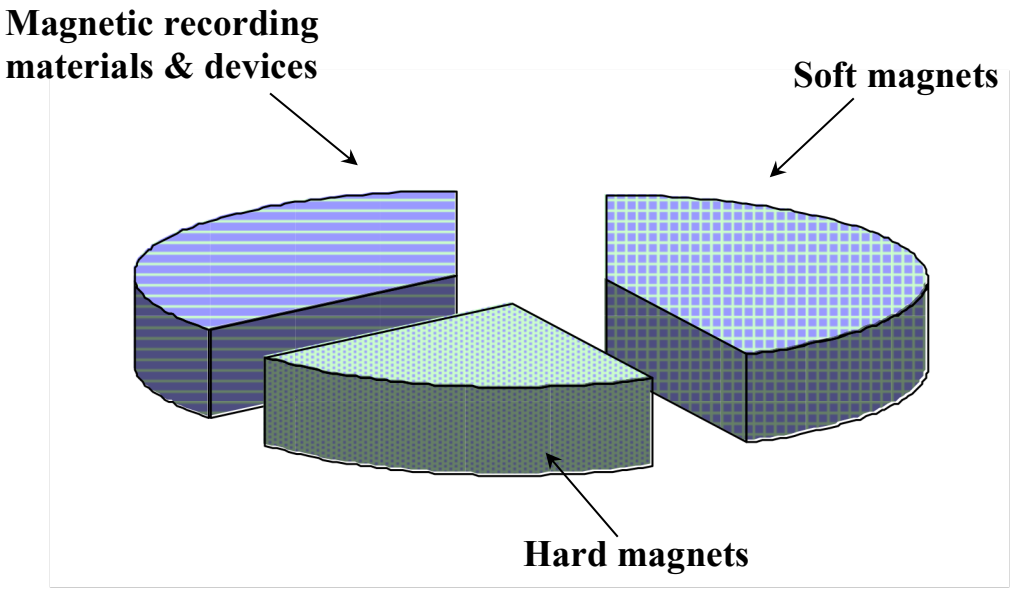

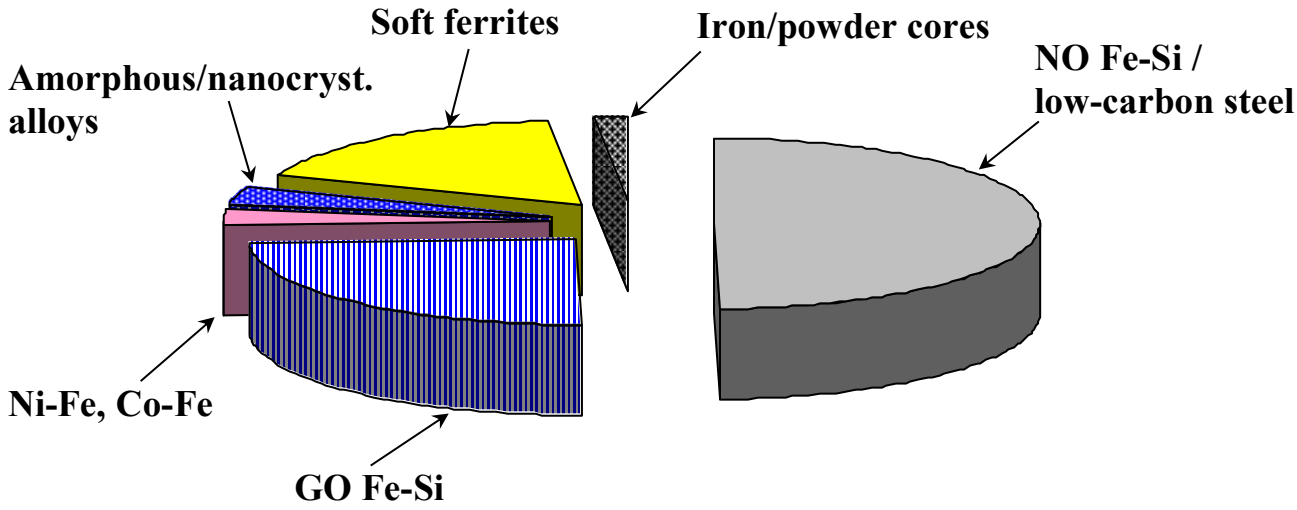

Fig. 1 – The soft magnets cover a large proportion of the global market of magnetic materials, with a value estimated in the year 2015 around ◘ $20 \cdot 10^9$. A major share of the market is covered by the grain-oriented (GO) and non-oriented (NO) electrical steels.

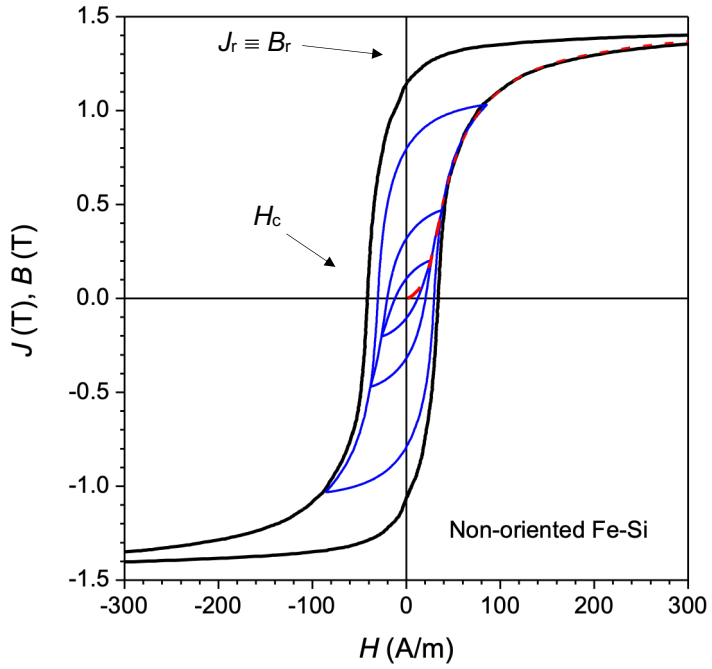

Fig. 2 – Magnetic hysteresis loops in a non-oriented Fe-Si sheet under quasi-static excitation. The remanent polarization J_r (always coincident with the remanent induction B_r) and the coercive field H_c are put in evidence. The dashed line shows the normal magnetization curve, obtained as the locus of the tip points of the nested symmetric minor loops. This curve is practically coincident with the initial magnetization curve. There are no detectable differences between the $B(H)$ and $J(H)$ loops in soft magnets at technical induction values.

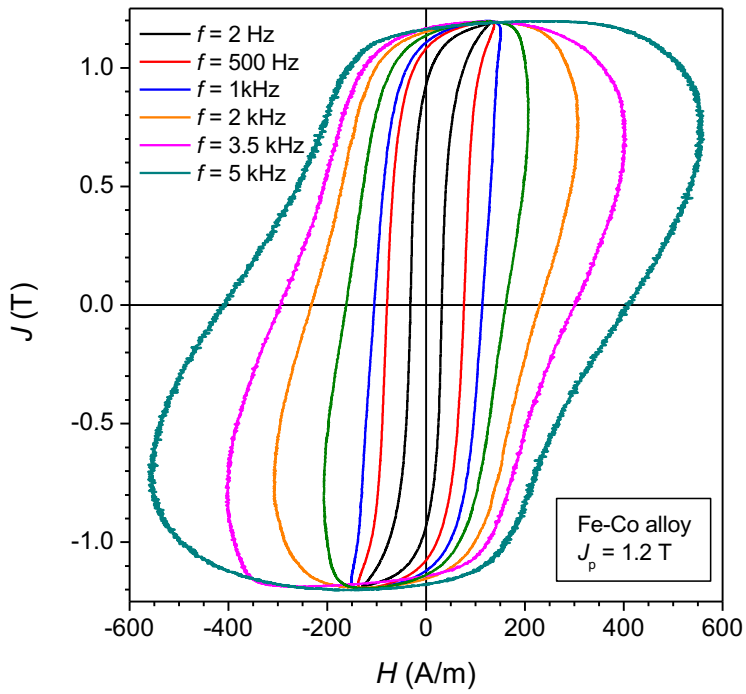

Fig. 3 – Magnetic hysteresis loops $J(H)$ versus magnetizing frequency in a 0.20 mm thick $Fe_{49}Co_{49}V_2$ sheet excited with sinusoidal polarization $J(t)$ of peak value $J_p = 1.2$ T.

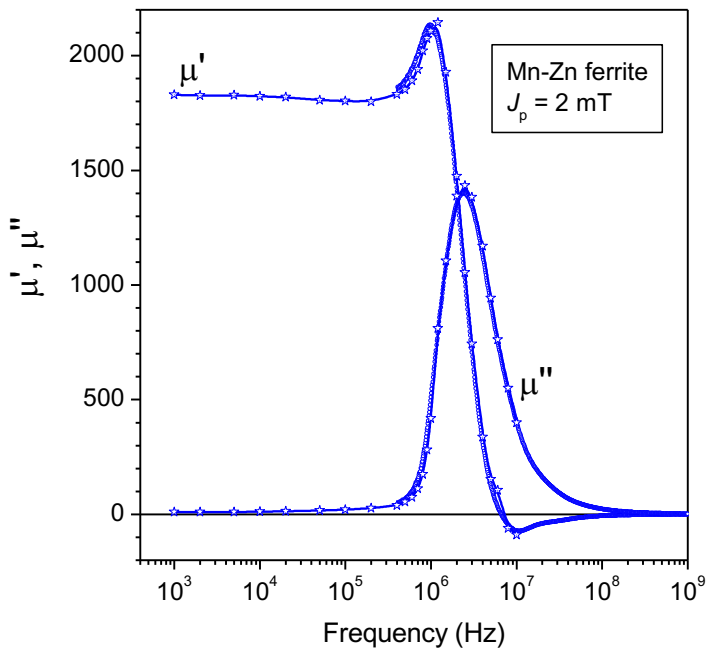

Fig. 4 – Broadband behavior of real μ' and imaginary μ'' initial permeability components in a Mn-Zn ferrite. The measurements are made by combination of fluxmetric and transmission line methods at the peak polarization value J_p = 2 mT.

	Density (kg/m^3)	Thermal conductivity ($W \cdot m^{-1} \cdot K^{-1}$)	Electrical resistivity ($\Omega \cdot m$)	Yield stress (tension) (MPa)	Fracture stress (tension) (MPa)	Vickers hardness
Polycrystalline Fe	7867	79.6	$10.5 \cdot 10^{-8}$	70 - 150	290	100 - 150
NO Fe-(1.0 wt%)Si *NO Fe-(3.5 wt%)Si*	7800 7600	40 20	$25 \cdot 10^{-8}$ $50 \cdot 10^{-8}$	300 400	400 530	130 220
GO Fe-(3 wt%)Si	7650	20	$45 \cdot 10^{-8}$	320	380	200
Bonded-sintered Fe powders	7100 - 7700	10 - 30	$50 \cdot 10^{-6}$- $1000 \cdot 10^{-6}$	50 - 250	50 - 250	140
Permalloy/Mumetal ($Fe_{15}Ni_{80}Mo_5$)	8700	19	$70 \cdot 10^{-8}$	280	700	160
Permendur ($Fe_{49}Co_{49}V_2$)	8200	32	$40 \cdot 10^{-8}$	200 - 400	250 - 650	180 - 220
$Fe_{50}Ni_{50}$ $Fe_{52}Ni_{48}$	8120	13	$48 \cdot 10^{-8}$	250	520	120
Sintered ferrites (Mn-Zn and Ni-Zn)	4800 - 5300	4 - 7	$10^{-2} – 10^{5}$	60	60	600-800
Amorphous alloys (Fe- and Co-based)	7200 - 7900	9	120 - 140 $\cdot 10^{-8}$	700	2800	800
Nanocrystalline alloys(FINEMET)	7200	5	$118 \cdot 10^{-8}$	150	150	800

Table 1 – Physical and mechanical parameters of representative soft magnetic materials.

	Composition (*wt% cryst. alloys, at% amorphous alloys)*	Max. relative permeability μ_{max}	Coercive field H_c (A/m)	Saturation polarization J_s (T)	Curie temperature T_c (°C)	Saturation magnetostriction $\lambda_s = (\Delta l/l)_{Js}$
Polycrystallin Fe	Fe_{100}	$3\text{-}50\cdot10^3$	10-100	2.16	770	$5\cdot10^{-6}$
NO Fe-Si	$Fe_{96\text{-}99}\text{-}Si_{1\text{-}4}$	$3\text{-}10\cdot10^3$	30 - 80	1.96-2.12	735-765	$10\cdot10^{-6}$
GO Fe-Si	$Fe_{97}\text{-}Si_3$	$15\text{-}80\cdot10^3$	4 - 15	2.02	750	$1\text{-}3\cdot10^{-6}$
Fe-(6.5 wt%)Si	$Fe_{93.5}Si_{6.5}$	$5\text{-}30\cdot10^3$	10 - 40	1.80	690	$5\cdot10^{-7}$
Sintered/bonded powders	$Fe_{99.5}P_{0.5}$	$10^2\text{-}10^3$	100 -500	1.65-1.95	770	----
Permalloy / Mumetal	$Fe_{15}Ni_{80}Mo_5$ / $Fe_{14}Ni_{77}Mo_4Cu_5$	$5\cdot10^5$	0.3 -2	0.75-0.80	420	$1\cdot10^{-6}$
Permendur	$Fe_{49}Co_{49}V_2$	$2\cdot10^3$	30-100	2.35	930	$60\cdot10^{-6}$
*Fe*50-*Ni*50	$Fe_{52}Ni_{48}$	10^5	4	1.60	450	$25\cdot10^{-6}$
Sintered ferrites	$(Mn,Zn)O\cdot Fe_2O_3$ $(Ni,Zn)O\cdot Fe_2O_3$	$10^3\text{-}10^4$ $10^2\text{-}10^3$	5 - 20 20 -200	0.4 - 0.5 0.2 – 0.35	130 – 280 110 - 400	$-2\cdot10^{-6}$ $-20\cdot10^{-6}$
Sendust	$Fe_{85}Si_{9.5}Al_{5..5}$	$50\cdot10^3$	5-10	1.70	670	$1\cdot10^{-6}$
Amorphous alloys (Fe-based)	$Fe_{78}B_{13}Si_9$	10^5	2-5	1.56	415	$37\cdot10^{-6}$
Amorphous alloys (Co-based)	$Co_{67}Fe_4B_{14.5}Si_{14.5}$	$5\cdot10^5$	0.5-1	0.62	320	$5\cdot10^{-7}$
Nanocrystalline alloys (FINEMET)	$Fe_{73.5}Cu_1Nb_3Si_{13.5}B_9$	$5\cdot10^5$	0.5-1	1.24	600	$2\cdot10^{-6}$
Nanocrystalline alloys (NANOPERM)	$Fe_{86}Cu_1Zr_7B_6$	$5\cdot10^4$	3	1.52	600	$1\cdot10^{-7}$

Table 2 - Representative soft magnetic materials and typical values of some basic magnetic parameters at room temperature. μ_{max} ≡ maximum DC relative permeability; H_c ≡ coercive field; J_s ≡ saturation polarization; T_c ≡ Curie temperature, λ_s ≡ saturation magnetostriction. The composition is given in wt %, but for the amorphous and nanocrystalline alloys, where it is expressed in at %.

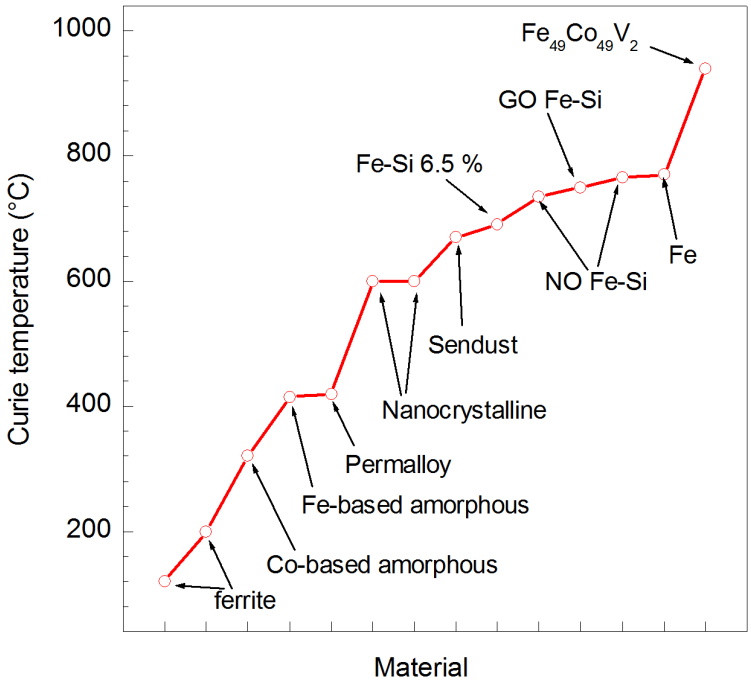

Fig. 5 – Curie temperature of the main applicative soft magnetic materials.

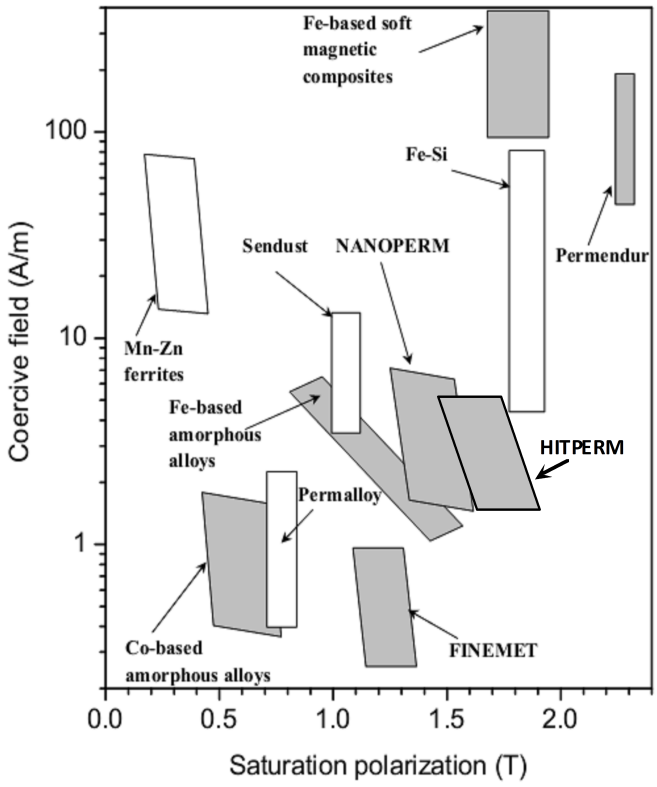

Fig. 6 – Coercive field landscape in applicative soft magnetic alloys.

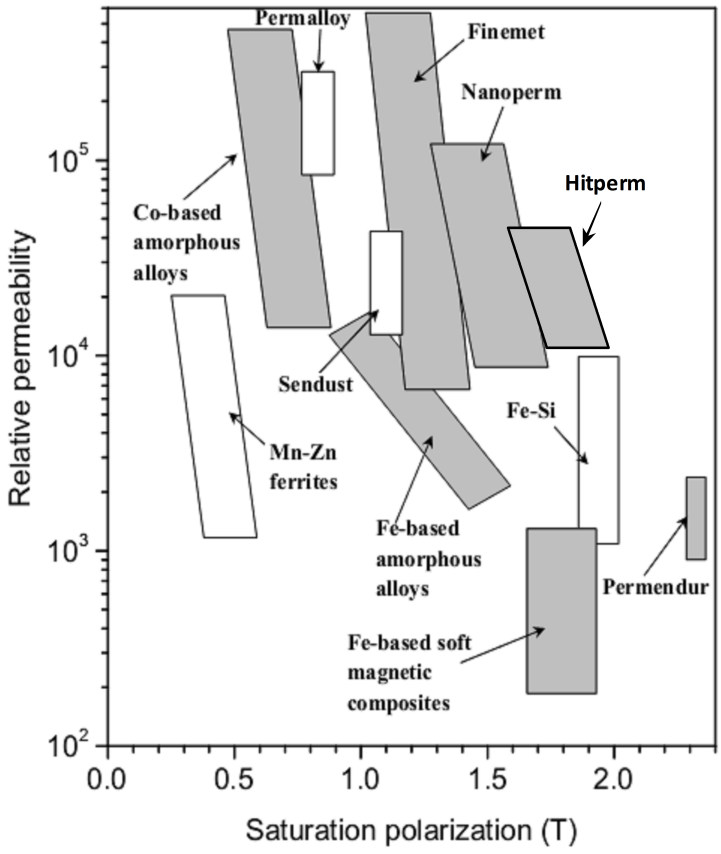

Fig. 7 – As in Fig. 6 for the maximum permeability value.

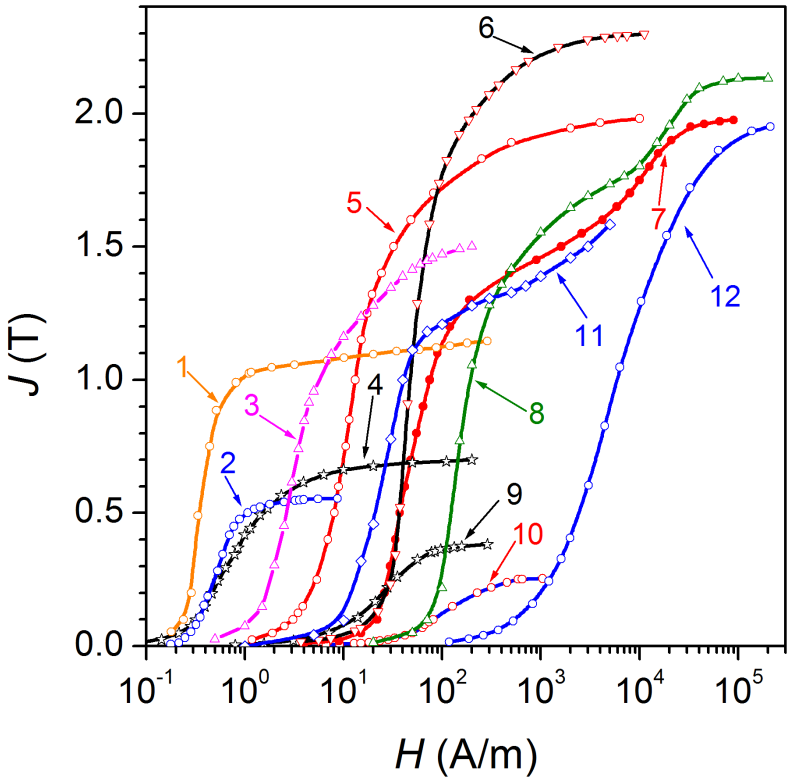

Fig. 8 – Initial magnetization curve of several types of soft magnets: 1) FINEMET nanocrystalline alloys $Fe_{73.5}Cu_1Nb_3B_9Si_{13.5}$; 2) amorphous alloys $Co_{67}Fe_4B_{14.5}Si_{14.5}$; 3) amorphous alloys $Fe_{78}B_{13}Si_9$; 4) $Fe_{15}Ni_{80}Mo_5$ (mumetal); 5) grain-oriented Fe-(3 wt %) Si sheets; 6) $Fe_{49}Co_{49}V_2$ alloys (permendur); 7) non-oriented Fe-(3.5 wt%)Si laminations; 8) Low-C steels; 9) Mn-Zn soft ferrites; 10) Ni-Zn soft ferrites; 11) Fe-(6.5 wt%)Si; 12) Fe powder cores (Soft Magnetic Composites).

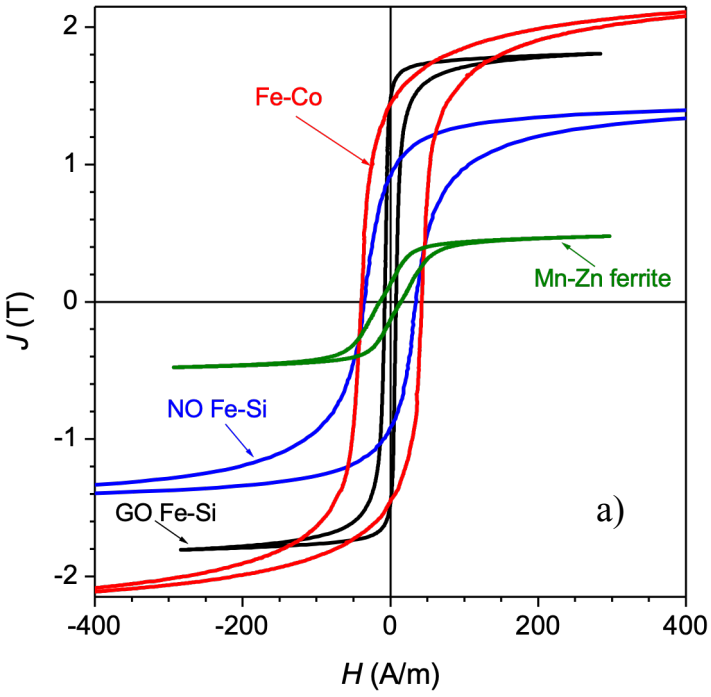
Fe-Co
Mn-Zn ferrite
NO Fe-Si
GO Fe-Si
a)
J (T)
H (A/m)
2
1
0
-1
-2
-400
-200
0
200
400

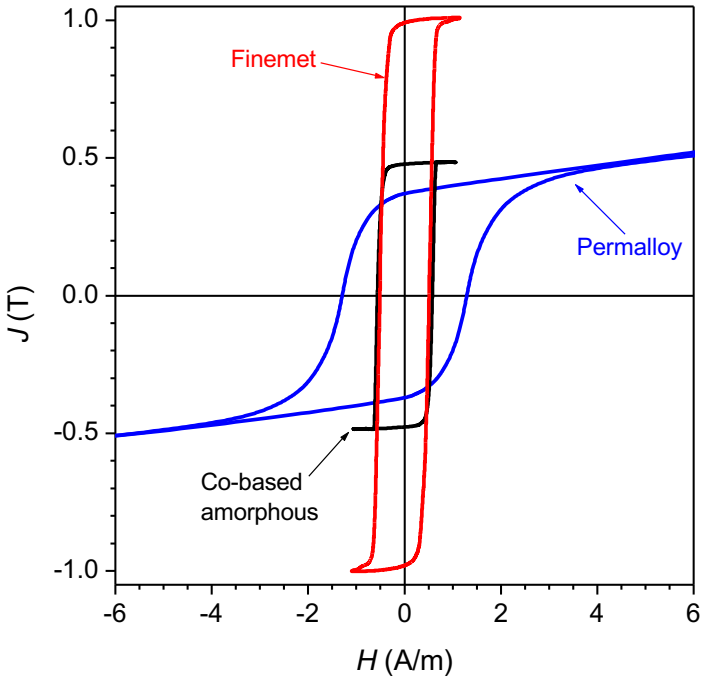
Finemet
Permalloy
Co-based
amorphous
J (T)
H (A/m)
1.0
0.5
0.0
-0.5
-1.0
-6
-4
-2
0
2
4
6

b)

Fig. 9 – DC hysteresis loops in different soft magnetic alloys. a) $Fe_{49}Co_{49}V_2$ (Permendur/Vacoflux) ; Grain-oriented Fe-(3wt%)Si; non-oriented Fe-(3wt%)Si; Mn-Zn sintered ferrite. b) $Fe_{73.5}Cu_1Nb_3B_9Si_{13.5}$ nanocrystalline alloy (Finemet); amorphous $Co_{67}Fe_4B_{14.5}Si_{14.5}$ alloy; $Fe_{20}Ni_{80}$ (Permalloy/Mumetal). All materials are heat treated for best DC response. The amorphous and nanocrystalline ribbons are annealed under a saturating longitudinal magnetic field.

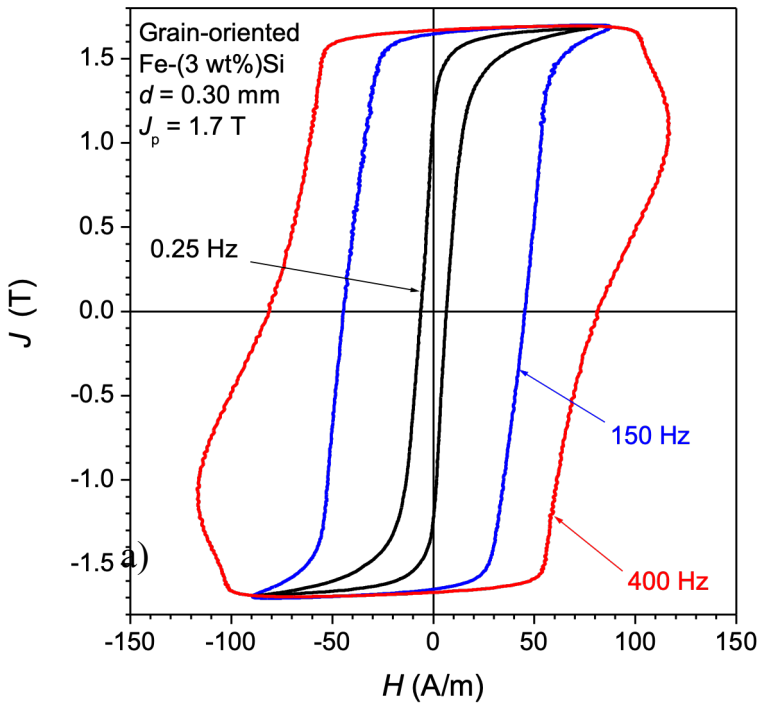

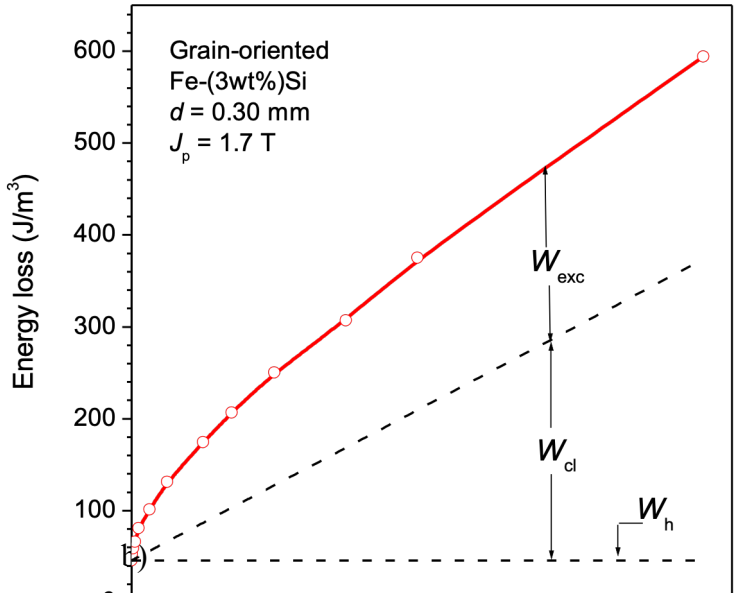

Fig. 10 – a) Hysteresis loops in a grain-oriented 0.30 mm thick Fe-Si steel sheet measured under sinusoidal polarization of peak value J_p = 1.7 T at different frequencies. b) Corresponding behavior of the energy loss per cycle and unit volume $W(f)$ (area of the hysteresis loop) and its decomposition in the quasi-static W_h, classical W_{cl}, and excess W_{exc} components.

Table 3 - Typical impurities and their concentrations (wt ppm) in different grades of iron and in low-carbon steel.

Iron type	C	N	O	Mn	P	S	Si	Cu	Ni
ARMCO	150	20	150	280	50	250	30	150	--
Electrolytic	40	100	100	15	20	30	30	40	10
H_2-treated	30	10	30	280	40	< 30	--	--	--
Zone-refined	7	< 10	2	0.5	< 0.1	0.2	--	1.5	0.50
Low-carbon steel	50 - 1000	30 - 200	200 - 1000	5000	200 - 1000	50 - 300	10^3-10^4	100	--

- Melting, degassing, continuous casting of slabs.
- Re-heating (1000 °C – 1250 °C) and hot rolling to 2 mm – 2.5 mm thickness.
- Pickling and cold rolling to final thickness (0.50 mm – 1 mm).
- Intermediate annealing for re-crystallization.
- Temper rolling (reduction 3% to 5%).
- Punching.
- Final annealing (decarburization, grain-growth, controlled surface oxidation).
- Core assemblage.

Table 4 - The sequence of thermomechanical treatments in low-carbon steel sheet processing.

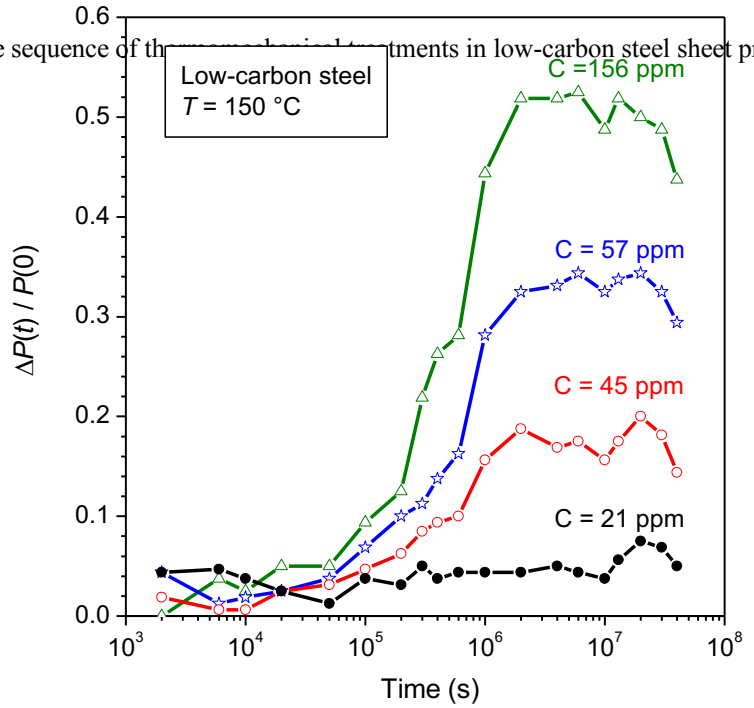

Fig. 11- Relative increase $\Delta P(t)/P(0)$ of power losses (f = 50 Hz, J_p = 1.5 T) with aging time t at T = 150 °C in low-carbon steel sheets (Si = 0.3 wt%) having C concentration (weight ppm) ranging between 21 ppm and 156 ppm. Adapted from Ref. [33].

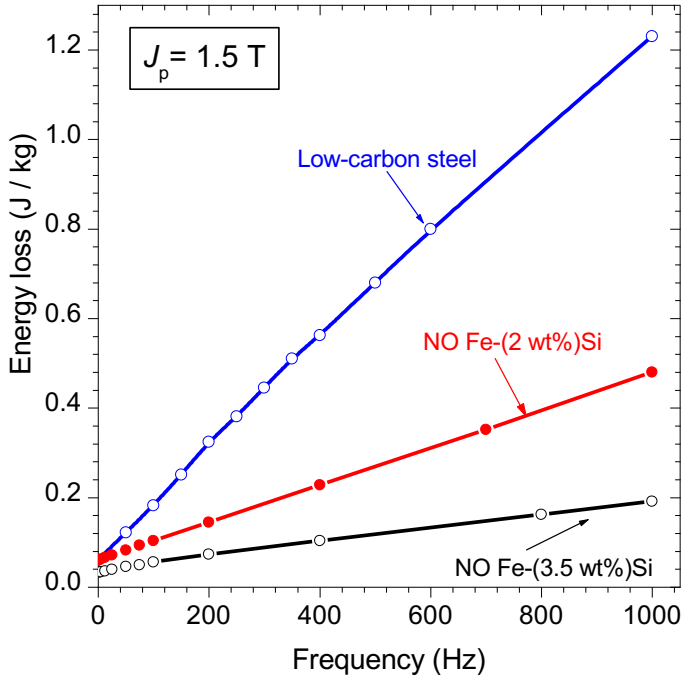

Fig. 12 - Specific power loss versus magnetizing frequency at peak polarization value J_p = 1.5 T in different types of commercial soft magnetic sheets: 1) 0.65 mm thick low-carbon steel; 2) 0.50 mm thick non-oriented Fe-(2 wt%) Si; 3) 0.35 mm thick non-oriented Fe-(3.5 wt%) Si.

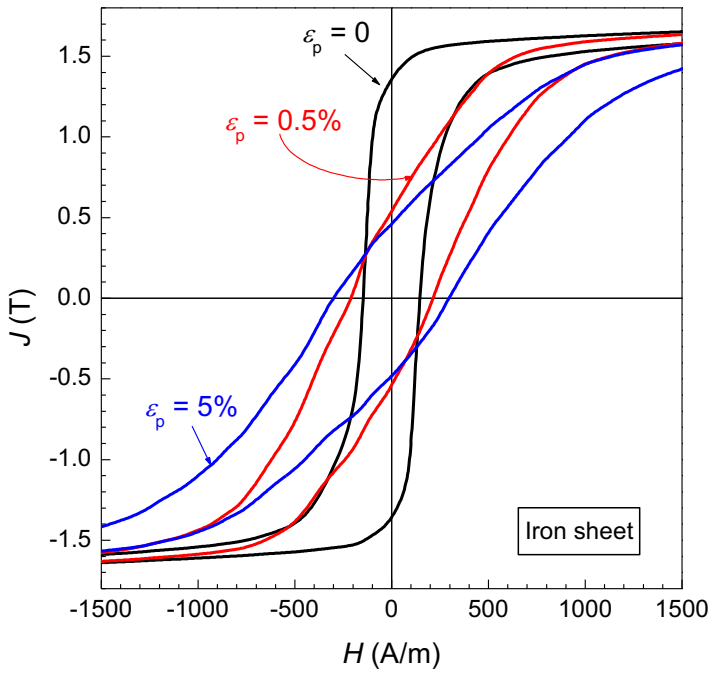

Fig. 13 - Evolution of DC major hysteresis loop (J_p = 1.5 T) in cold-rolled and recrystallized Fe sheets (average grain size $\langle s \rangle$ = 14 μm) with plastic deformation by tensile straining up to ε_p = 5 %.

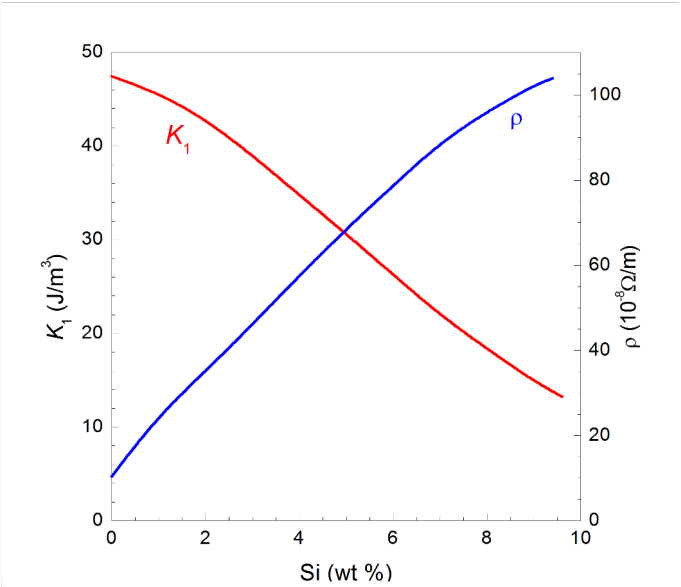

Fig. 14 – Magnetocrystalline anisotropy constant K_1, electrical resistivity ρ, saturation magnetic polarization J_s, and yield stress σ_y versus Si concentration in the Fe-Si alloys. These behaviors summarize data taken from different literature sources [39]

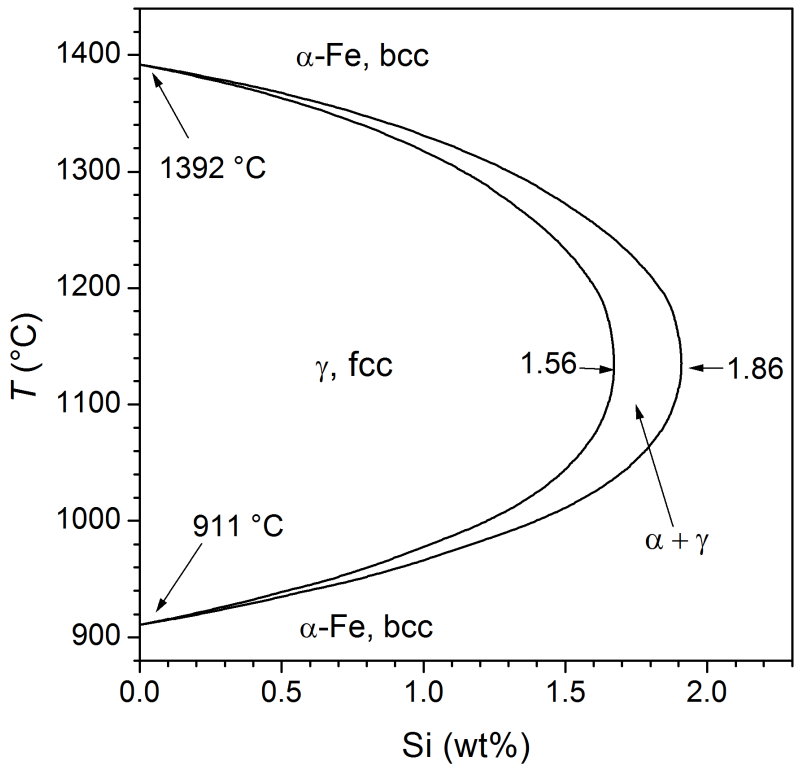

Fig. 15 – Fe-Si phase diagram: the γ loop. For Si concentrations exceeding 1.86 wt% and negligible C concentrations, the $\alpha \rightarrow \gamma$ transformation does not take place and there is freedom in the thermomechanical treatments. The width of the region where the α (bcc) and γ (fcc) phases coexist increases with the C content.

- Composition [wt%]: Si (0.9…3.7), Al (0.2…0.8), Mn (0.1…0.3).
- Melting, degassing, continuous casting of slabs.
- Re-heating (1000 °C – 1250 °C) and hot rolling to thickness 1.8 mm - 2.3 mm.
- Pickling and cold rolling to intermediate gauge.
- Intermediate annealing (750 °C – 900 °C).
- Cold rolling to final gauge (0.65 mm – 0.35 mm).
- Decarburization and re-crystallization annealing (830 °C – 900 °C).
- Final grain-growth annealing (850 °C – 1100°C).
- Coating.

Table 5 – Preparation stages of fully processed non-oriented Fe-Si laminations.

Grade	Sheet thickness (mm)	Maximum specific loss at 1.0 T (W/kg)	
		f = 400 Hz	f = 2.5 kHz
NO27	0.27	15.0	300
NO20	0.20	15.0	215
NO18	0.178	14.3	179
NO12	0.127	13.5	152
NO10	0.10	13.0	135

Table 6 – Industrial non-oriented fully processed electrical steel sheets with reduced thickness (Cogent Steels).

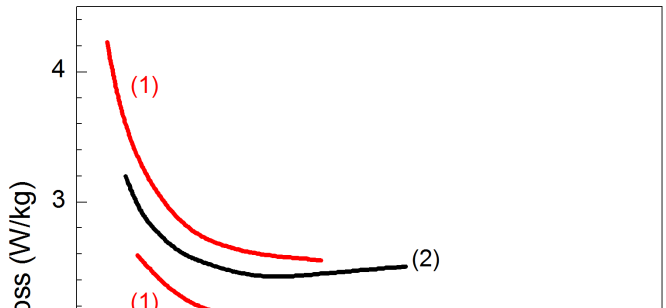

Fig. 16 – Power loss at 50 Hz versus average grain size measured in NO Fe-Si steel sheets. (1) Two different types of 0.35 mm thick sheets with Si 3 wt % + Al 0.4 wt % [44]; (2) 0.50 mm thick sheet with Si 3 wt% + Al 1 wt% [45].

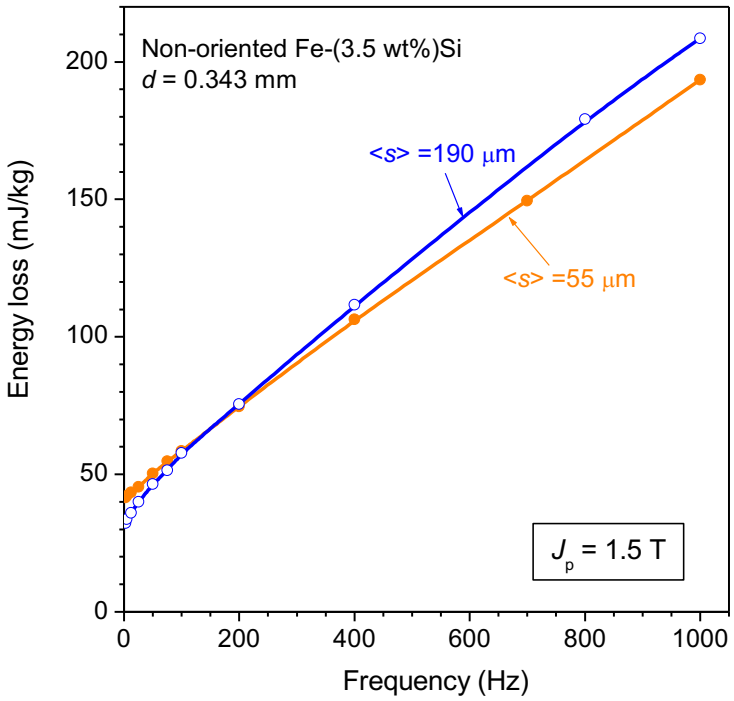

Fig. 17 - Energy loss per cycle versus magnetizing frequency in 0.343 mm thick non-oriented fully processed Fe-Si sheets. With increasing grain size $\langle s \rangle$, the energy loss decreases in the lower frequency range (up to a few hundred Hz) and increases at higher frequencies. This behavior highlights the role of the excess loss component W_{exc}, which increases as $\langle s \rangle^{1/2}$ [44].

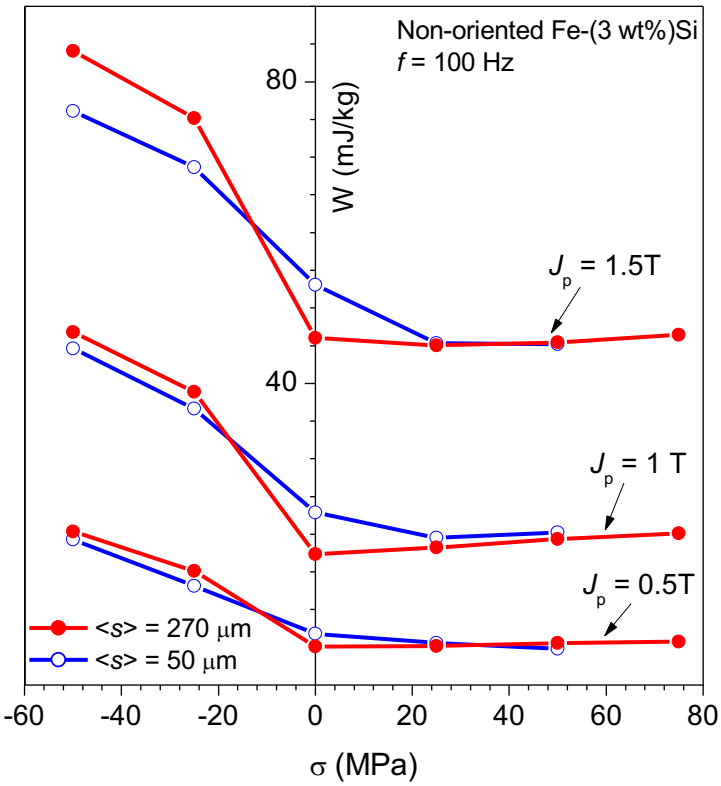

Fig. 18 – Specific energy loss measured at 100 Hz and different values of the peak polarization J_p in non-oriented Fe-(3 wt%)Si sheets (thickness 0.34 mm) under various applied tensile (positive)/compressive (negative) stresses. Open symbols: average grain size $\langle s \rangle$ = 50 μm. Full symbols: $\langle s \rangle$ = 270 μm. (Adapted from Ref. [49]).

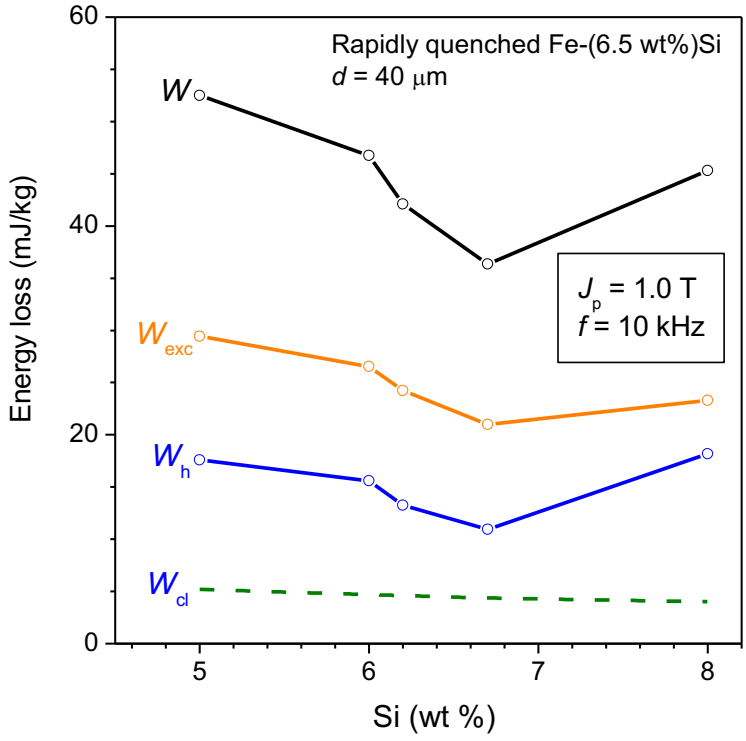

Fig. 19 – Energy loss W at 10 kHz and J_p = 1.0 T in a rapidly quenched high-Si ribbon (thickness d = 40 μm, average grain size $\langle s \rangle$ = 150 μm) and its components (hysteresis W_h, excess W_{exc}, and classical W_{cl}) as a function of the Si concentration (Adapted from Ref. [51]).

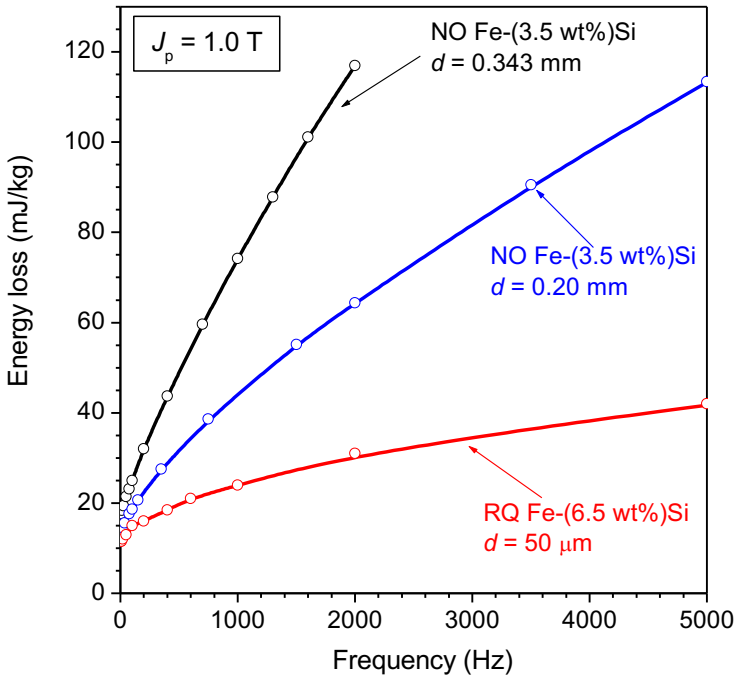

Fig. 20 – Energy loss versus frequency in conventional non-oriented Fe-Si sheets and in rapidly quenched (RQ) high-Si ribbons (peak polarization J_p = 1.0 T). 1) Fe-(3.5 wt%)Si, thickness d = 0.343 mm; 2) Fe-(3.5 wt%)Si, thickness d = 0.20 mm; 3) RQ Fe-(6.5 wt %)Si ribbon, thickness d = 50 μm.

	d (mm)	μ_{max}	J_s (T)	B_8 (T)	B_{25} (T)	$P_{10/50}$ (W/kg)	$P_{10/400}$ (W/kg)	$P_{10/1k}$ (W/kg)	$P_{5/2k}$ (W/kg)	$P_{1/10k}$ (W/kg)
Fe-(6.5 wt%)Si JNHF	0.10 0.20	$0.41 \cdot 10^4$ $0.39 \cdot 10^4$	1.88 1.94	1.15 1.09	1.44 1.47	1.1 1.2	10.1 14.5	30.0 51.6	11.5 17.9	7.1 12.7
Fe-(6.5 wt%)Si JNEX	0.10	$2.3 \cdot 10^4$	1.80	1.29	1.40	0.5	5.7	18.7	11.3	8.3
GO	0.10	$2.4 \cdot 10^4$	2.03	1.84	1.91	0.7	6.0	22.7	22.0	18.0
NO	0.345	$1.2 \cdot 10^4$	1.99	1.44	1.55	0.87	17.6	76.0	59.0	53.2
Amorphous	0.025	$30 \cdot 10^4$	1.55	1.54	1.55	0.1	1.5	5.5	8.1	3.6

Table 7 – Magnetic parameters in different magnetic steel sheets and in a typical Fe-based amorphous alloy. 1) JFE CVD-treated Fe-Si with Si concentration gradient (JNHF); 2) JFE CVD treated Fe-(6.5 wt%Si) (JNEX); 3) Thinned GO sheets; 4) NO fully processed sheets; 5) Fe-based amorphous ribbons. $d \equiv$ sheet thickness; $\mu_{max} \equiv$ DC relative maximum permeability; $J_s \equiv$ saturation polarization; $B_8 \equiv$ induction at 800 A/m; $B_{25} \equiv$ induction at 2500 A/m; $P_{10/50} \equiv$ specific power loss at $J = 1$ T and $f = 50$ Hz; $P_{10/400} \equiv$ specific power loss at $J = 1$ T and $f = 400$ Hz; $P_{10/1k} \equiv$ specific power loss at $J = 1$ T and $f = 1$ kHz; $P_{5/2k} \equiv$ specific power loss at $J = 0.5$ T and $f = 2$kHz; $P_{1/10k} \equiv$ specific power loss at $J = 0.1$ T and $f = 10$ kHz.

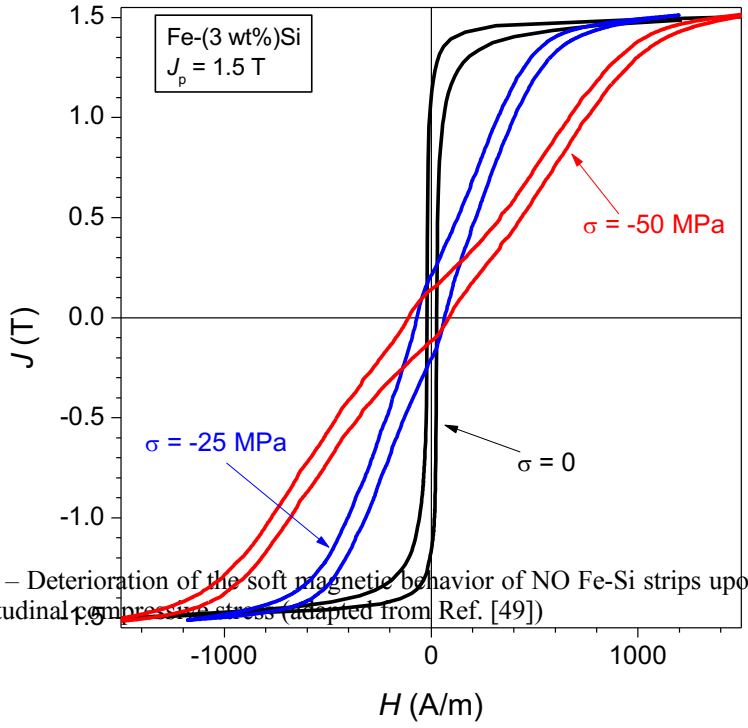

Fig. 21 – Deterioration of the soft magnetic behavior of NO Fe-Si strips upon application of a longitudinal compressive stress (adapted from Ref. [49])

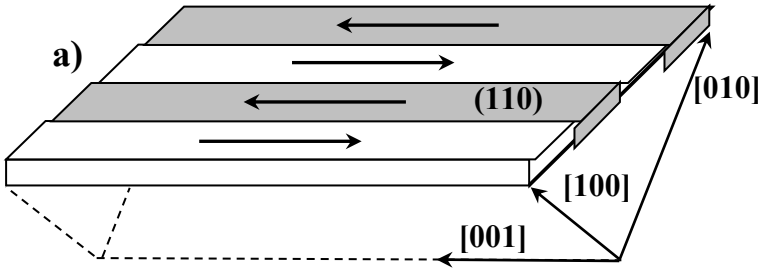
a)
(110)
[010]
[100]
[001]

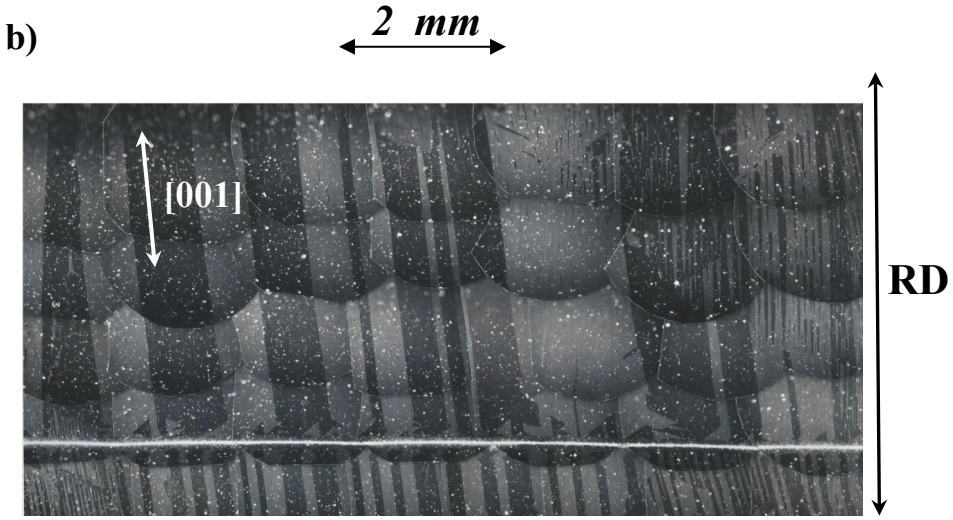
b)
2 mm
[001]
RD

Type	Grade	Thickness (mm)	Specific power loss J_p=1.7 T, f=50 Hz (W/kg)	Polarization at H = 800 A/m (T)
CGO	M140-35S	0.35	1.40	1.82
CGO	M130-30S	0.30	1.30	1.83
CGO	M121-27S	0.27	1.21	1.84
CGO	M115-23S	0.23	1.15	1.84
CGO	M090-20S	0.20	0.90	1.86
CGO	M082-20S	0.20	0.82	1.84
HGO	M106-30P	0.30	1.06	1.91
HGO	M099-27P	0.27	0.99	1.92
HGO	M092-23P	0.23	0.92	1.92
HGO	M080-23P (laser scribed)	0.23	0.80	1.90

Table 8 – Specifications for conventional (CGO) and high-permeability (HGO) grain-oriented Fe-(3 wt%)Si sheets.

Fig. 22 – (a) A well oriented crystal in a grain-oriented Fe-Si sheet displays a bar-like domain structure, with the magnetization oriented along the [001] axis and lying in the (110) plane. (b) Magnetooptical Kerr observations show that flux-closure domains appear at the grain boundaries and spike structures are formed when the sheet plane slightly deviates from the ideal (110) orientation (RD ≡ rolling direction). The density of the main domains can be increased by means of surface scribing (bottom of the micrograph).

	CGO	**HGO**
Composition (wt%)	3.0….3.2 Si 0.004…0.1 Mn 0.02 S 0.03 C balance Fe	2.9…3.3 Si 0.03 Al 0.07 Mn 0.03 S 0.015 N 0.05-0.07 C balance Fe
Inhibitors	MnS	MnS + AlN
Melting, degassing and continuous casting of slabs		
Re-heating and hot-rolling	T = 1320 °C	T = 1360 °C
Annealing	T = 900…1000 °C	T = 1100- 1150 °C
Cold-reduction	70 %	87 %
Annealing	800….1000 °C	------
Cold-reduction	55 %	------
Decarburization	800…..850 °C (wet H_2 atmosphere)	
MgO coating and coiling		
Box annealing (secondary recrystallization), T = 1200 °C		
Phosphate coating and thermal flattening		

Table 9 - Summary of the industrial preparation process of grain-oriented silicon steel sheets. CGO denotes the conventional grain-oriented steels. HGO refers to the high permeability steels, of which a standard preparation method is presented. The CGO process adopts a two-stage cold reduction, while with HGO the final gauge is reached in a single step. The inhibitors are the MnS precipitates and MnS + AlN particles for CGO and HGO, respectively.

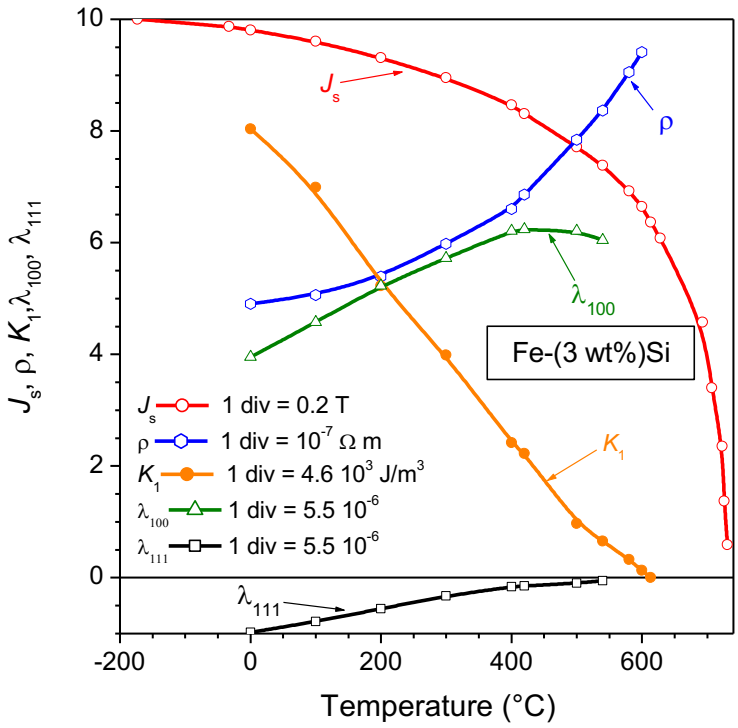

Fig. 23 – Temperature dependence of electrical resistivity and the intrinsic magnetic parameters in Fe-(3 wt%)Si (reduced units). J_s ≡ saturation polarization; ρ ≡ electrical resistivity; K_1 ≡ anisotropy constant; λ_{100}, λ_{111} ≡ saturation magnetostriction constants (Adapted from Refs. [68] [69])

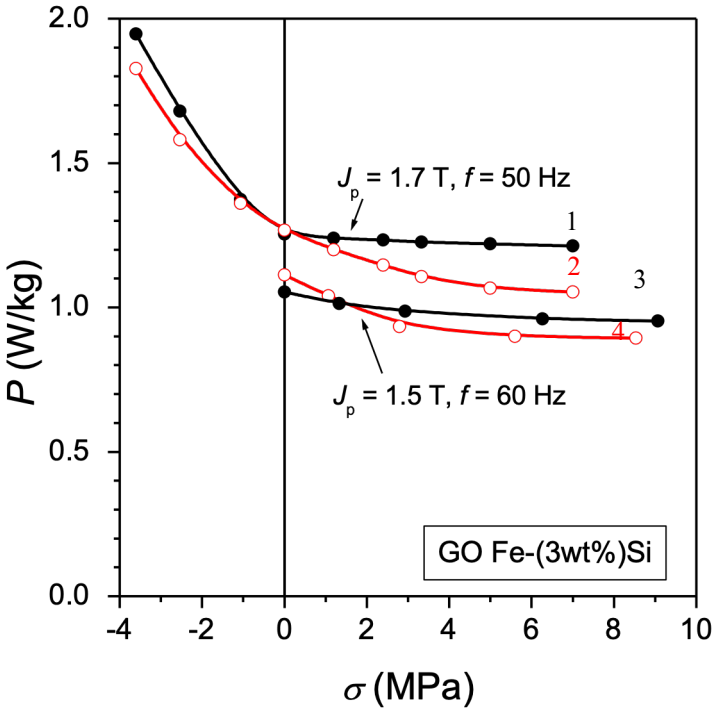
2.0
1.5
1.0
0.5
0.0
P (W/kg)
-4
-2
0
2
4
6
8
10
σ (MPa)
J_p = 1.7 T, f = 50 Hz
J_p = 1.5 T, f = 60 Hz
1
2
3
4
GO Fe-(3wt%)Si

Fig. 24 – Stress dependence of the power loss in CGO (solid symbols) and HGO (open symbols) Fe-(3 wt%)Si at J_p = 1.7 T (f = 50 Hz) and J_p = 1.5 T (f = 60 Hz). 1&2: thickness d = 0.30mm; 3: d = 0.27 mm; 4: d = 0.29 mm (from Refs. [70] [71]).

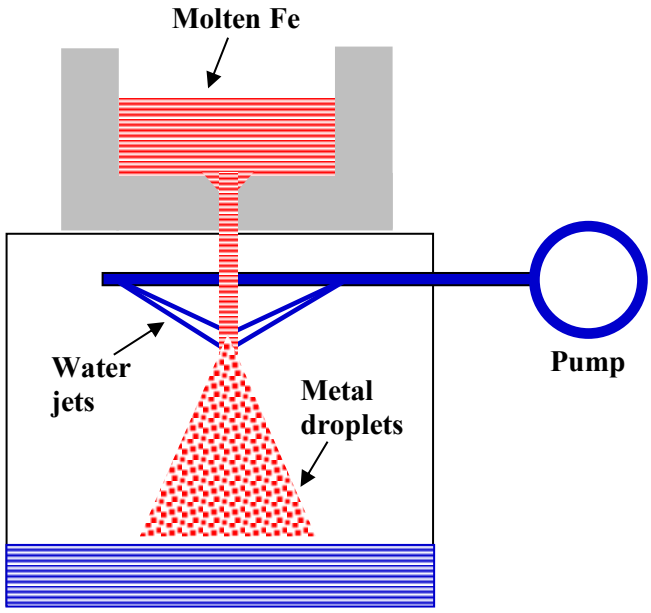

Fig. 25 - Production of particles by the atomization process. The molten Fe, pouring from the crucible, is invested by a jet of pressurized water and solidification occurs by formation of particles of approximately spherical shape.

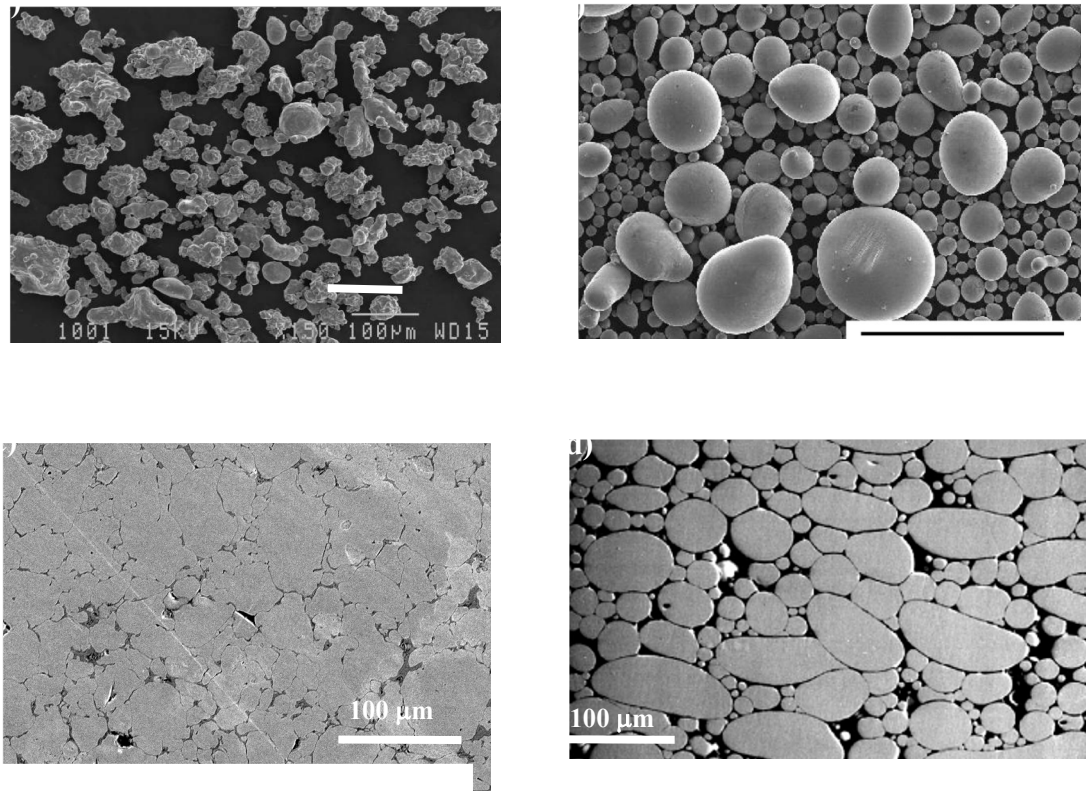

Fig. 26 – a) Iron powder obtained by the water atomisation process [73]; b) $Fe_{81}(Si_{0.3}B_{0.7})_{17}C_2$ amorphous particles obtained by the Spinning Water Atomization Process (SWAP) [77]; c) Cross-sectional view of a composite obtained after powder mixing, compaction, and curing at a temperature ranging between, 150 °C and 500 °C [80]); d) Cross-sectional view of the consolidated amorphous powder with glass binder [81]).

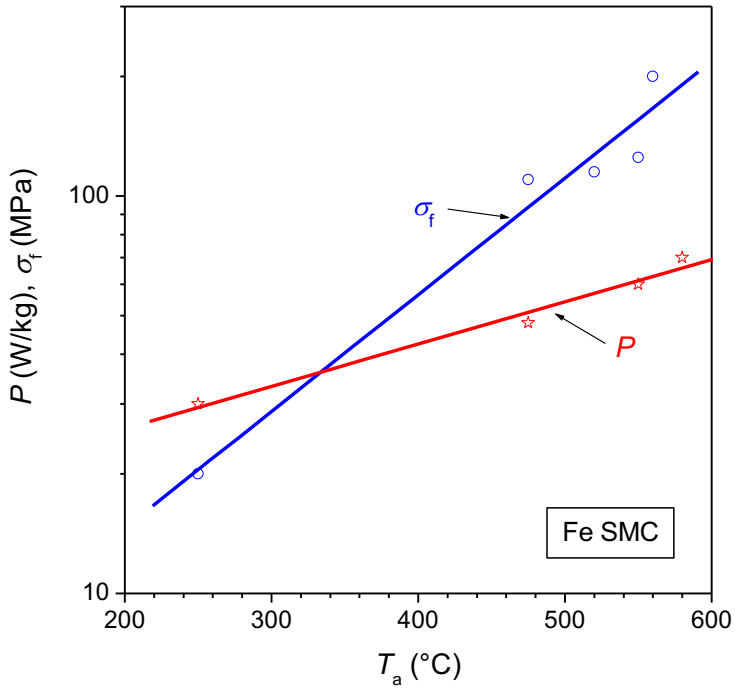

Fig. 27 – Transverse fracture stress σ_f and power loss P at J_p = 1.5 T and f = 100 Hz as a function of annealing temperature T_a in compacted Fe-composites (from Ref. [83].

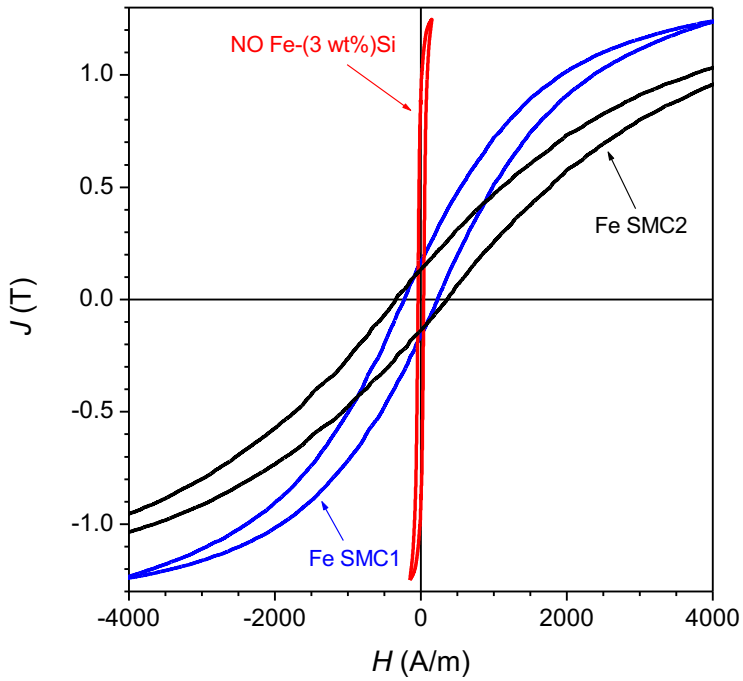

Fig. 28 – DC hysteresis loops taken at peak polarization J_p = 1.5 T in: 1) Non-oriented 0.35 mm thick Fe-(3 wt%)Si sheet; 2) Fe-based composite SMC1, with density δ = 7450 kg/m^3 and average particle size $\langle s \rangle$ = 114 μm; 3) Fe-based composite SMC2, with density δ = 7260 kg/m^3 and average particle size $\langle s \rangle$ = 29.5 μm.

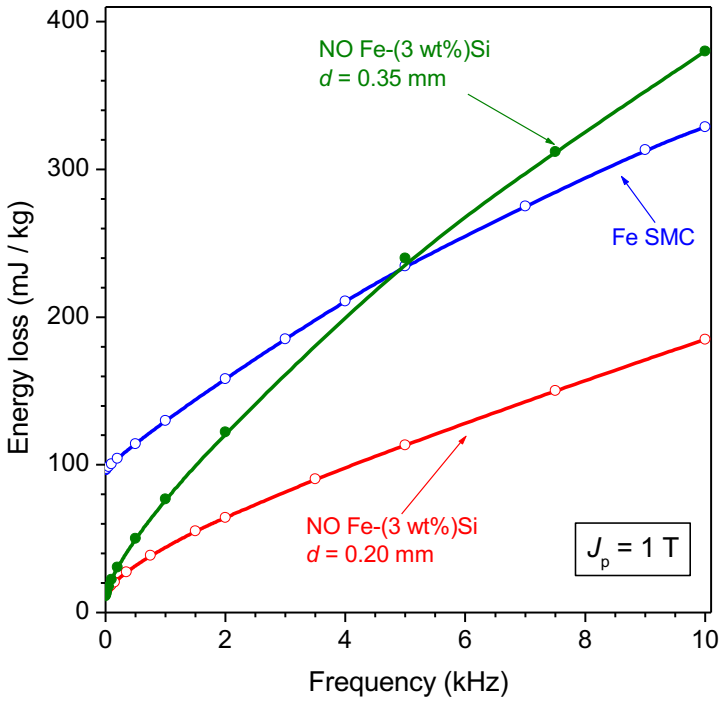

Fig. 29 – The energy loss versus frequency at J_p = 1.0 T in a high-density (δ = 7450 kg/m^3) bonded Fe SMC sample is compared with the loss measured in 0.35 mm thick and 0.20mm thick non-oriented Fe-(3 wt%)Si sheets.

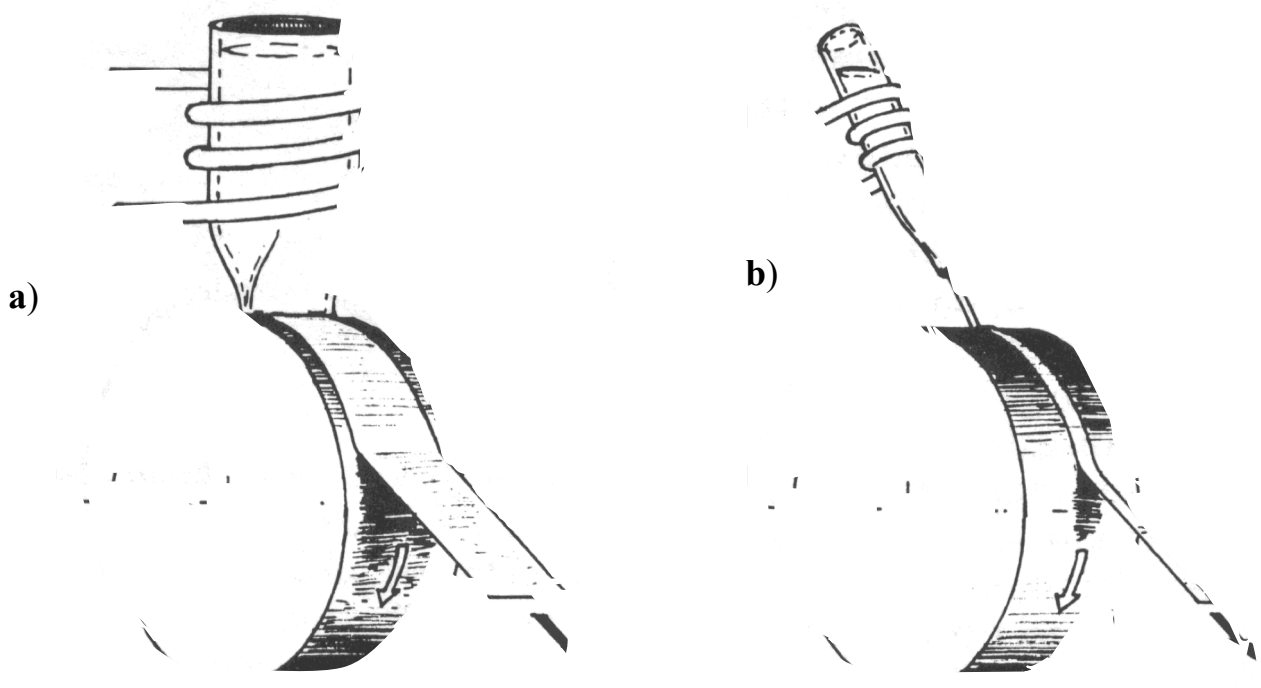

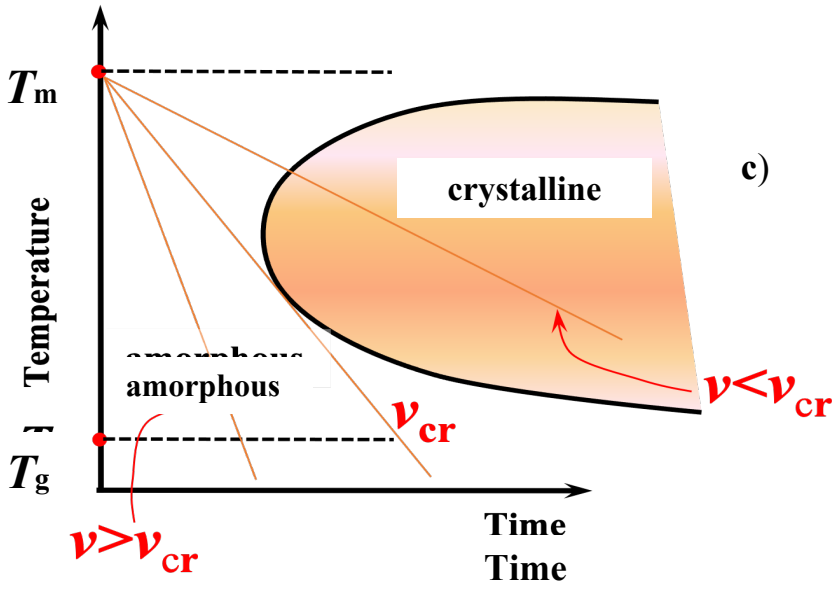

Fig. 30 – Preparation of soft magnetic ribbons by means of rapid quenching from the melt by (a) Planar Flow Casting and (b) Chill Block Melt Spinning. The peripheral velocity of the metallic wheel (e.g. copper, iron, steel) typically ranges between 10 m/s and 40 m/s. Casting can be performed either in air, inert gas or vacuum. c) Time-Temperature-Transformation (TTT) diagram. For cooling rates $v = dT/dt$ larger than a critical value $v_{cr} \sim 10^5$ °C/s, the liquid structure is retained, starting from the melting temperature T_m, down to the glass transition temperature T_g, where it achieves the viscosity of the solid state.

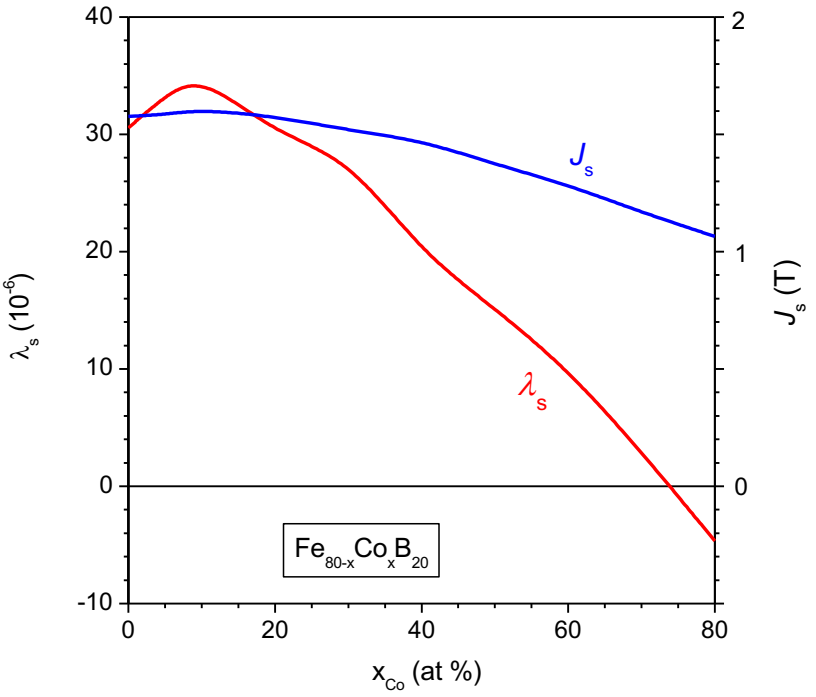

Fig. 31 – Saturation polarisation J_s and saturation magnetostriction constant λ_s versus Co atomic concentration in $Fe_{80-x}Co_xB_{20}$ amorphous alloys. Zero magnetostriction is attained for Co concentration $x_{Co} \sim 75$ at% [96].

	Amorphous ribbon $Fe_{78}B_{13}Si_9$ (thickness 0.025 mm)	*GO Fe-(3 wt%)Si (thickness 0.23 mm)*
Density (kg/m^3)	$7.18 \cdot 10^3$	$7.65 \cdot 10^3$
Young modulus (GPa)	150	120
Yield stress (MPa)	> 700	< 300
Fracture stress (MPa)	2800	350
Fracture strain (%)	2.5	25
Vicker's hardness	800	180
Electrical resistivity (Ω·m)	$137 \cdot 10^{-8}$	$45 \cdot 10^{-8}$
Lamination factor (%)	< 90	95
Curie temperature (°C)	415	740
Saturation polarization (T)	1.56	2.03
Saturation magnetostriction (λ_{100})	$37 \cdot 10^{-6}$	$25 \cdot 10^{-6}$
dc coercive field (A/m)	2 (after annealing)	5
Max relative permeability	$2 \cdot 10^5$ (after annealing)	$8 \cdot 10^4$
50 Hz power loss at 1.4 T (W/kg)	0.25 (after annealing)	0.70

Table 10 - Physical and magnetic properties of $Fe_{78}B_{13}Si_9$ amorphous alloys and grain-oriented Fe-(3wt%)Si steel sheets.

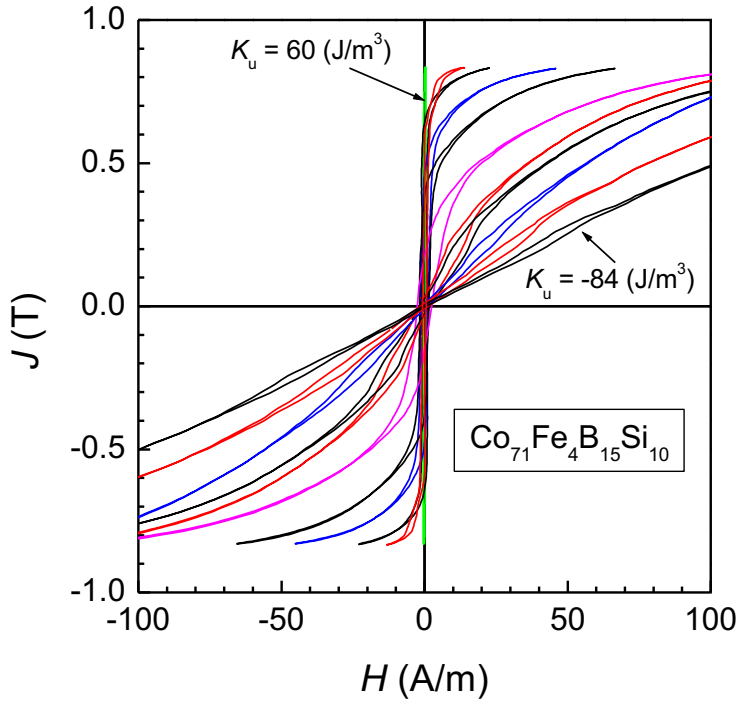

Fig. 32 – Evolution of the DC hysteresis loops in near-zero magnetostriction Co-based amorphous ribbons with magnetic anisotropy K_u induced by annealing under saturating magnetic field. Starting from the near-rectangular loop ($K_u > 0$) obtained by annealing under longitudinal field, progressive tilting and linearization of the loop is observed upon a sequence of transverse field treatments with increasing times and temperatures, which lead to increasing transverse induced anisotropy ($K_u < 0$).

Alloy	J_s **(T)**	T_c **(°C)**	T_x **(°C)**	ρ **(10^{-8} Ωm)**	λ_s **(10^{-6})**	H_c **(A/m)**
$Fe_{80}B_{20}$	1.60	375	450	122	32	3
$Fe_{78}B_{13}Si_9$	1.56	415	550	137	37	2.4
$Fe_{81}B_{13.5}Si_{3.5}C_2$	1.61	370	480	135	30	3.2
$Co_{80}B_{10}Si_{10}$	0.90	520	410	108	-4	7
$Co_{71}Fe_4B_{15}Si_{10}$	0.87	352	520	124	-0.2	0.5
$(Co,Fe)_{70}(Mo,Si,B)_{30}$	0.55	250	500	130	-0.2	0.4

Table 11 - Physical parameters of representative amorphous alloys. J_s ≡ saturation polarisation; T_c ≡ Curie temperature; T_x ≡ crystallization temperature; ρ ≡ electrical resistivity; λ_s ≡ saturation magnetostriction constant; H_c ≡ coercive field. The data refer to materials subjected to thermomagnetic treatments leading to optimization of the magnetic properties.

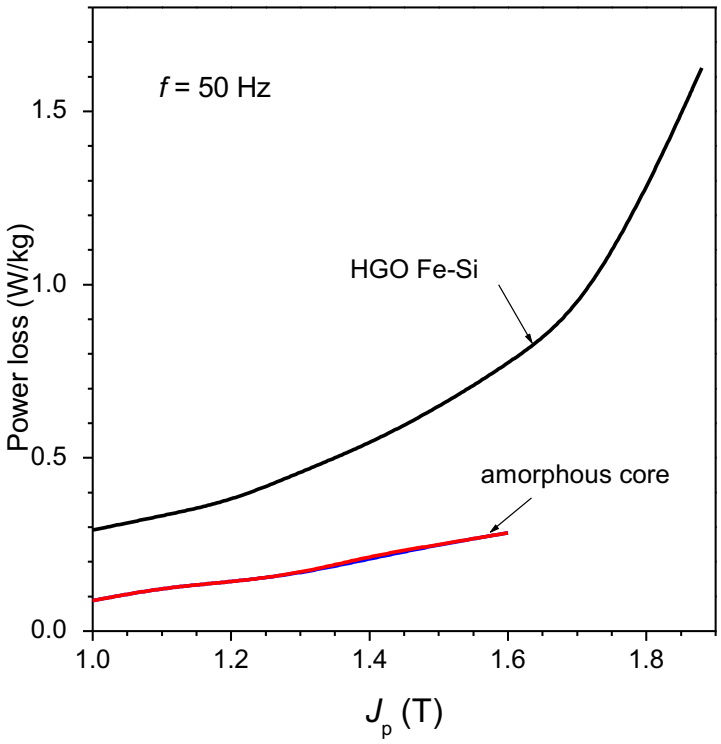

Fig. 33 - Power losses at 50 Hz versus polarization level in high-permeability grain-oriented Fe-Si alloys and Fe-based amorphous alloys (from Ref. [98])

Transformer parameters	Metglas® HB1 amorphous alloy	Metglas® SA1 amorphous alloy	HGO Fe-Si
Mass ratio	1.17	1.23	1
No-load loss (W)	215	215	665
Total loss at 40% load(W)	1207	1207	1353
Audible noise (dB)	55	58	53

Table 12 – Parameters in a 500 kVA three-phase transformer unit with different core materials [98].

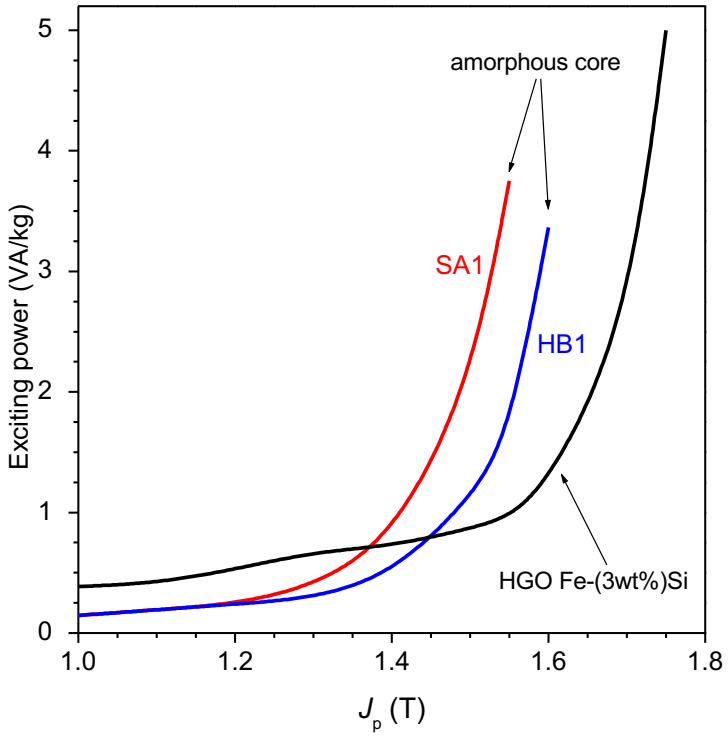

Fig. 34 - Exciting power at 50 Hz versus peak polarization in the amorphous and Fe-Si transformer cores of Table 12 (from Ref. [98])

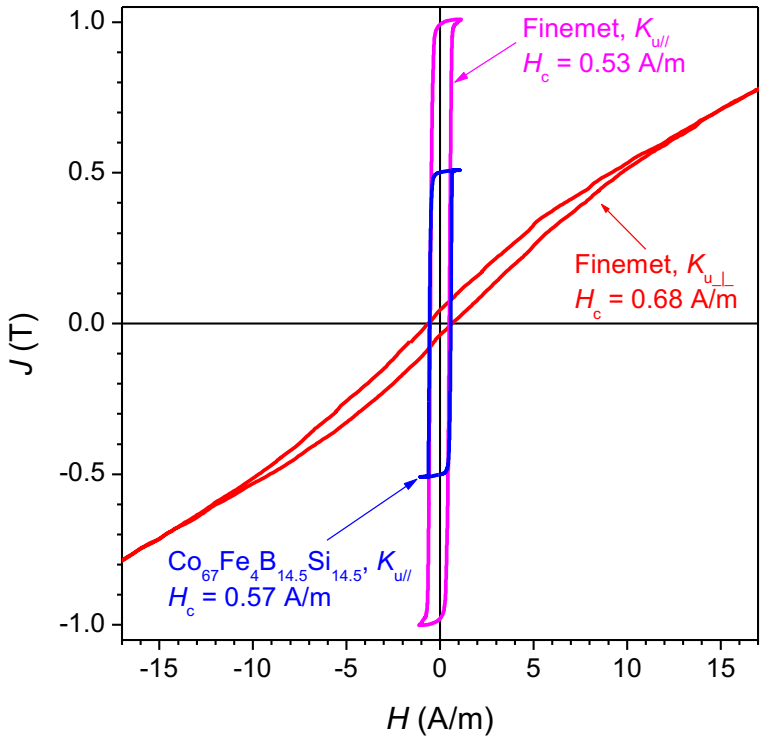

Fig. 35 – Quasi-static hysteresis loops in Co-based amorphous and in nanocrystalline $Fe_{73.5}Cu_1Nb_3B_9Si_{13.5}$ alloys (tapewound toroidal cores). The amorphous sample is stress-relaxed at 360 °C and annealed under longitudinal saturating magnetic field at 280 °C (induced anisotropy $K_{u//}$). The nanocrystalline ring is subjected to crystallization annealing at 550 °C and slow cooling under either longitudinal ($K_{u//}$) or transverse ($K_{u\_|\_}$) saturating field, thereby passing from near-rectangular to near-linear hysteresis loop.

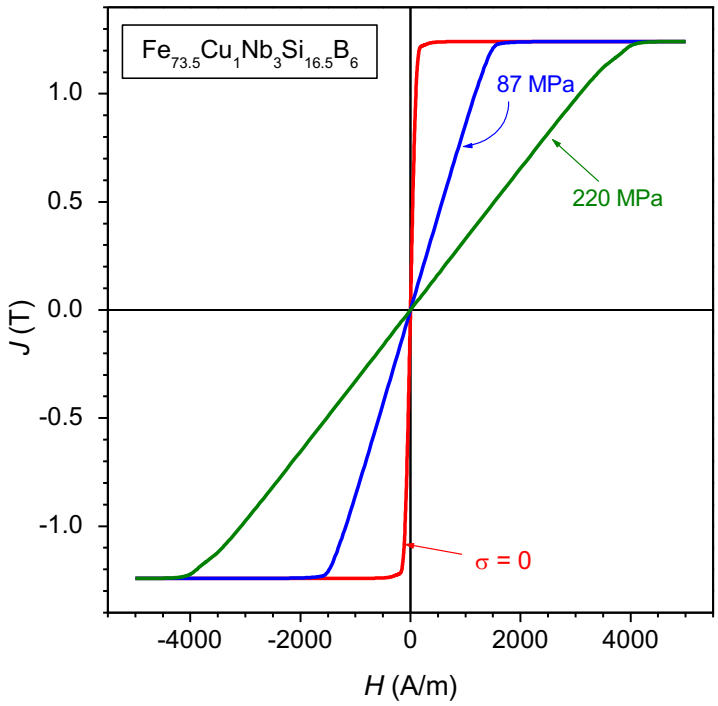

Fig. 36 – Quasi-static hysteresis loops in nanocrystalline $Fe_{73.5}Cu_1Nb_3Si_{16.5}B_6$ alloys, annealed 1 hour at 540 °C under applied tensile stress σ (from G. Herzer [116]). For σ = 220 MPa, the anisotropy induced transverse to the ribbon axis is $K_u \approx -2400$ J/m^3.

Alloy	J_s **(T)**	λ_s **(10^{-6})**	H_c **(A/m)**	μ_i	ρ **(10^{-8} Ωm)**	$\langle s \rangle$ **(nm)**
$Fe_{73.5}Cu_1Nb_3Si_{13.5}B_9$	1.24	2.1	0.5	$1 \cdot 10^5$	32	13
$Fe_{73.5}Cu_1Nb_3Si_{15.5}B_7$	1.23	~ 0	0.4	$1.1 \cdot 10^5$	32	14
$Fe_{84}Nb_7B_9$.	1.49	0.1	8	$2.2 \cdot 10^4$	30	9
$Fe_{86}Cu_1Zr_7B_6$	1.52	~ 0	3	$4.8 \cdot 10^4$	-4	10
$Fe_{91}Zr_7B_2$	1.63	-1.1	6	$2.2 \cdot 10^4$	-4	17

Table 13 - Physical and magnetic parameters of representative nanocrystalline alloys. $J_s \equiv$ saturation polarisation; $\lambda_s \equiv$ saturation magnetostriction constant; $H_c \equiv$ coercive field; $\mu_i \equiv$ quasi-static initial permeability; $\langle s \rangle \equiv$ average grain size; $\rho \equiv$ electrical resistivity (from Ref. [16]).

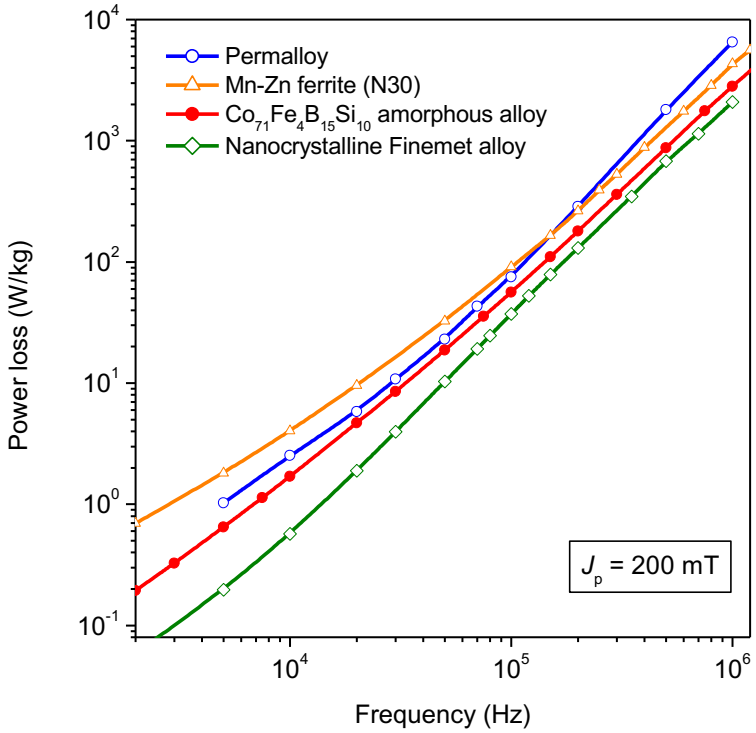

Fig. 37 – The power loss at peak polarization J_p = 0.2 T and intermediate frequencies of 20 μm thick nanocrystalline $Fe_{73.5}Cu_1Nb_3B_9Si_{13.5}$ ribbons annealed under saturating transverse magnetic field is compared with the same quantity measured in Co-based amorphous ribbons and Fe-Ni tapes of Permalloy type of comparable thickness, and in a commercial Mn-Zn ferrite. Note that if the loss per unit volume instead of unit mass is represented, the shown loss figures must be accordingly readjusted, but the overall advantage of the nanocrystalline ribbons persists.

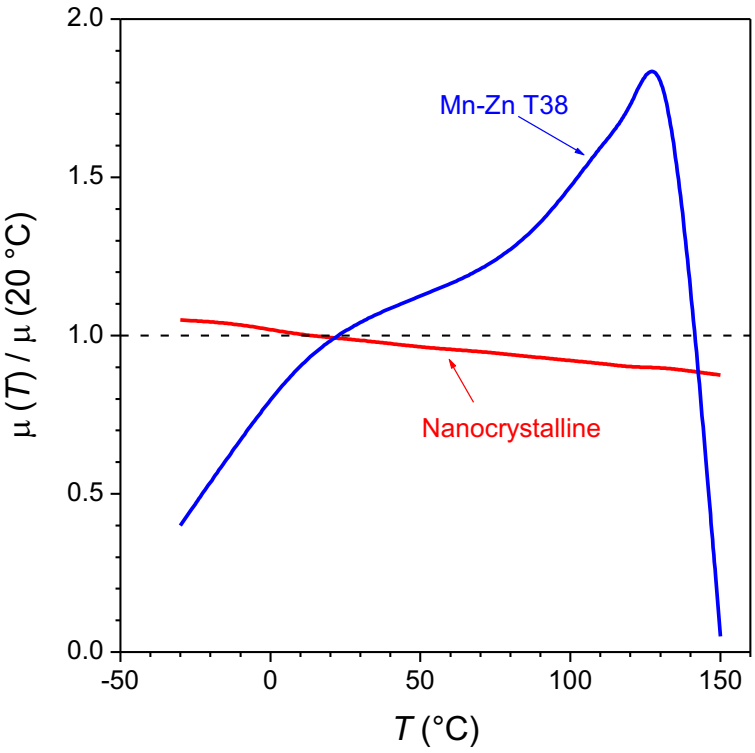

Fig. 38 – Variation of the initial permeability with temperature relative to $T = 20$ °C in a Mn-Zn ferrite (T38) and in a nanocrystalline core [118].

Type	Saturation polarization (T)	Max DC permeability	Saturation magnetostriction (ppm)	Electrical resistivity (Ω·m)	Curie temperature (°C)
2605SA1 (Fe-based)	1.56	10^5	27	$130 \cdot 10^{-8}$	400
2605S3A (Fe-based)	1.41	$35 \cdot 10^3$	20	$138 \cdot 10^{-8}$	358
2705M (Co-based)	0.77	$6 \cdot 10^5$	< 0.5	$136 \cdot 10^{-8}$	365
2714A (Co-based)	0.57	10^6	< 0.5	$142 \cdot 10^{-8}$	225

Type	Density (kg/m^3)	Vickers hardness	Tensile strength (GPa)	Crystallization temperature (°C)	Lamination factor (%)	Continuous service temperature (°C)
2605SA1 (Fe-based)	7180	900	1	508	> 75	150
2605S3A (Fe-based)	7290	860	1	535	> 75	150
2705M (Co-based)	7800	900	1	520	> 75	90
2714A (Co-based)	7590	960	1	550	> 75	90

Table 14 - Physical and magnetic parameters of representative commercial amorphous alloys (METGLAS, Inc.)

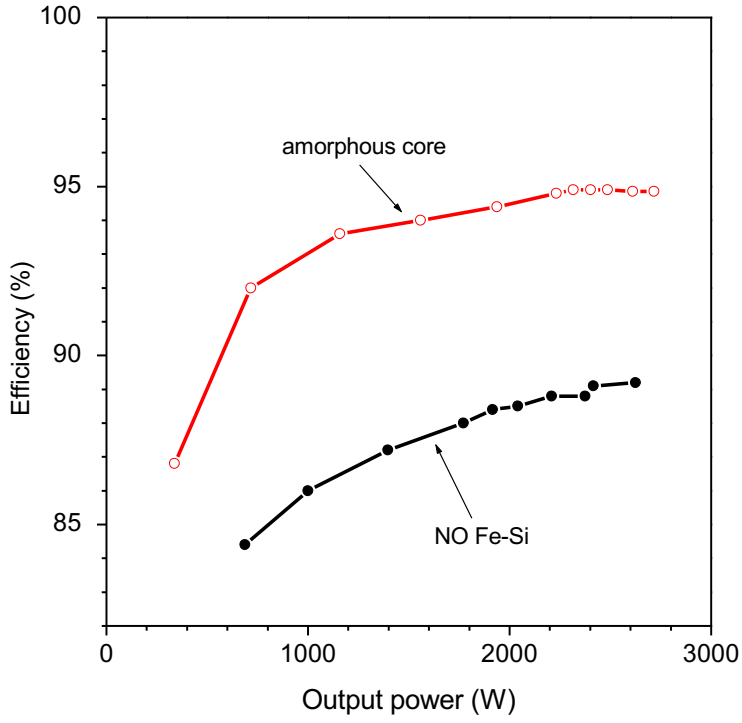

Fig. 39 – Efficiency versus output power in a switched reluctance motor based on an amorphous based alloy and a conventional non-oriented Fe-Si steel [124].

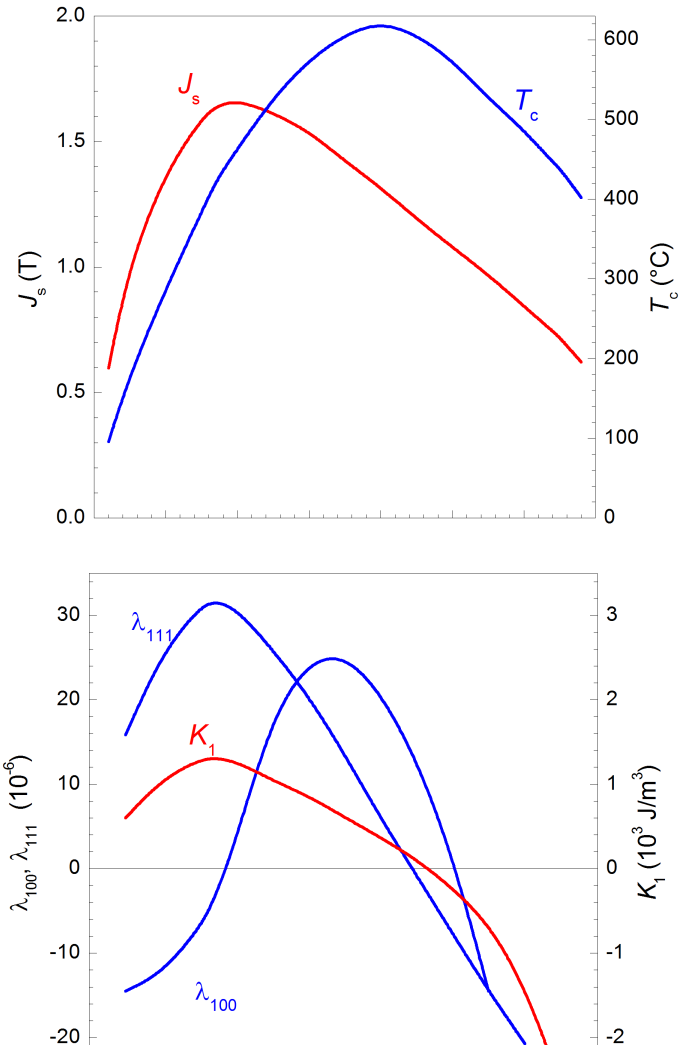

Fig. 40 - Dependence of the magnetic intrinsic parameters on the Ni concentration in Ni-Fe alloys. $J_s \equiv$ saturation polarization; $T_c \equiv$ Curie temperature; $K_1 \equiv$ magnetocrystalline anisotropy constant (random solid solution); λ_{100}, $\lambda_{111} \equiv$ magnetostriction constants. T_c approaches the room temperature for Ni ~ 30 wt% and interesting soft magnetic properties are observed only at higher Ni concentrations. The anisotropy constant depends, besides the composition, on the degree of structural ordering, that is the possible formation of the Ni_3Fe phase. It is consequently related to the annealing temperature and the cooling rate.

Composition (wt%)	J_s **(T)**	T_c **(°C)**	ρ **(10^{-8} Ω·m)**	H_c **(A/m)**	μ_i
$Fe_{64}Ni_{36}$	1.30	230	75	40	2 000
$Fe_{50}Ni_{50}$	1.60	490	45	7	15 000
$Fe_{15}Ni_{80}Mo_5$	0.80	400	60	0.5	150 000
$Fe_{14}Ni_{77}Mo_4Cu_5$	0.78	400	60	1.5	40 000
$Fe_{49}Co_{49}V_2$	2.35	930	40	50	2 000

Table 15 - Properties of some basic Fe-Ni and Fe-Co alloys. $J_s \equiv$ saturation polarization; $T_c \equiv$ Curie temperature; $\rho \equiv$ electrical resistivity; $H_c \equiv$ coercive field; $\mu_i \equiv$ relative initial permeability.

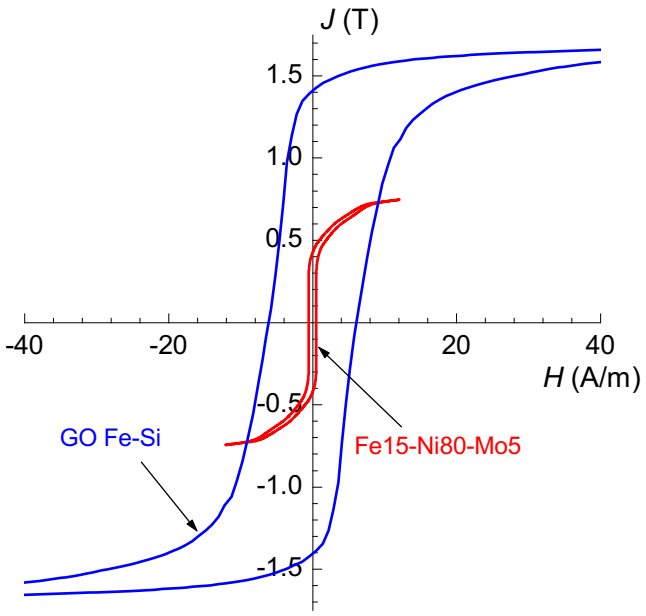

$Fe_{15}Ni_{80}Mo_5$

Fig. 41 - DC hysteresis loops in HGO Fe-(3 wt%)Si laminations and in permalloy ($Fe_{15}Ni_{80}Mo_5$) tapes.

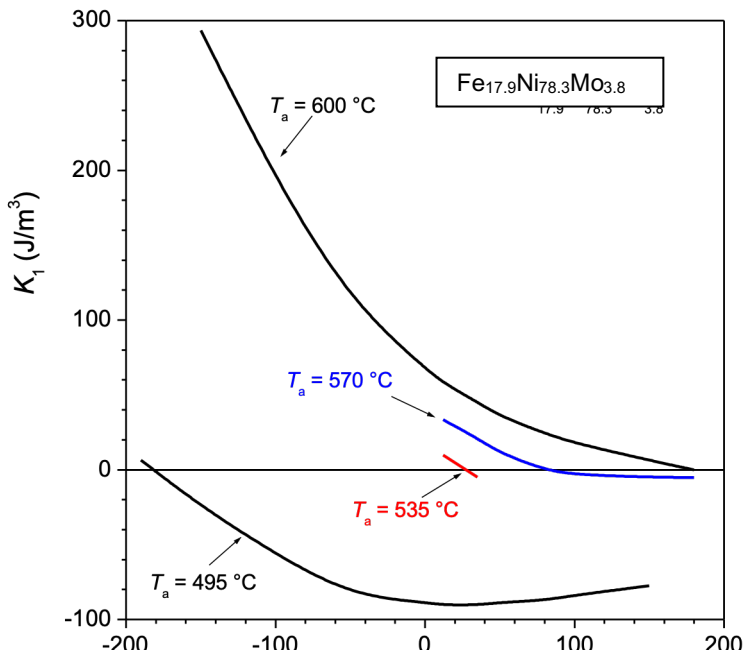

Fig. 42 – Anisotropy constant versus temperature in permalloy-type alloys annealed at different temperatures (T_a) and quenched to room temperature [127].

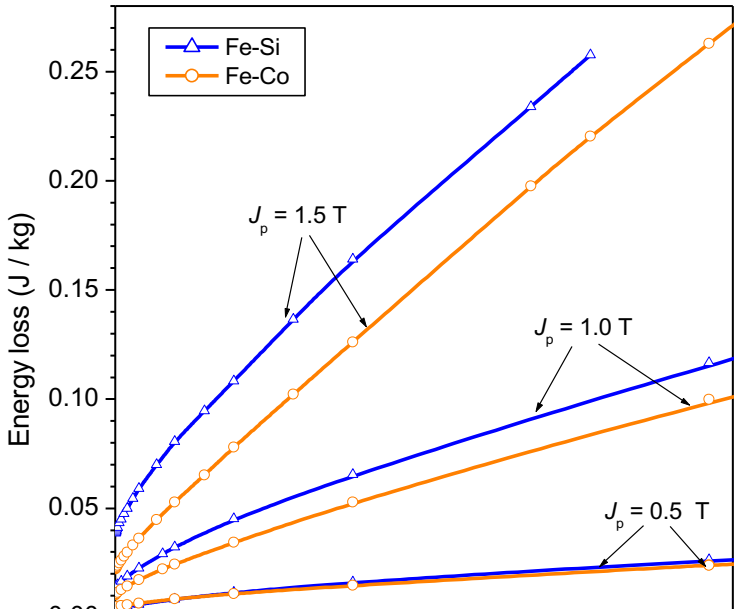

Fig. 43 – Energy loss versus frequency in thin (d = 0.20 mm) Fe-Co and non-oriented Fe-(3 wt%)Si sheets at three different peak polarization values. The Fe-Co alloys (of composition $Fe_{50}Co_{50}V_2$) display increasingly superior performance with respect to the Fe-Si alloys upon increasing J_p value.

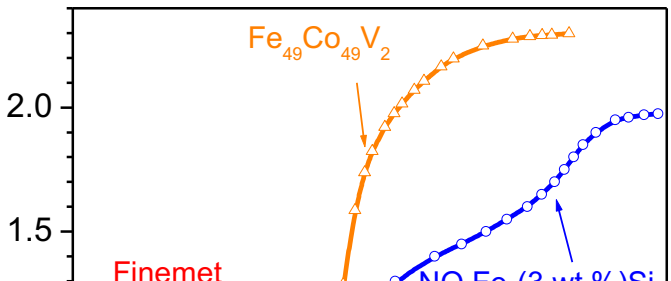

Fig. 44 – Initial magnetization curves of mumetall/permalloy ($(Ni_{80}Fe_{15}Mo_5)$ and permendur ($Fe_{49}Co_{49}V_2$) compared with the curves of nanocrystalline and non-oriented Fe-Si alloys.

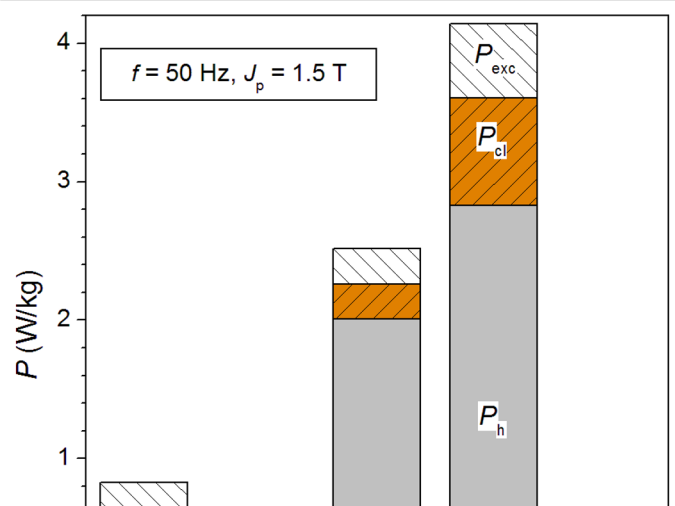

Fig. 45 – Power losses and their decomposition into hysteresis P_h, classical P_{cl}, and excess P_{exc} components at power and medium frequencies and technically significant polarization values J_p in different applicative soft magnetic materials (sinusoidal induction). GO-1: grain-oriented Fe-Si steel sheet, thickness d = 0.29 mm; GO-2: same as GO-1, d = 0.18 mm; NO-1: non-oriented Fe-(3.5 wt%)Si steel sheet, d = 0.35 mm; NO-2: Fe-(2.3 wt%)Si, d = 0.51 mm; NO-3: Fe-(3.5 wt%)Si d = 0.194 mm; Am-1: Fe-based amorphous ribbon, d = 30 μm; Am-2: same as Am-1, d = 23 μm; Fe-Co: $Fe_{49}Co_{49}V_2$ sheet, d = 0.20 mm; SMC: Soft Magnetic Composite; High-Si: Fe-(6.7 wt%)Si rapidly solidified ribbon, d = 40 μm; Ncryst.: nanocrystalline FINEMET ribbon, d = 20 μm.

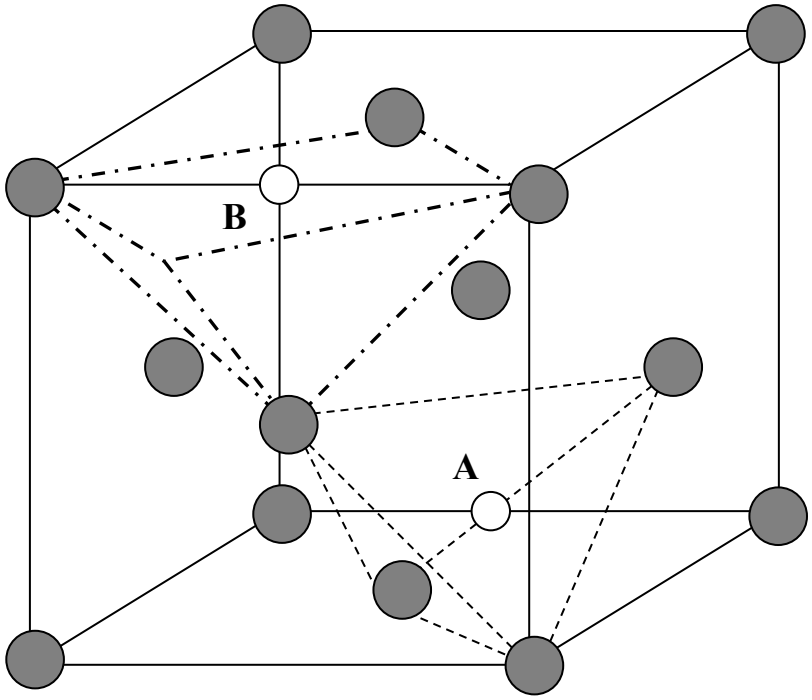

Fig. 46 – Portion (one eighth) of a unit cell of a cubic spinel. The O^{2-} ions (dark) are arranged in an f.c.c. structure. The metal ions (white) are interstitially arranged in tetrahedral (A) and octahedral (B) sites.

Ferrite	Tetrahedral sites A	Octahedral sites B	Bohr magnetons per formula unit
$NiFe_2O_4$	$Fe^{3+} \downarrow 5\mu_B$	$Ni^{2+} \uparrow 2\mu_B$ $Fe^{3+} \uparrow 5\mu_B$	$2\mu_B$
$MnFe_2O_4$	$Mn^{2+} \downarrow 0.8 \times 5\mu_B$ $Fe^{3+} \downarrow 0.2 \times 5\mu_B$	$Mn^{2+} \uparrow 0.2 \times 5\mu_B$ $Fe^{3+} \uparrow 0.8 \times 5\mu_B$ $Fe^{3+} \uparrow 5\mu_B$	$5\mu_B$
$ZnFe_2O_4$	$Zn^{2+} \downarrow 0\mu_B$	$Fe^{3+} \uparrow 5\mu_B$ $Fe^{3+} \downarrow 5\mu_B$	$0\mu_B$
$Zn_xMn_{(1-x)}Fe_2O_4$	$Zn^{2+} \downarrow 0\mu_B$ $Mn^{2+} \downarrow (1-x) \times 5\mu_B$	$Fe^{3+} \uparrow 5\mu_B$ $Fe^{3+} \uparrow 5\mu_B$	$(1+x) \times 5\mu_B$
$Zn_xNi_{(1-x)}Fe_2O_4$	$Zn^{2+} \downarrow 0\mu_B$ $Fe^{3+} \downarrow (1-x) \times 5\mu_B$	$Ni^{2+} \uparrow (1-x) \times 2\mu_B$ $Fe^{3+} \uparrow 5\mu_B$ $Fe^{3+} \uparrow x \times 5\mu_B$	$(1+4x) \times 2\mu_B$

Table 16 – Cation occupancy and magnetic moments in different types of spinel ferrites. 1) Inverse ferrite $NiFe_2O_4$ (Fe^{3+} cations in the tetrahedral A sites); 2) Mostly normal ferrite $MnFe_2O_4$; 3) Normal ferrite $ZnFe_2O_4$ (no net magnetic moment); 3) Mixed ferrite $Zn_xMn_{(1-x)}Fe_2O_4$. The addition of the non-magnetic Zn^{2+} ion increases the magnetic moment per formula unit. 4) The same occurs with the mixed ferrite $Zn_xNi_{(1-x)}Fe_2O_4$.

	$n_{B,th}$	$n_{B,exp}$	J_s(T)	T_c (°C)	δ (10^3 kg/m^3)	ρ (Ω·m)	K_1(10^3	J/m^3)
	λ_s (10^{-6})							
$FeFe_2O_4$	4	4.1	0.603	585	5.24	10^{-5}	-12	
	40							
$NiFe_2O_4$	2	2.3	0.340	585	5.38	10^2	-7	-
26								
$CoFe_2O_4$	3	3.7	0.534	520	5.29	10^5	200	-
110								
$MgFe_2O_4$	1	1.0	0.151	440	4.52	10^5	-4	-
6								
$MnFe_2O_4$	5	4.6	0.503	330	5.00	10^2	-4	-
5								

Table 17 - Properties of some basic spinel ferrites. $FeFe_2O_4$, $NiFe_2O_4$ and $CoFe_2O_4$ are inverse spinel ferrites, $MgFe_2O_4$ is mostly inverse (90% of A sites occupied by Fe^{3+}, 10% by Mg^{2+}), $MnFe_2O_4$ is mostly normal (80% of A sites occupied by Mn^{2+}, 20% by Fe^{3+}). $n_{B,th}$ and $n_{B,exp}$ are the calculated and experimental magnetic moments at 0 K per formula unit (Bohr magnetons). $J_s \equiv$ saturation polarization at room temperature; $T_c \equiv$ Curie temperature; $\delta \equiv$ density; $\rho \equiv$ electrical resistivity; $K_1 \equiv$ anisotropy constant; $\lambda_s \equiv$ saturation magnetostriction.

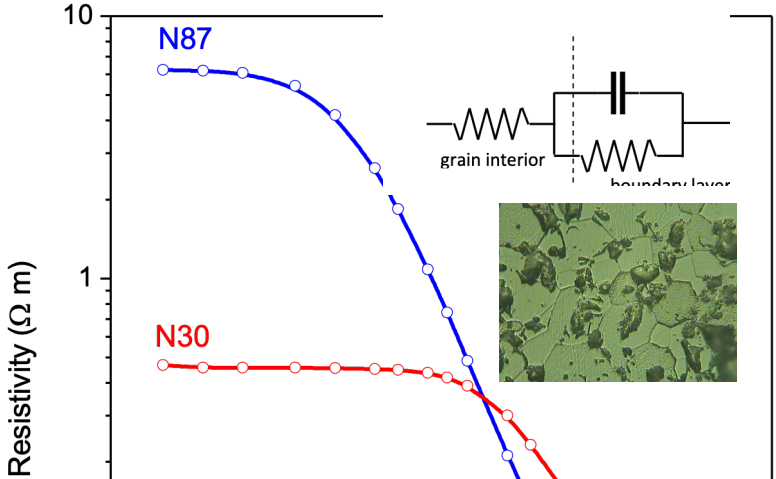

Fig. 46 – Resistivity versus frequency in different types of commercial Mn-Zn sintered ferrites (four-point measuring method). The observed behaviour is consistent with the equivalent R-RC circuit describing the electrical behaviour of a grain and its surface layer [139]. The inset is a micrographic view of a typical grain structure of a Mn-Zn ferrite.

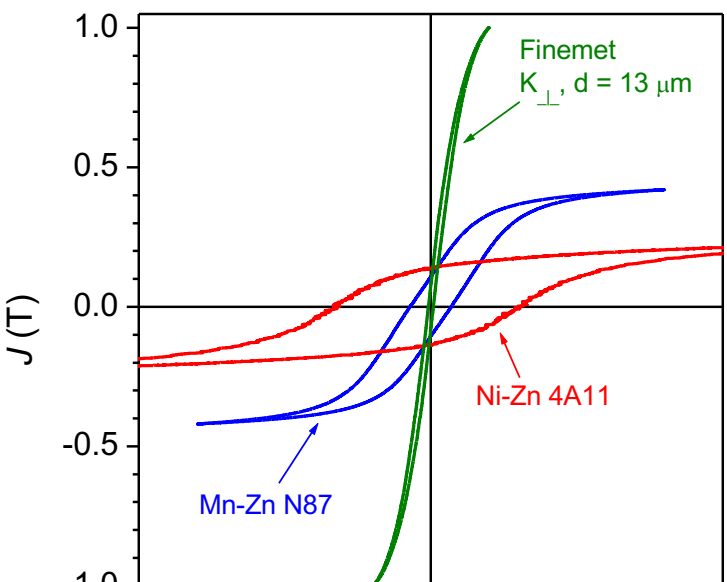

Fig. 47 - Major quasi-static DC hysteresis loops in representative Mn_Zn and Ni-Zn ferrites and in a transverse-anisotropy nanocrystalline ribbon.

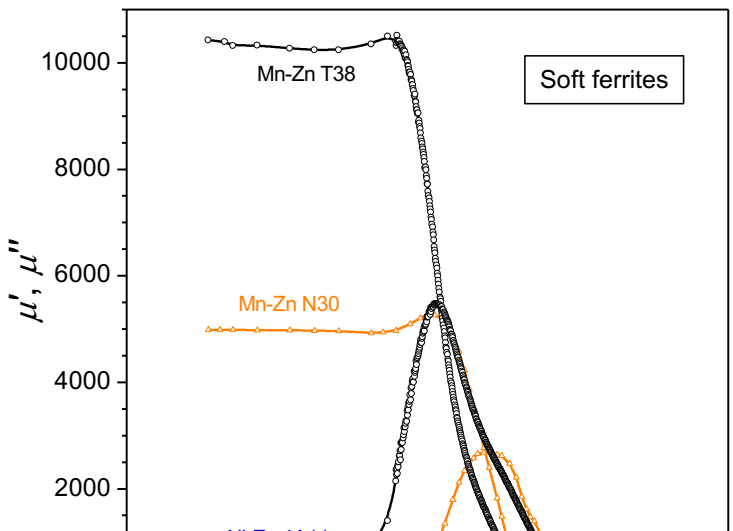

Fig. 48 – Real (μ') and imaginary (μ'') initial permeability components versus frequency in Mn-Zn and Ni-Zn ferrites.

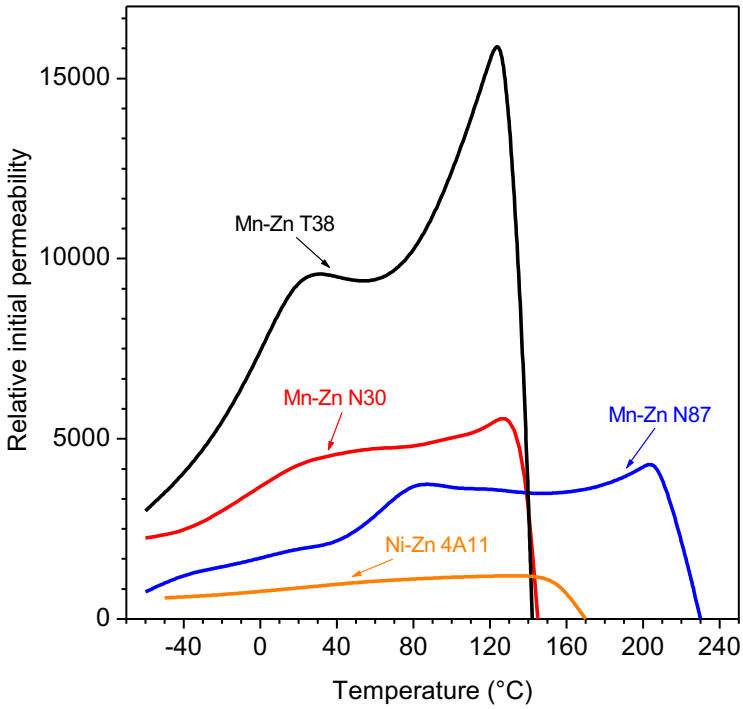

Fig. 49 – Initial permeability versus temperature in commercial Mn-Zn and Ni-Zn sintered soft ferrites.